저작자표시-비영리-변경금지 2.0 대한민국

이용자는 아래의 조건을 따르는 경우에 한하여 자유롭게

- 이 저작물을 복제, 배포, 전송, 전시, 공연 및 방송할 수 있습니다.

다음과 같은 조건을 따라야 합니다:

저작자표시. 귀하는 원저작자를 표시하여야 합니다.

비영리. 귀하는 이 저작물을 영리 목적으로 이용할 수 없습니다.

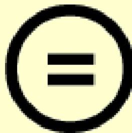
변경금지. 귀하는 이 저작물을 개작, 변형 또는 가공할 수 없습니다.

- 귀하는, 이 저작물의 재이용이나 배포의 경우, 이 저작물에 적용된 이용허락조건을 명확하게 나타내어야 합니다.
- 저작권자로부터 별도의 허가를 받으면 이러한 조건들은 적용되지 않습니다.

저작권법에 따른 이용자의 권리는 위의 내용에 의하여 영향을 받지 않습니다.

이것은 이용허락규약(Legal Code)을 이해하기 쉽게 요약한 것입니다.

Disclaimer

dCollection

이학박사학위논문

산화물/질화물 복합구조를 이용한 유연한 전자 및 광전소자 응용

Hybrid dimensional nanostructures composed of nitride and oxide materials for flexible electronics/optoelectronic

2020년 8월

서울대학교 대학원

물리천문학부 물리학 전공

이 근 동

Doctoral thesis

Hybrid dimensional nanostructures composed of nitride and oxide materials for flexible electronics/optoelectronic

August 2020

Keundong Lee
Department of Physics and Astronomy,
Seoul National University

Hybrid dimensional nanostructures composed of nitride and oxide materials for flexible electronics/optoelectronic

산화물/질화물 복합구조를 이용한 유연한 전자 및 광전소자 응용

지도교수 이 규 철

이 논문을 이학박사학위논문으로 제출함

2020년 07월

서울대학교 대학원

물리천문학부

이 근 동

이근동의 박사학위논문을 인준함

2020년 07월

위 원 장 박 혜 윤 (인)

부 위 원 장 이 규 철 (인)

위 원 전 헌 수 (인)

위 원 홍 성 철 (인)

위 원 홍 영 준 (인)

Abstract

The hybrid dimensional nanostructrures composed of high-quality inorganic nanostructures grown directly on two-dimensional (2D) materials such as graphene offers a novel material system for flexible electronics and optoelectronics. Indeed, the hybrid dimensional nanostructures have been fabricated to flexible electronics/optoelectronics and attracted many attentions with their excellent performances. Despite of the demonstration of flexible devices using the hybrid dimensional nanostructures, there remains a lot of devices that need to be further investigated in order to realize future electronics/optoelectronics such as wearable devices. This thesis presents the hybrid material system composed of oxide/nitrid heterostructures grown on graphene films and their applications on flexible non-volatile memory and flexible multi-color LEDs.

Key-words: graphene; nitride; oxide; flexible electronics; flexible optoelectronics

Student number: 2014-30113

Table of Contents

Abstract

Chapter 1. General Introduction..1

1.1. Motivation: Potentials of hybrid dimensional nanomaterials for flexible electronic/optoelectronic device applications………………1

1.2. Thesis objective and approach……………………………………………3

1.3. Thesis outline………………………………………………………………4

Chapter 2. Literature survey..6

2.1. Oxide-based flexible electronics…………………………………………..6

2.1.1. Current status of oxide-based electronics……………………..8

2.1.2. Next generation oxide-based electronics: ReRAM…………12

2.1.3. Flexible ReRAM………………………………………………..17

2.1.3.1. ReRAM on plastic substrates……………………….17
2.1.3.2. Transfer of ReRAM layers on flexible substrates...20
2.2. Nitride-based flexible optoelectronics…………………………………..23
2.2.1. Current status of nitride-based optoelectronics……………..23
2.2.2. Next generation nitride-based optoelectronics
: flexible & high-resolution LED………………………………..29
2.3. Hybrid dimensional material systems for flexible electronics and
Optoelectronics……………………………………………………………34
2.3.1. Growth of oxide & nitride nano-/micro-structures on
graphene layers……………………………………………….35
2.3.2. Functional devices using hybrid dimensional material
Systems…………………………………………………………..45
2.3.2.1. Electronics……………………………………………..47
2.3.2.2. Optoelectronics……………………………………..50
Chapter 3. Experimental Techniques……………………………...53
3.1. Growth techniques………………………………………………………..53

3.1.1. Metalorganic vapor-phase epitaxy system………………….53

3.1.1.1. Gas delivery system……………………………...53

3.1.1.2. Reactor and temperature controller……………….55

3.1.1.3. Exhaust disposal system and low pressure pumping

System………………………………………………56

3.2. Structural characterization……………………………………………….57

3.2.1. Morphology inspection……………………………………...57

3.2.2. Crystallographic and microstructural investigations………..57

3.2.2.1. Transmission electron microscopy………………..57

3.3. Optical characterization…………………………………………………..58

3.3.1. Photoluminescence & electroluminescence spectroscopy..58

3.4. Electrical characterization………………………………………………..59

3.4.1. Current-Voltage measurement………………………………59

Chapter 4. Flexible ReRAM based on hybrid dimensional material systems...60

4.1.

Introduction……………………………………………………………...60

4.2. Growth of oxide/nitride hybrid structures on graphene layers…………61

4.2.1. ZnO nanowall growth CVD-graphene films…………………62

4.2.2. Growth of GaN microdisk arrays……………………………..62

4.2.3. Growth of resistive switching layers…………………………..65

4.4. Fabrication of flexible ReRAM……………………………………………65

4.5. Resistive switching characteristics………………………………………69

4.6. Discussion for the mechanism of resistive switchings using oxide/nitride hybrid structures……………………………………………78

4.6.1. Fabrication of ReRAM/LED hybrid device…………………..80

4.6.2. Real-time imaging of resistive switching dynamics…………85

4.7. Summary……………………………………………………………………..99

Chapter 5. Monolithic integration of morphology controlled GaN microstructures on graphene films for flexible & multi-color

LEDs……………………………………………………………101

5.1. Introduction………………………………………………………….……………101

5.2. Morphology control of GaN microstructures on graphene films…….103

5.2.1. Growth parameter: spacing & time…………………………103

5.2.2. Growth behavior analysis……………………………………109

5.3. Fabrication of LEDs on graphene films…………………………..…115

5.4. EL and electrical characteristics………………………………….…118

5.5. High temperature operations of flexible LEDs………………………...125

5.6. Summary……………………………………………………………………134

Chapter 6. Conclusion and Outlook……………………………136

6.1. Conclusion…………………………………………………………………..136

6.2. Future works and outlook…………………………………………………141

References..143

Abstract

(Korean)……………………………………………………...151

List of Figures

Figure 2.1. Conceptual figure for the symmetries and degrees of freedom of correlated electrons which can be engineered at oxide interfaces...7

Figure 2.2. Schematic showing (a) different physical properties and applications of oxide materials. (b) Evolution of thin film transistor technology and its potential future applications. 10

Figure 2.3. Vertical surround-gate ZnO nanowire FETs. (a) Cross-sectional top-view SEM image of a ZnO nanowire conformally coated with a gate oxide and metal electrode (top), and schematic illustration of a vertical surround-gate FETs (bottom). (b) Ids–|Vg–Vth| characteristic curves for both n-type and p-type FETs. The inset shows a cross-sectional SEM image of a FET with a channel length of ~200 nm.................................11

Figure 2.4. 2013 ITRS ERD critical review of emerging memories based on eight criteria, where "3" and "1" represent the best and the worst assessment scores, respectively. ...13

Figure 2.5. *I–V* curves for (a) unipolar switching in a Pt/NiO/Pt cell and (b) bipolar switching in a Ti/La2CuO4/La1.65Sr0.35CuO4 cell. Proposed models for resistive switching can be classified according to either (c) a filamentary conducting path, or (d) an interface-type conducting path...16

Figure 2.6. I–V curves of two-layer cells (a) not flexed and (b) after 100-times bending. The inset of (a) shows the optical image of two measured cells.......................................19

Figure 2.7. a) Schematic illustrations of the process for fabricating flexible crossbar-structured memory on a plastic substrate via the ILLO method. b) simulation of temperature distribution c) A cross-sectional SEM image of the overall structures. d) A

magnified optical image of the front side (upper region) and back (lower region) of the memory array transferred onto a flexible substrate. The e) A photograph of the flexible RRAM device on a plastic substrate...22

Figure 2.8. SEM pictures (45° tilted) of various micro-crystals simultaneously grown by pulsed SAE. Estimated polar, semi-polar, and non-polar surface contributions are reported for each pattern size. Scale bars represent 5 μm. 33

Figure 2.9. FE-SEM image of ZnO nanostructures grown on the graphene layerstransferred onto the SiO2 / Si substrates. 36

Figure 2.10. (a) Schematic illustration of ZnO nanostructures grown on graphene coated TEM grid for TEM analysis. (b) HR-TEM image of ZnO grown on graphene. The inset shows diffraction patterns of ZnO and graphene. 38

Figure 2.11 Controlled growth of ZnO nanostructures on graphene layers. (a) Schematic illustration of growing position-and morphology-controlled ZnO nanostructures on mechanically exfoliated graphene layers, (b) SEM images of resulting ZnO nanostructures. (c) Strategy of growth of ZnO nanotube on CVD graphene layers. (d) Photographs of ZnO nanotube grown graphene/Si wafer. (inset) Magnified SEM images of the ZnO nanotubes. 40

Figure 2.12 Growth of GaN thin-film on graphene layers using ZnO nanowall as an intermediate layer. (a) Schematic illustration of heteroepitaxial growth of GaN thin-film on graphene layers using ZnO nanowall networks. (b) Microscope image of the mechanically exfoliated graphene layers. (c) SEM image of dense ZnO nanowall networks. (d) SEM image of the grown GaN thin film showing flat surface

morphology...43

Figure 2.13 Microstructure of the GaN thin film grown on graphene layers. (a) Low-magnification cross-sectional image of the GaN/ZnO/graphene heterostructure. (b, c) Selective area diffraction patterns from the circle-marked area in (a). 44

Figure 2.14. Temperature dependent PL spectra of ZnO nanostructures grown on graphene layer...46

Figure 2.15. Fabrication of a nanotube crossbar array by (a) designing gold (Au) electrode lines as Schottky contacts on the top surface of the ZnO nanotubes and (b) deposition of chromium (Cr)/Au electrodes, followed by a reactive ion etching process, to create graphene layers/Cr/Au electrode lines as ohmic contacts on the bottom surface. (c) Overall structure of the nanotube device array with Au and graphene layers/Cr/Au electrode lines contacting individual nanotubes. The top and bottom electrodes are cross-aligned. (d) Photograph of the ultrathin and flexible nanotube device array. (e) Tilted SEM images clearly demonstrating precise alignment of the (f) top and (g) bottom electrodes with the ZnO nanotube device array. (h) Cross-sectional SEM image of the nanotube device array. 48

Figure 2.16. Bending test of the GaN micro-LED array. a) Optical image of GaN micro-LEDs wrapped around a 1 mm diameter paper clip. b) Low-magnification and c) high-magnification FE-SEM images of GaN micro-LEDs under bending radii of 0.6–0.8 mm. d) Room temperature EL spectra and e) *I–V* curves of the micro-LEDs under various bending radii. The inset in (d) shows a light emission image of the micro-LEDs at a bending radius of 6 mm. 52

Figure 3.1. Schematics of gas delivery systems..55

Figure 4.1. SEM image of GaN microdisk arrays..64

Figure 4.2. Schematics of the oxide/nitride/graphene hybrid material system growth and its device fabrication process. 67

Figure 4.3. Releasing the device arrays using the thermal release tape. 68

Figure 4.4. *I–V* characteristic curves of ReRAM disk at variously strain states including flat, bent, and rolled states. Inset shows a photograph of the device showing semi-transparency. 71

Figure 4.5. Resistive switching characteristics of ReRAM disk on plastic substrate. (a) cumulative probability, (b) endurance, (c) retention, and (d) reliability about number of bending cycles. 75

Figure 4.6. Comparison of resistive switching characteristics of ReRAM disk at 300K and 450K. (a) cumulative probability, (b) endurance..77

Figure 4.7. Transport and light emitting characteristics of a ReRAM/LED hybrid device. (a) Schematic device structures, (b) resistive switching behaviors, and (c) light emission images of a ReRAM/LED hybrid device in LRS and HRS. For comparison, resistive switching behaviors of a conventional ReRAM are also displayed in (b). 84

Figure 4.8. Electrode dependent LED performance. Current-voltage curves of LED devices with (a) Au/Ni and (b) Pt top electrode. The upper insets show schematic diagrams of LED devices and the lower inset of (a) reveals the light emission image obtained from the Au/Ni/LED device...87

Figure 4.9. Resistive switching and real-time light emission during semi-forming and forming processes. (a) Resistive switching behaviors and (b) light emission images of a

ReRAM/LED hybrid device during semi-forming and forming processes. Black and red open squares in (a) indicate semi-forming and forming processes, respectively. Light emission images in (b) are obtained when I-V curves in (a) reach the points marked with arrows and numbers during resistive switching..90

Figure 4.10. Repetitive resistive switching and real-time light emission. (a, c, e) I-V curves and (b, d, e) light emission images of a ReRAM/LED hybrid device during (a and b) stable reset and stable set (SrSs), (c and d) stable reset and unstable set (SrUs), and (e and f) unstable reset and stable set (UrSs) processes. Light emission images are obtained when I-V curves reach the points marked with arrows and numbers during resistive switching.
....94

Figure 4.11. More unstable reset switching and real-time light emission. (a and c) I-V curves and (b and d) light emission images of a ReRAM/LED hybrid device during (a and b) more unstable reset and (c and d) subsequent set processes...............................96

Figure 4.12. 50 times resistive switchings and real-time light emission. (a) I_{set} versus V_{set} relationship and (b-e) light emission images obtained at several set switchings during 50 times resistive switchings of other ReRAM/LED hybrid device...98

Figure 5.1. SEM images of ZnO nanostructures with different spacings. (a) 2, (b) 4, (c) 6, and (d) 8 μm. 10
5

Figure 5.2. Morphology controlled growth of GaN/ZnO heterostructures. SEM images of the GaN/ZnO heterostructures with different spacings and growth times show gradual change of their morphology from microrod to micropyramid. 108

Figure 5.3. GaN/ZnO heterostructures grown at different temperatures and schematic illustration of their growth mechanism……………………………………………………………………111

Figure 5.4. Strategy for the monolithic integration of GaN microrod and micropyramid on CVD graphene films……………………………………………………………………………………113

Figure 5.5. SEM image of GaN microstructures grown on ZnO nanostructures with spacing of 12 μm……………………………………………………………………………………………114

Figure 5.6. Schematic illustration of monolithic integrated flexible LED. (a) device fabrication and (b) its demonstration at 9.0 V. …………………………………………………………117

Figure 5.7. EL spectra of (a) microrod-based and (b) micropyramid-based LEDs as a function of current levels from 0.11 to 0.50 mA……………………………………………………121

Figure 5.8. TEM images of monolithically integrated LEDs on CVD graphene films. (a) microrod-based LED. (b) micropyramid-based LED…………………………………………………122

Figure 5.9. Flexibility demonstrations. (a) Light emission photographs at bending radii of ∞, 7, 5, 3.5 mm. I–V characteristic curves as a function of the bending cycle for (b) microrod-based and (c) micropyramid-based LEDs. (d) Normalized EL intensity of the microrod-based (top) and micropyramid-based LEDs during 1000 times of bending.124

Figure 5.10. Temperature dependent $I-V$ characteristic curves of GaN microdisk LEDs. The temperature increased from 293 to 373 K by 10 K……………………………………………128

Figure 5.11. Temperature dependent EL spectra of GaN microdisk LEDs and GaN thin film LEDs..130

Figure 5.12. Analysis of the light-emitting characteristics as a function of temperature. (a) Plot of light intensity as a function of temperature. (b) Plot of peak energy of light emission as a function of temperature. 133

Table 4.1. Distributions and SDs of V_{set} and V_{reset} at variously strained state..76

General introduction

1

1.1. Motivation: Potentials of hybrid dimensional nanomaterials for flexible electronic/optoelectronic device applications

Large-scale and flexible inorganic optoelectronic devices have recently attracted much attention for use in such as wearable displays, sensors and biomedical devices.[1] For the bendable and wearable devices, organic films have widely been employed due to their excellent scalability and flexibility.[2, 3] Compared with organic material which has widely been used for flexible devices, inorganic semiconductor in the hybrid material offers better electrical and optical characteristics including higher carrier mobility and electron-hole pair recombination rate as well as higher stability and reliability at high temperature and harsh condition.[4] However, achieving flexible devices using inorganic films is still very challenging because of the rigidity and brittleness inherent to inorganic films and single-crystalline substrates.[5] For their large-area or flexible-device applications, the device must be fabricated on glass, plastic, or metal substrates.

However, high quality epitaxial films can be grown only on a lattice-matched single-crystal substrate at a high growth temperature so it is very challenging to grow epitaxial films on those substrates. For this reason, the films have been grown epitaxially on a sapphire substrate and lift-off using the laser lift-off process to transfer device layers onto the flexible substrate.[6] However, difficulties in separating the films from a single-crystal substrate and limitations in large scalability arising from size of the single-crystalline substrate limited the use of such techniques.

To resolve this problem, growths of inorganic nanostructures on chemical-vapor deposited (CVD)-graphene films have recently been proposed.[7, 8] CVD graphene films have hexagonal structure offering epitaxial relationship with semiconductors with wurtzite, zinc blende or diamond structures. In addition, their high chemical/thermal stability enables them to be used as a good substrate for the growth of high-quality semiconductors. Moreover, their atomic-scale layered sheets bonded by van der Waals force offer transferability and flexibility. Those novel material characteristics make CVD graphene films ideal for the

substrate of the inorganic nanostructure growth for fabrications of flexible electronics/optoelectronics.

1.2. Thesis objective and approach

Hybrid-dimensional nanostructures have been investigated and their applications on flexible devices including field effect transistor (FET) and blue light emitting diodes (LEDs) have been demonstrated.[9-11] Their excellent device performances after many times of bendings are promising to demonstrate wearable devices which require stable device performances under physically harsh conditions. Although previous works on hybrid materials have focused on flexible LEDs and FET, these graphene-based hybrid materials can provide further functionality beyond previously demonstrated devices. For example, electronics need to not only process the information, but also be capable for data storages to save the processed data. To communicate the processed data with user efficiently, high-resolution optoelectronics are required to display the information accurately.

The main objective of the dissertation is to develop more functional devices to meet demands for flexible devices based on hybrid dimensional nanomaterial systems. The approach of this dissertation is to develop new material system which gives novel functionality to the hybrid dimensional nanomaterial systems. In more detail, Chapter 4 presents oxide/nitride hybrid material system prepared on CVD-graphene films to fabricate flexible resistive random access memory (ReRAM) which is well-known as one of the next generation non-volatile memory devices. Furthermore, Chapter 5 will discuss about morphology controlled growth technique to monolithically integrate different oxide/nitride microstructures on CVD-graphene films to demonstrate flexible and multi-color LEDs.

1.3. Thesis Outlines

This dissertation is composed of five chapters. Chapter 2 reviews current research activities and history on oxide based electronics, nitride based optoelectronics and their flexible device applications. This chapter will then

review the flexible devices based on hybrid dimensional material systems to introduce current status of flexible device applications composed of inorganic nanostructures grown on graphene films. Chapter 3 describes experimental procedures including growth, characterization process. In Chapter 4, material growth of oxide thin films as a resistive switching layer on nitride microstructures prepared on CVD-graphene films and their ReRAM application are described. Furthermore, the dynamics of resistive switchings are carefully studied by real-time imaging of the light emission from the LED films corresponding to locations of the conducting filament emerged in the ReRAM device which is considered as an origin of the resistive switching. Chapter 5 presents morphology controlled growth of GaN microstructures on ZnO nanotubes prepared on CVD-graphene films and their application on flexible multi-color LEDs by monolithic integration of different LEDs on CVD-graphene films.

Literature survey

2

2.1. Oxide-based flexible electronics

Multi-functionality of oxide materials is crucial to overcome the fundamental limitation of the current CMOS-based information technology.[12] As shown in **Figure 2.1**, oxides can respond to electrical, magnetic, thermal and mechanical stimulations due to their novel material characteristics.[13] In many materials, information can be stored into by gating, tunneling or emergence of various domains including ferro/antiferromagnetic, ferroelectric, and multi-ferroic. These properties enable the demonstration of many transistors and non-volatile memories. Using these novel characteristics, ultra-fast, non-volatile memories has been developed as next generation memory devices and commercialized.[14] Moreover, recent rapid development in nanofabrication technique and material engineering have motivated to investigate fabrications of flexible electronics for their wearable device applications.[15] In this chapter, current status of oxide-based

electronics and their next generation device will be described and their applications on flexible electronics will be reviewed.

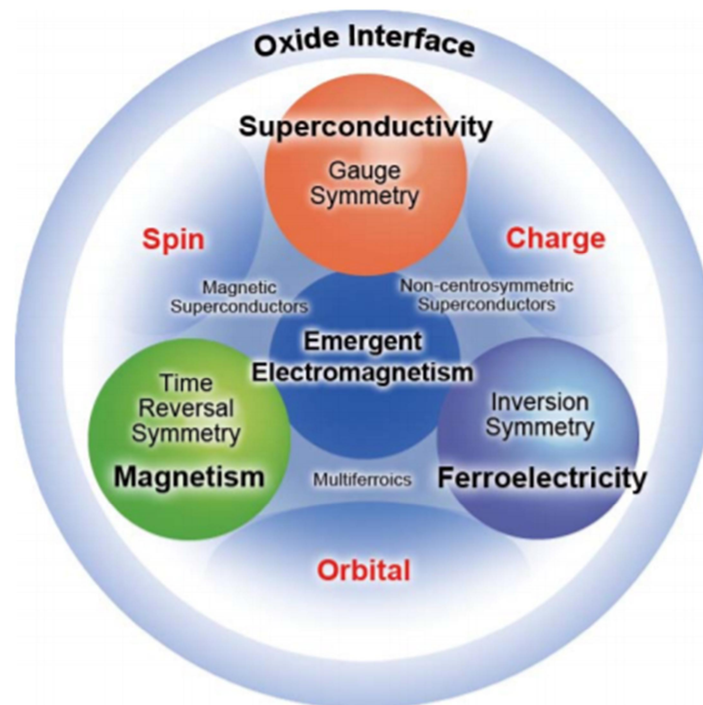

Figure 2.1. Conceptual figure for the symmetries and degrees of freedom of correlated electrons which can be engineered at oxide interfaces.[13]

2.1.1. Current status of oxide-based electronics

MOSFETs (Metal-Oxide-Semiconductor Field-Effect Transistors) have for a long time been the basic component of modern electronics. For the purpose of a highly scalable integration, the size of a MOSFET has been decreasing with the Moore's Law, but nowadays, owing to the restrictions from their intrinsic material and device properties, the further down scaling of MOSFETs becomes very challenging resulting in devising the complex fabrication processes and expensive engineering solutions.[16]

To overcome those issues, there are alternative approaches proposing new device concepts based on new material candidates based on metal oxides (TMOs) or new device geometries as introduced in **Figure 2.2.**[17-20] For instance, the Mott transition in vanadium dioxide caused by strong electron-electron correlation is considered as one of the most promising phenomena for oxide electronics and applied on FET known as a Mott-transition field-effect transistor (MTFET).[21, 22] As an another example, rather than shrinking the device's structure further resulting in electrons to leak through the narrow part of the channel, researchers

have developed FETs with three-dimensional structures.[23-25] In particular, nanowire based vertical-channel field-effect transistors (VFETs) were proposed that enable to surround gate transistors, in which the gate is wrapped around a nanowire channel to provide the best possible electrostatic gate control. Ng *et al.* demonstrated vertical surround-gate FETs using vertically aligned ZnO nanowire arrays grown on SiC substrates[26]. For the device fabrication, as shown in **Figure. 2.3**, a conformal coating of the SiO_2 gate oxide and metal (Cr) gate electrode over the entire surface of the nanowire was performed using CVD and ion beam deposition techniques, respectively. The geometry of the vertical device was reduced because the drain, source, and channel are stacked on top of each other vertically, potentially enabling the high packing density. These types of three dimensional FETs have been demonstrated by ZnO nanorods and they are further functionalized to pressure sensors, actuators, and generators gating by piezoelectric stimulations.

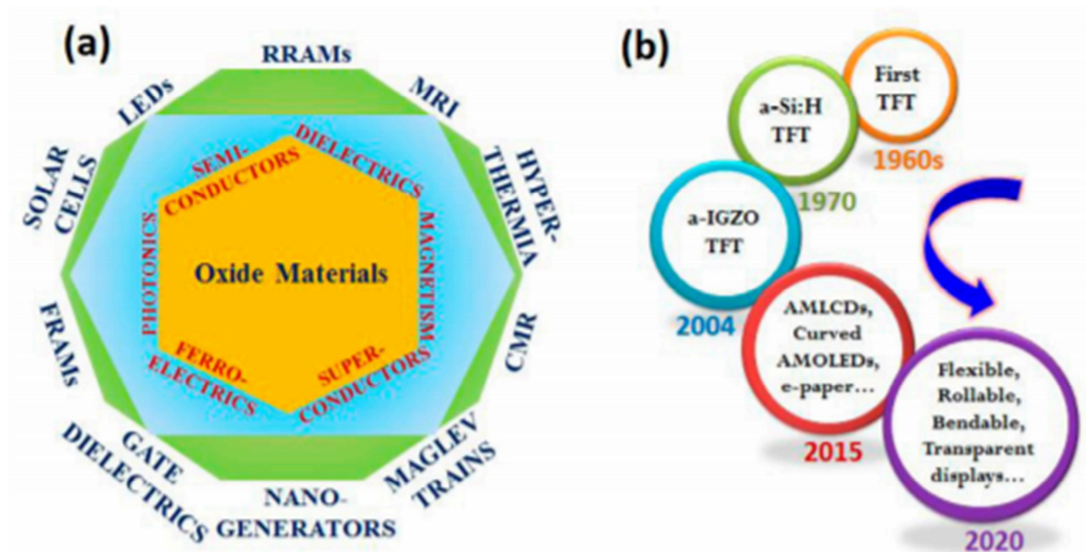

Figure 2.2. Schematic showing (a) different physical properties and applications of oxide materials. (b) Evolution of thin film transistor technology and its potential future applications.[20]

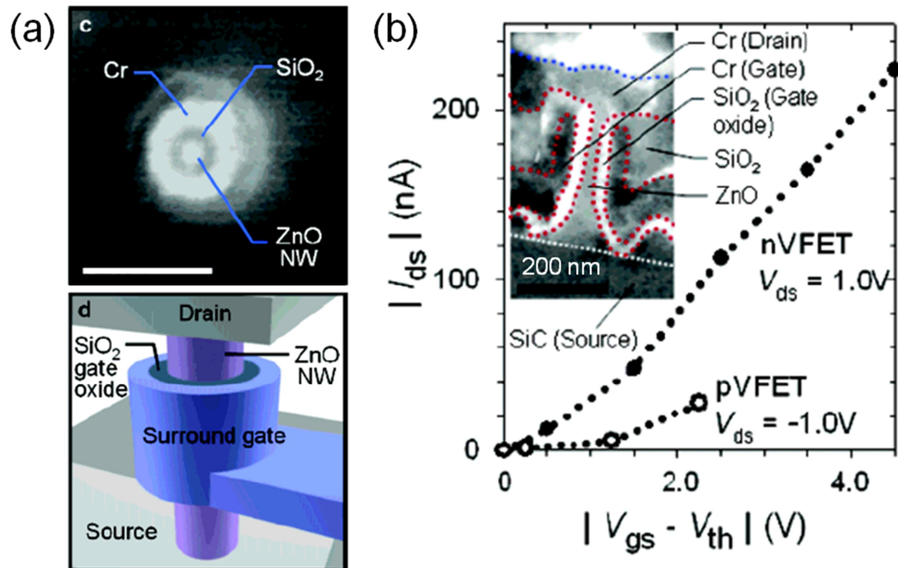

Figure 2.3. Vertical surround-gate ZnO nanowire FETs[26]. (a) Cross-sectional top-view SEM image of a ZnO nanowire conformally coated with a gate oxide and metal electrode (top), and schematic illustration of a vertical surround-gate FETs (bottom). (b) Ids–|Vg–Vth| characteristic curves for both n-type and p-type FETs. The inset shows a cross-sectional SEM image of a FET with a channel length of ~200 nm.

2.1.2. Next generation oxide-based electronics: ReRAM

Nowadays, regarding nonvolatile memories, flash memory has been successfully scaled down to achieve large memory capacity. However, it is expected that further dramatic scale down would be very challenging because of technical and physical limits in the near future. In order to overcome this problem, functionalization by introducing new materials and/or three dimensional device geometry, has been proposed as a new alternative approaches to meet a requirement for down scaling as sown in **Figure 2.4**.[27] They are called as next generation non-volatile memories including ferroelectric random access memory (FeRAM),[28, 29] in which the polarization of a ferroelectric material manages the resistance of the device, magnetoresistive RAM (MRAM),[30, 31] which uses magnetic tunnel junctions, and phase-change RAM (PCRAM),[32, 33] operating the resistive switching by applying voltages to change their crystallinity between crystalline and amorphous states of a chalcogenide compound, have attracted a great deal of attention.

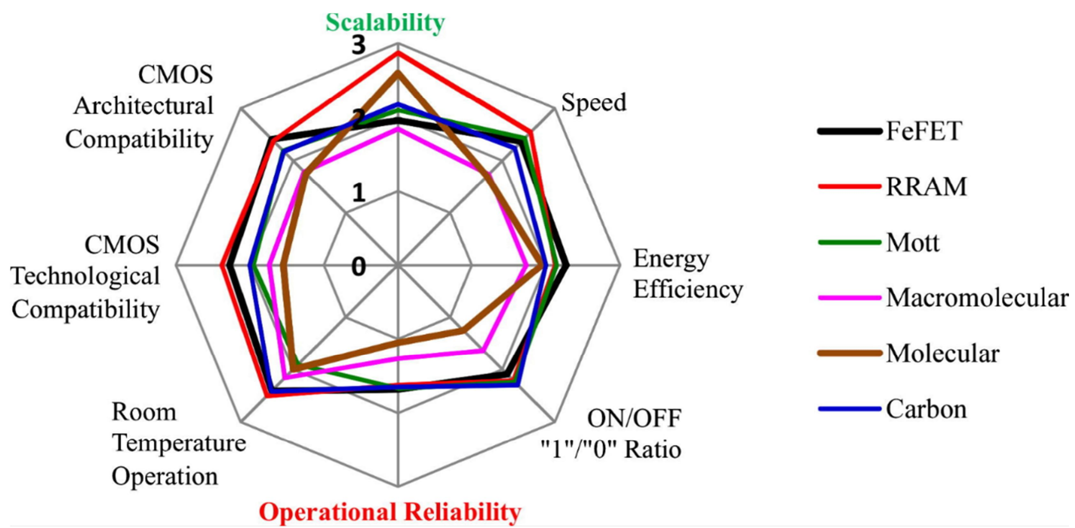

Figure 2.4. 2013 ITRS ERD critical review of emerging memories based on eight criteria, where "3" and "1" represent the best and the worst assessment scores, respectively.[27]

Meanwhile, using a resistive switching phenomenon found in TMOs, the oxide-based new candidate has emerged: resistance random access memory (ReRAM).[34, 35] As shown in **Figure 2.5**, the resistive switching occurs either in the manner of the applying bias voltages to unipolar or bipolar directions. In more detail, in unipolar resistive switching, the resistive switching depends on the amplitude of the applied voltage but not on the polarity (Figure 2.5 (a)). An as-prepared device is in a highly resistive state and is driven into a low-resistance state (LRS) by applying a relatively high bias voltage which is called the 'forming process'. After the forming process, the device in a LRS is switched to a high-resistance state (HRS) by applying bias voltage ('reset process'). Switching from a HRS to a LRS ('set process') is achieved by applying a threshold voltage that is larger than the reset voltage. In the set process, the current is limited by the current compliance of the control system to prevent abrupt current flowing resulting in device burning. Meanwhile, bipolar resistive switching operates similarly but depends on the polarity of applied bias voltage (Figure 2.5 (b)).

The origin of the conducting path resulting in the resistive switching can

be also classified by the unipolar/bipolar switching types. In the unipolar switching, filament-type resistive switching has been reported that the conductive filaments form in the bulk of the thin film (Figure 2.5 (c)). In more detail, during the forming process, filamentary metallic TMOs form as a soft breakdown in the dielectric material. These filaments are ruptured then formed while we applied the bias during reset and set processes, respectively. The rupture and formation of the conductive filaments are originated by joule heating, thermal redox and/or anodization near the interface between the metal electrode corresponding to soft-disconnection and reconnection of conductive filaments. In contrast, in the bipolar-type, migration of oxygen ions at the interface is regarded as the associated mechanism (Figure 2.5 (d)).

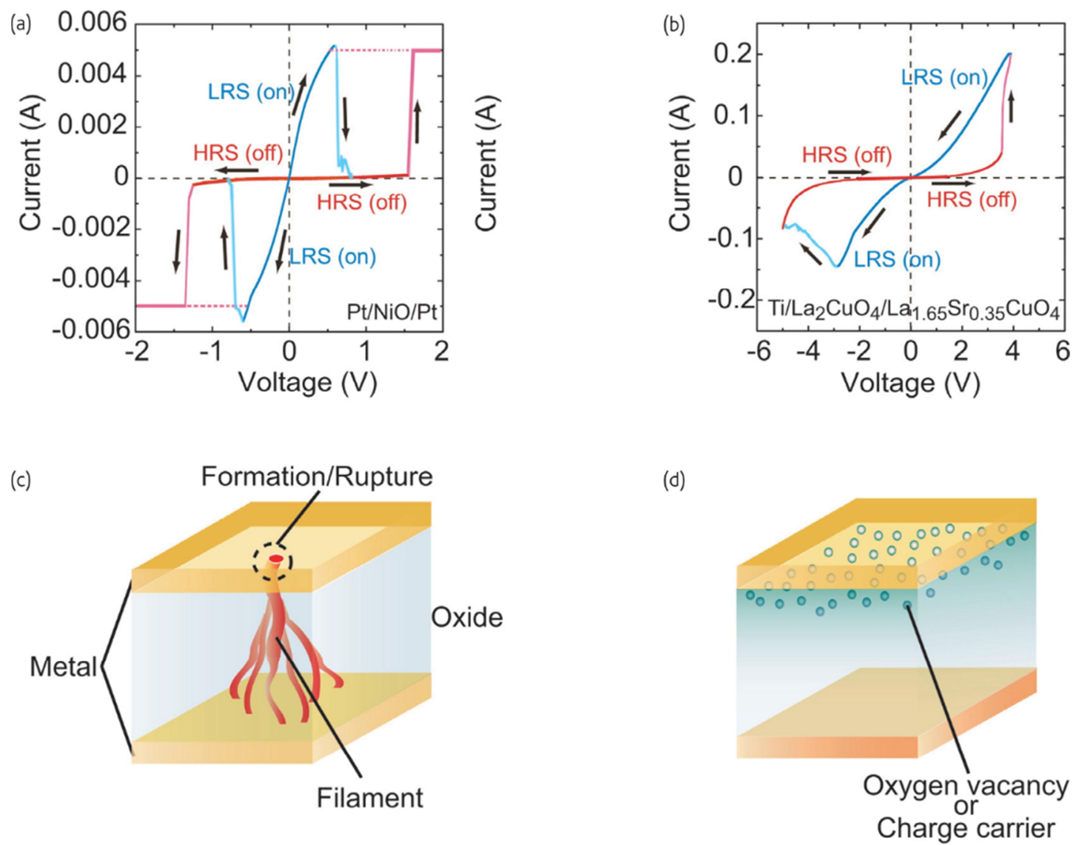

Figure 2.5. *I–V* curves for (a) unipolar switching in a Pt/NiO/Pt cell and (b) bipolar switching in a Ti/La2CuO4/La1.65Sr0.35CuO4 cell. Proposed models for resistive switching can be classified according to either (c) a filamentary conducting path, or (d) an interface-type conducting path.[35]

2.1.3. Flexible ReRAM

ReRAM has various advantages in comparing to other memories including simple and highly scalable two terminal structures, high resistive switching speed and low power consumption.[34-36] Those properties are essential requirements for their wearable electronics applications so fabrications of the ReRAM on flexible substrate have attracted attentions. This part generally reviews fabrications of flexible ReRAM by many brilliant approaches including spin coating, low-temperature deposition, and laser lift-off processes.

2.1.3.1. ReRAM on plastic substrates

Researches about flexible ReRAM have been performed mainly using organic materials due to their excellent flexibility. However, organic materials and devices have critical weaknesses in the long-term reliablity and durability at atmospheric conditions. In contrast, oxide-based ReRAM generally exhibit excellent stability and better durability.

To demonstrate the oxide-based ReRAM on flexible substrate, low temperature oxide thin film deposition techniques were developed. They are

followed by metal film depositions on plastic substrates then subsequent low temperature and/or plasma assisted oxidation processes are performed.[37-39] Using an aluminium oxide as a resistive switching layer, more than 5,000 times of repetitive switching cycles were able to be demonstrated due to its high ductility. Moreoever, ReRAM with a passive matrix array was also fabricated on plastic substrates by low temperature deposition of TiO_2 layers.[39] They further demonstrated double-layer-stacked device composed of $Al/TiO_2/Al/TiO_2/Al$ on the plastic substrate for its high density flexible memory device applications (**Figure 2.6**). They examined its non-volatile memory performances and confirmed its non-volatile memory characteristics.

Meanwhile, solution processes TiO_2 layers also exhibited resistive switching characteristics.[40] They thermally heated spin-coated TiO_2 solutions on the plastic substrate and fabricated ReRAM devices. This ReRAM investrigated by means of a continuous substrate bending test revealed that the ratio of the HRS to LRS remained over 1K until two hundred cycles were reached.

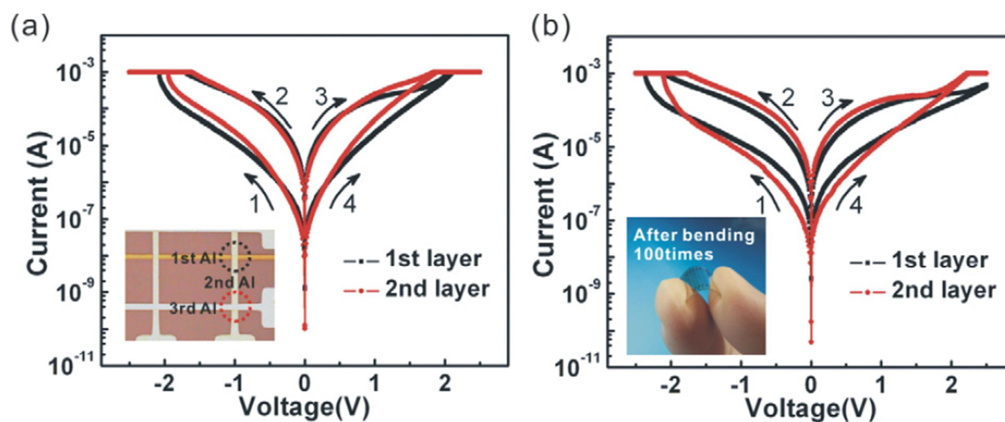

Figure 2.6. I–V curves of two-layer cells (a) not flexed and (b) after 100-times bending. The inset of (a) shows the optical image of two measured cells.[39]

2.1.3.2. Transfer of ReRAM layers onto flexible substrates

Although these flexible ReRAMs have been well-established with the capability of achieving flexible electronics, there are still big challenges including how to resolve insufficient performance arising from inherent material properties due to the low temperature process. To address these limitations, there have been attempted to transfer high-quality grown inorganic materials from transparent inorganic substrates onto flexible substrates using a strong laser, enabling to incorporating the excellent characteristics of the inorganic materials synthesized under sufficiently high temperature. Using this technique, many inorganic materials become transferrable so that many kinds of electronics have been realized on flexible substrates.[15]

As shown in **Figure 2.7**. this method has also been applied for the flexible ReRAM fabrication. Researchers reported a strategy for the fabrication of flexible memory employing a one selector–one resistor (1S–1R) crossbar structure on a plastic substrate via an inorganic based laser lift-off (ILLO) process. The 1S–1R electronics of flexible memory composed of 32 × 32 arrays were fabricated with

an inorganic laser-reactive exfoliation layer on a glass substrate which is CMOS compatible, and then subsequently transferred onto a flexible substrate through the ILLO process. Their 1k memory cells performed excellent addressing tests verifying the absence of crosstalk issues and poor resistive switching characteristics under various conditions, writing symbolized letters on a plastic substrate.

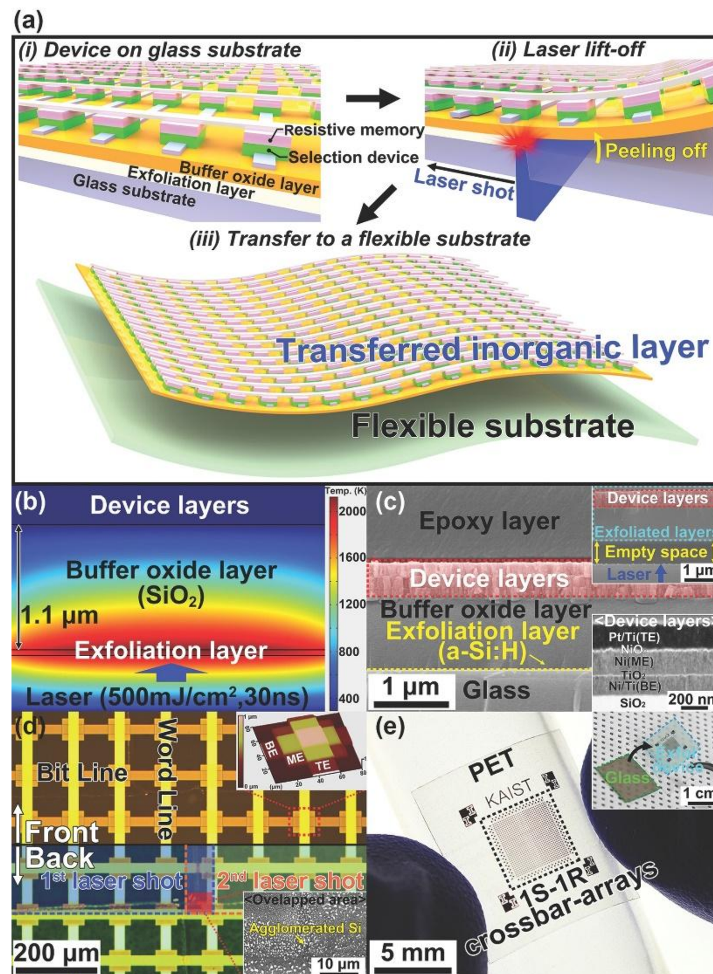

Figure 2.7. a) Schematic illustrations of the process for fabricating flexible crossbar-structured memory on a plastic substrate via the ILLO method. b) simulation of temperature distribution c) A cross-sectional SEM image of the overall structures. d) A magnified optical image of the front side (upper region) and back (lower region) of the memory array transferred onto a flexible substrate. The e) A photograph of the flexible RRAM device on a plastic substrate.[15]

2.2. Nitride-based flexible optoelectronics

Inorganic compound semiconductors, such as GaAs and GaN, provide many advantages for optoelectronic device applications, including high carrier mobility and radiative recombination rates as well as long-term stability and reliability.[41] Especially, the excellent optical and electrical characteristics of GaN enable fabrications of full-color-spectrum nitride LEDs with high efficiency and long-term stability and they are now commercially available. Those performances are essential for wearable display applications to communicate with a user while the device is under flexible states.[42, 43] Indeed. the demonstrations of GaN LEDs on flexible substrates have been investigated tremendously. This part describes general review of nitride-based optoelectronics and their applications on flexible LEDs.

2.2.1. Current status of nitride-based optoelectronics

The alloy of the III-nitrides has direct band gaps with wide ranging from 0.7 eV (InN) to 6.2 eV (AlN) with 3.4eV for GaN.[44] The band gaps of the alloy can be tuned from 0.7 to 6.2eV by suitable alloy combinations in the AlGaInN

system covering the entire UV and visible ranges.[45, 46] Therefore, the III-nitride material systems have attracted tremendous attention for application on variety of optoelectronic devices, in particular, LEDs.

An LED consists of a sandwich of a *p*-type and *n*-type GaN layers. These *p*- and *n*-type GaN are produced by doping with donor and acceptor atoms respectively. When a forward bias electric field is applied across the *p*–*n* junction, electrons from the *n*-type GaN and holes from the *p*-type GaN are driven into the *p*–*n* junction region. When the electrons and holes recombine, this recombination results in the spontaneous light emission corresponding the bandgap energy. In more detail, an electron meets a hole during a recombination state, then the electron falls into a lower energy level releasing its energy as a photon. Therefore, wavelength of the light depends on the band gap energy of the materials of the *p*–*n* junction.

A light emitting diode, usually called an LED, is a semiconductor diode that emits incoherent narrow-spectrum light when electrically biased in the forward direction of the *p-n* junction. Like a normal diode, the LED consists of a

chip of semiconducting material impregnated, or doped, with impurities to create a *p–n* junction. Charge-carriers (electrons and holes) flow into the junction from electrodes with different voltages. In silicon or germanium diodes, the electrons and holes recombine by a non-radiative transition which produces no optical emission, because these are indirect band gap materials. The materials used for the LED have a direct band gap with energies corresponding to near-infrared, visible or near-ultraviolet light.

To demonstrate highly efficient GaN-based LEDs, it is important to grow the films with dislocation densities as low as possible, less than 10^6 cm^{-2}.[47, 48] One of the critical parameters to grow high quality films was finding ideal substrate because the origin of dislocation comes from lattice constant and thermal expansion coefficient mismatches between GaN and substrates. Regarding these issue, the sapphire has been the most common substrate for GaN-based LEDs for epitaxy.[49, 50] However, it has still large lattice constant and thermal expansion coefficient mismatches and high cost issues so GaN growth on other substrates have been investigated.[51, 52] In this section, the properties and substrate processing

for GaN epitaxy are described.

- Sapphire

In the early stage of GaN growth on sapphire (single crystal aluminum oxide), the films have high dislocation density (10^{6}–10^{10} cm^{-2}) and biaxial compressive stress in the layer as it cooled from the deposition temperature due to a large lattice constant mismatch of ~15 % and a thermal expansion coefficient difference. These high defect densities reduce the charge carrier mobility, reduce the minority carrier lifetime, and decrease the thermal conductivity, all of which degrade device performance. In addition, the thermal coefficient mismatch issue becomes severe as the thickness of the films increases causing cracks on both the films and the substrate.

However, most recently, the dislocation density becomes lower less 10^{6} cm^{-2} by substrate engineering and growth parameter optimization. Researcher recently reported that InGaN/GaN LEDs with ultralow TD density and improved efficiency on the sapphire substrate, on which a near strain-free GaN compliant buffer layer was grown by remote plasma atomic layer deposition. They

engineered the buffer layer to relax the strain by absorption of misfit dislocations in a region within ~10 nm from the interface, leading to a high quality overlying GaN epilayer with significantly lowered an unusual dislocation density as low as 2.2×10^5 cm^{-2}. In addition, they applied their buffer layer technique up to a 6" wafer, revealing a promising means to realize large-area GaN hetero-epitaxy for efficient LEDs and high-power transistors.

- Silicon carbide

Silicon carbide (both the 4H- and 6H-polytype) has strong advantages over sapphire for the GaN growth, including a smaller lattice constant mismatch (3.1%), and a much higher thermal conductivity. Its conductive electrical properties enable to make *n*-type electrode (or bottom electrode) on back sided of the substrate so fabrication process becomes simplified compared to that of sapphire substrates. Moreover, the polarity of the substrate can be controlled easily (silicon or carbon polarity) which makes the polarity of the GaN layer controllable. However, SiC does have its disadvantages; poor wetting between GaN and SiC resulting in direct epitaxy of GaN on SiC challenging. This issue

has been addressed by using a buffer layer including AlN or $Al_xGa_{1-x}N$, but these layers increase the resistance between the device and the substrate.[53] Furethermore, the cost of silicon carbide substrates is high, and currently single crystal SiC is produced by relatively few manufacturers.

- Silicon

Silicon (Si) has many advantages over the sapphire substrate including high quality, large size and low cost. However, it is difficult to grow single crystalline GaN directly on the Si substrate because of the large mismatches of the lattice constant and thermal expansion coefficient. These mismatch has limited the thickness of crack-free GaN film growth on Si to less than 5 μm. Especially, for the thin films, severe GaN layer cracking and substrate bowing appears when the thicknesses exceed 1 μm. In order to minimize the severe wafer bowing effects, selective area growth (SAG) of GaN layers on patterned Si substrate has been investigated to relax the strain by confining the area of GaN growth. However, the thickness faced limitations below 2 μm, which is still lower, whereas much thicker layers are required because it is known that the growth of thick layers in

lattice mismatched materials can lead to annihilation and reduction of the dislocation densities. Recently, Atsunori et al. demonstrated growth of thick (19 μm), crack-free, and pure GaN layers on Si with the lowest threading dislocation density of 1.1×10^7 cm^{-2} by investigating geometrical effects and surface faceting to dilate thermal stresses at the surface of selectively grown epitaxial GaN layers on Si.[54] With these advances, the first vertical GaN metal–insulator–semiconductor FETs (MISFETs) on Si substrates with low leakage currents and high on/off ratios paving the way for a cost-effective high power device paradigm on an Si CMOS platform are demonstrated.

2.2.2. Next generation nitride-based optoelectronics: flexible & high-resolution LED

Although the growths of high quality GaN films on single crystal substrates are well established, difficulties in separating the films from a single-crystal substrate arising from strong bonding between GaN and sapphire and their high mechanical and chemical stability have limited their applications on flexible LEDs. For this reason, as mentioned above, laser lift-off technique has been used

to separate GaN films from the sapphire substrate and transferred onto targeted substrate by pick-and-place technique.[6] The GaN layer can be separated from sapphire substrates by irradiation of high power pulsed laser from the back side of the substrate. The laser decomposes the interfacial GaN since the absorbed energy selectively heats up the material. These Lift-off processes have been investigated by many studies. Kelly et al. reported the pulsed laser-assisted thermal etching of GaN using the third harmonic of a Q-switched Nd:YAG laser.[55] Wong et al. have also reported pulsed UV laser processing of GaN thin films using a KrF excimer laser.[6] They present the lack of detectable degradation of GaN crystal quality during the lift-off and transfer process.

Meanwhile, to fabricate flexible LEDs with large scalability, J. H. Choi et al. successfully demonstrated flexible LEDs based on GaN microstructures grown on a glass substrate.[56] They developed the growth of GaN LEDs on glass that consisted of nearly single-crystalline pyramid stack [n-GaN (core)/InGaN-GaN multiple-quantum well (MQW)/p-GaN (shell)] arrays using a hole-patterned SiO_2/LT-GaN/Ti/glass substrate. To realize fully flexible, surface-emitting GaN

LEDs, they devised the technique to reduce the adhesion strength of the LT-GaN/Ti hetero-interface by engineering the Ti interlayer to transform to nanovoids. Then, using further interface process, the GaN microstructures successfully embedded into ultrathin, flexible substrates showing stable light emission under various bending states and stretched conditions.

Those lift-off techniques have been further investigated to monolithically integrate RGB pixels on a single substrate.[57-59] The RGB pixels, independently fabricated from different substrates were transported to the target substrate through multiple transfer steps of (pick-up and drop-off). However, for an ultra-high resolution display, the large amount of individual process to align many subpixels makes the process challenging.[60, 61] In addition, the very small size of each element drastically limits the process yield regarding very precise alignment process.

Meanwhile, it is well-known that LEDs enable to cover the entire visible spectral range depending on In contents in InGaN layers in MQWs. This intrinsic characteristic enables various color emissions from different GaN microstructure-

based LEDs. This motivates the researcher to propose monolithic integrations of various GaN microstructures on a single substrate by simultaneous growth of the GaN microstructures have been proposed.[62-64] By growing MQWs and *p*-GaN layers on them, RGB pixels can be monolithically fabricated with precise material engineering processes. Most recently, as shown in **Figure 2.8**, Robin et al. presented simultaneous growth of independent core-shell structures emitting at different wavelengths by SAG.[62] By using different growth masks, they grew elongated nano-rods, micro-platelets, and pyramid-like structures on a sapphire substrate. The nano-rods is dominantly consisted of non-polar sidewalls, while the micro-platelets have polar top facet covering more than 80% of the surface. QWs deposited on these structures exhibit independent and well-separated emissions for all visible ranges.

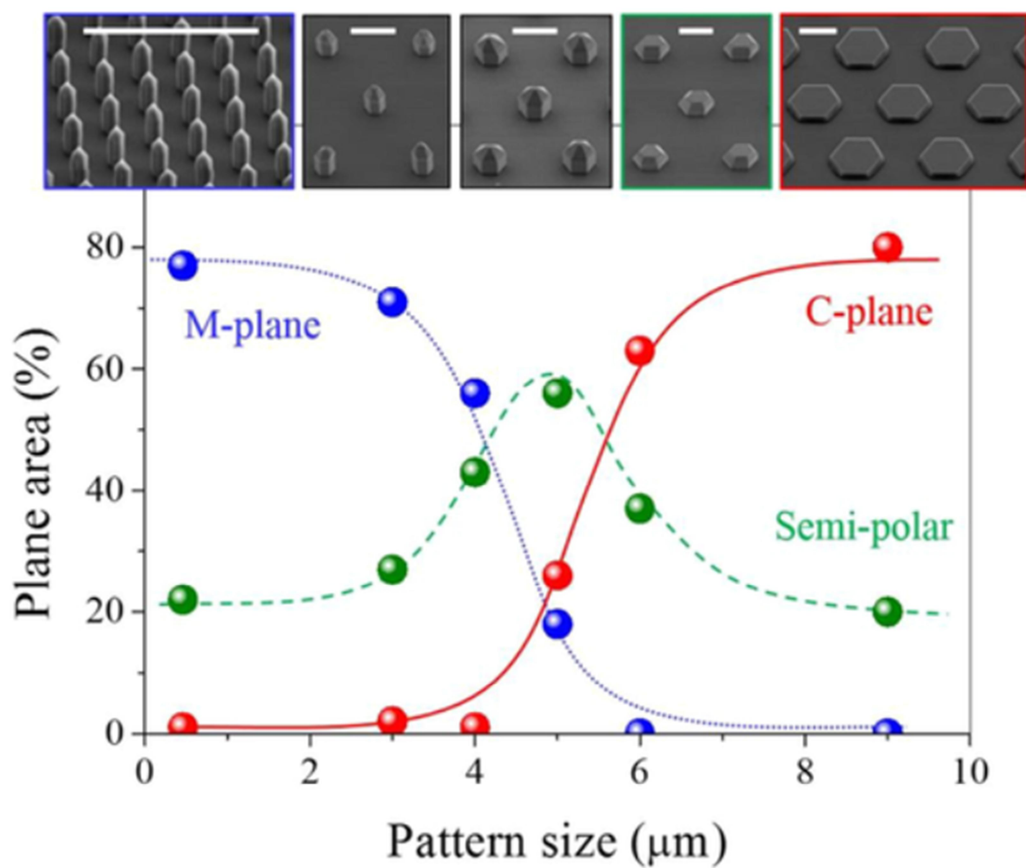

Figure 2.8. SEM pictures (45° tilted) of various micro□crystals simultaneously grown by pulsed SAE. Estimated polar, semi□polar, and non□polar surface contributions are reported for each pattern size. Scale bars represent 5 μm.[62]

2.3. Hybrid dimensional material systems for flexible electronics and optoelectronics

Although the growths of high quality GaN films on single crystal substrates are well established and their applications on flexible optoelectronics have demonstrated, the restricted substrate size and high cost of the rigid single crystal substrate limit their applications on large scale & flexible devices. For large-area or flexible-device applications, the device must be fabricated on glass, plastic, or metal substrates that is available for large scale manufactures. However, high-quality films can be grown only on a lattice-matched single-crystal substrate at a high growth temperature where those kinds of substrates have no tolerance. Growths of inorganic nanostructures and thin films on two-dimensional (2D) materials have attracted many attentions since 2D materials can be synthesized large scales over 30-inches using the roll-to-roll process.[65] Moreover, 2D materials have excellent mechanical/chemical/thermal stability which enable them to be used as substrates for the high-quality inorganic material growth.[66] This section describes growth of inorganic nanostructures and thin films on 2D

materials (hybrid-dimensional materials) and their applications on flexible electronics and optoelectronics.

2.3.1. Growth of oxide & nitride nano-/micro-structures on graphene layers

Among various inorganic semiconductors, ZnO nanostructures including nanorods and nanowalls were firstly grown on mechanically exfoliated graphene using catalyst-free metal-organic chemical vapor deposition (MOCVD) system (**Figure 2.9**).[67] The growth behavior of ZnO nanostructures on graphene was investigated using scanning electron microscope (SEM) and transmission electron microscope (TEM). ZnO nanorods exhibited good vertical alignments on pristine graphene layers. However, the density of the ZnO nanorods is low to fabricate highly packed devices. The origin of the low density growth was considered by the lack of chemical reactivity of graphene surfaces because the high density of ZnO nanostructures was observed at the graphene step edges: ZnO nanowalls or high density nanorods were grown along the graphene step edges. Moreover, this result motivated the growth of different microstructures with different densities on graphene layers with a precise control of the graphene step edges.[68]

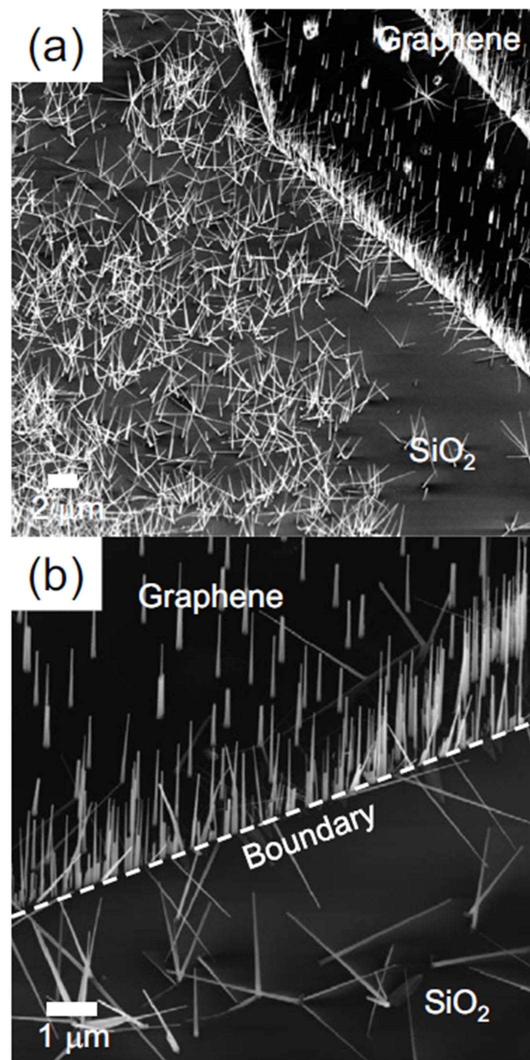

Figure 2.9. FE-SEM image of ZnO nanostructures grown on the graphene layerstransferred onto the SiO2 / Si substrates.[67]

To further investigate the origin of the growth and epitaxial relations of ZnO nanostructures on the graphene using TEM, graphene films were transferred on TEM grid and ZnO nanostructures were then grown on the graphene films for the sample preparation. As shown in **Figure 2.10**, the high resolution TEM image and diffraction patterns of ZnO and graphene clearly showed their epitaxial relationship: wurtzite ZnO exhibited a 3:4 lattice match with graphene.[69]

Meanwhile, InAs nanowires were grown on mechanically exfoliated graphene layers, using MOCVD[70, 71] or MBE[72, 73]. In similar to the ZnO growth on graphene films, the epitaxial growth of InAs was confirmed by TEM analysis even though there exists lattice mismatch.[73]

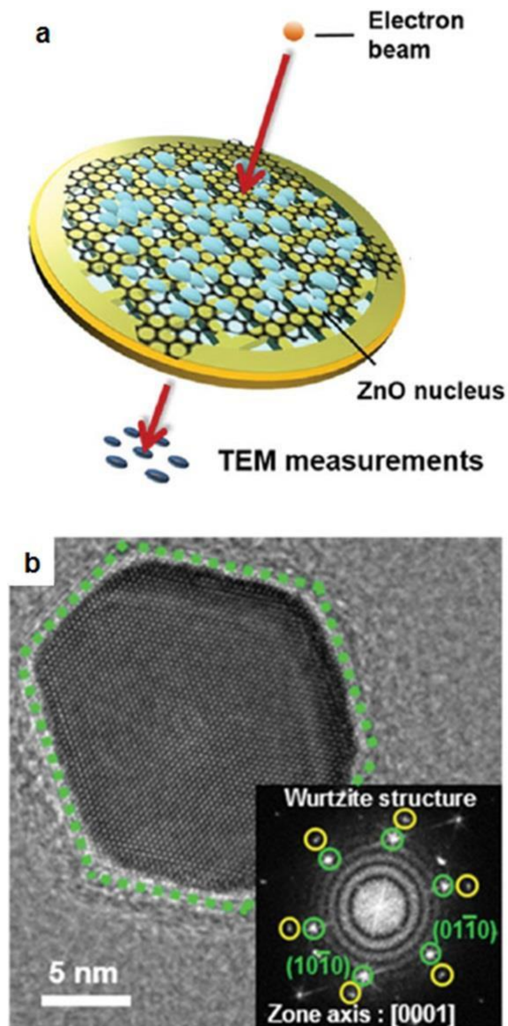

Figure 2.10. (a) Schematic illustration of ZnO nanostructures grown on graphene coated TEM grid for TEM analysis. (b) HR-TEM image of ZnO grown on graphene. The inset shows diffraction patterns of ZnO and graphene.[69]

ZnO and InAs are well-known wide and narrow band gap materials. They have been fabricated to various optoelectronics using their intrinsic characteristics. The growth of ZnO and InAs on graphene films motivated fabrications of flexible optoelectronics. Meanwhile, to enhance the uniformity of the nanostructures for reliable device performances, position-controlled ZnO growth was demonstrated on graphene films using SiO_2 growth mask prepared on graphene films. The position-controlled growth technique was further investigated to grow the ZnO nanostructures on CVD-graphene films for their large scalability. Park et al. successfully grew position controlled ZnO nanotubes on 2-inch Si substrate where CVD-graphene films were transferred onto (**Figure 2.11**).[8]

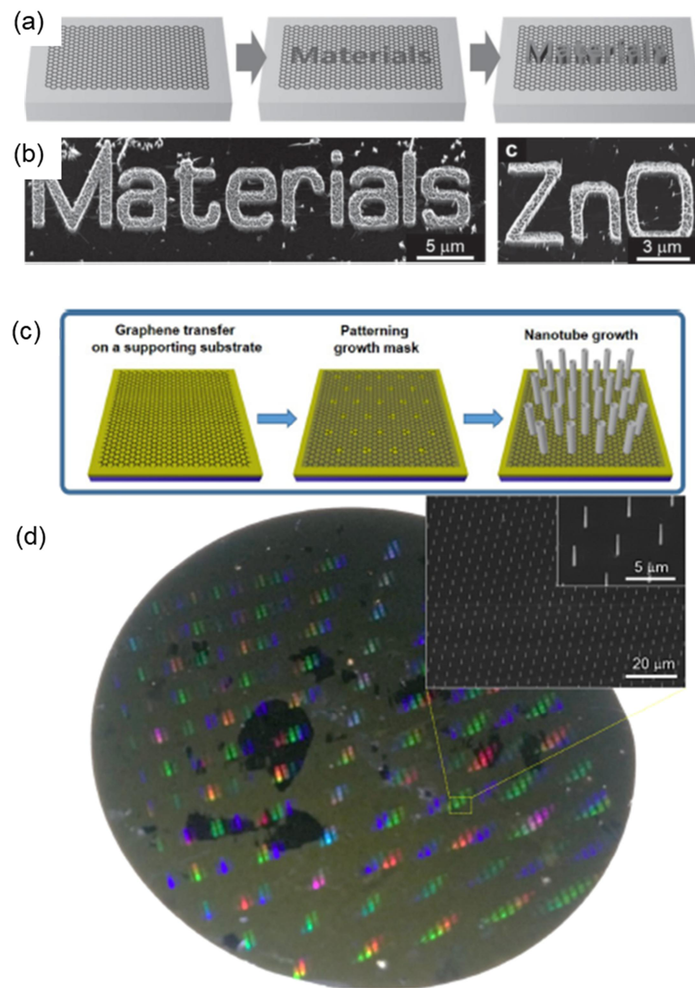

Figure 2.11 Controlled growth of ZnO nanostructures on graphene layers. (a) Schematic illustration of growing position-and morphology-controlled ZnO nanostructures on mechanically exfoliated graphene layers, (b) SEM images of resulting ZnO nanostructures. (c) Strategy of growth of ZnO nanotube on CVD graphene layers. (d) Photographs of ZnO nanotube grown graphene/Si wafer. (inset) Magnified SEM images of the ZnO nanotubes.[8]

Based on the position-controlled ZnO growth, uniform GaN nano/microstructures were able to be grown on graphene films by hetero-epitaxy of GaN layers on ZnO nanotubes.[68] The interface between the GaN and ZnO was investigated using TEM and their epitaxial relationship was confirmed. Yoon et al. investigated the relationship between misfit dislocations and crystal shape by examining highly localized symmetric dislocations in the [10–10] direction for GaN/ZnO nanotubes. They were mostly edge-type dislocations with Burgers vector 1/3 [11–20]. The highly localized nature of the dislocations is attributable to the geometry of the nanostructure in the presence of stress at the vertical and lateral interfaces.[74]

Meanwhile, rather than the nanostructure growth, thin films are difficult to be grown directly on graphene films because the nucleation of materials is confined by step-edge or defect sites of the graphene films where the dangling bonding density is high. To circumvent this problem, ZnO nanowalls were employed as an intermediate layer. Then, a lateral growth of ZnO was performed to coalesce the nanowalls becoming merged structures.[75] Similarly, GaN thin

films were grown on the ZnO nanowalls.[76] In more detail, the predominant dislocations in the GaN thin films grown on ZnO nanowalls, prepared on graphene films (**Figure 2.12**). The TEM investigation confirmed that they have mixed-type dislocations. The typical threading dislocation density in the films was determined to around 10^9 cm^{-2}, which is comparable to that of GaN on Si substrates and slightly higher than that of GaN on sapphire substrates (**Figure 2.13**).

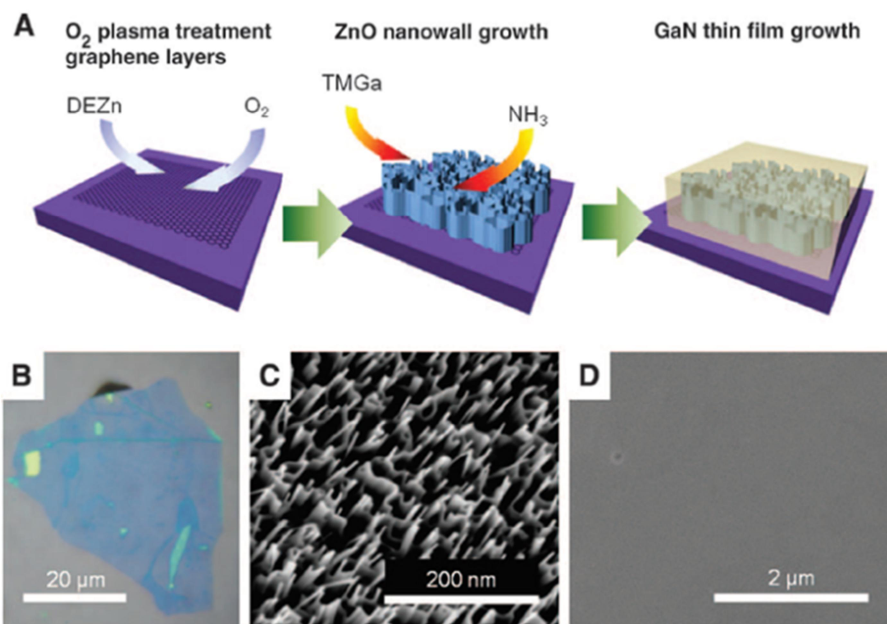

Figure 2.12 Growth of GaN thin-film on graphene layers using ZnO nanowall as an intermediate layer. (a) Schematic illustration of heteroepitaxial growth of GaN thin-film on graphene layers using ZnO nanowall networks. (b) Microscope image of the mechanically exfoliated graphene layers. (c) SEM image of dense ZnO nanowall networks. (d) SEM image of the grown GaN thin film showing flat surface morphology.[76]

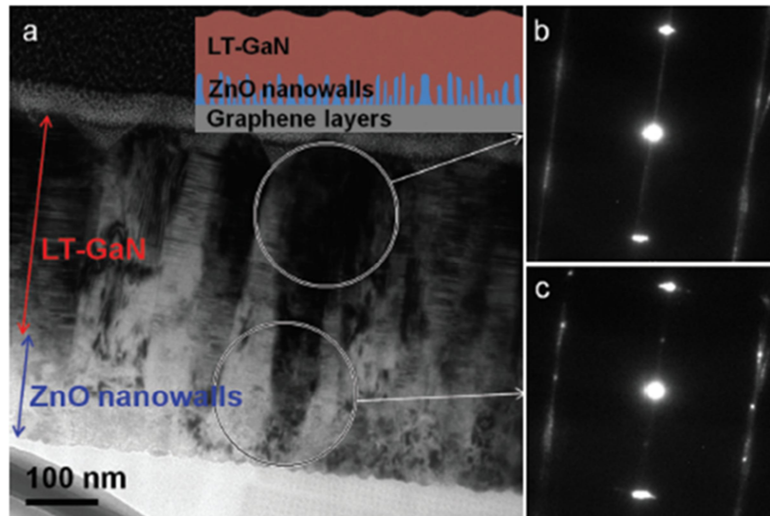

Figure 2.13 Microstructure of the GaN thin film grown on graphene layers. (a) Low-magnification cross-sectional image of the GaN/ZnO/graphene heterostructure. (b, c) Selective area diffraction patterns from the circle-marked area in (a).[77]

2.3.2. Functional devices using hybrid dimensional material Systems

Epitaxial ZnO nanostructures on graphene films grown by MOCVD enable the material exhibits excellent intrinsic material characteristics.[67] As shown in **Figure 2.14**, free exciton emission peaks were observed from the low temperature photoluminescence (PL) spectra. Moreover, it was confirmed that GaN microstructures grown by hetero-epitaxy have comparable dislocation densities to that of GaN on Si. Those high-quality nanostructures on graphene films have been fabricated to various flexible electronics and optoelectronics. This section describes a general review of those devices.

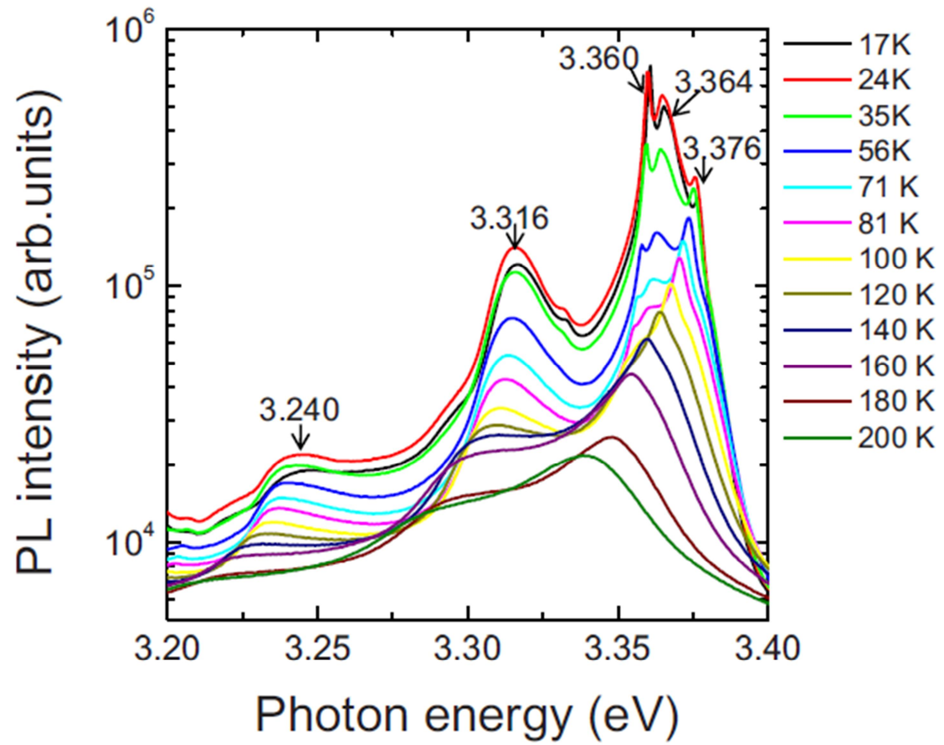

Figure 2.14. Temperature dependent PL spectra of ZnO nanostructures grown on graphene layers.[67]

2.3.2.1. Electronics

Oh et al. reported a VFET consisting of ZnO nanotubes on CVD-graphene films.[9] Due to the high quality of the single crystal ZnO nanotubes and the unique 1D device structure, the fabricated VFET exhibits excellent electrical characteristics including a small subthreshold swing of 110 mV dec^{-1}, a high I_{max}/I_{min} ratio of 10^6, and a transconductance of 170 nS μm^{-1}. The VFETs can be easily transferred onto flexible substrates showing reliable and high performances without significant degradations.

Tchoe et al. demonstrated individually addressable, high-density ZnO nanotube Schottky diode arrays (**Figure 2.15**).[78] Their electrical characteristics were investigated by current (I) – voltage (V) measurements showing conventional diode characteristics. Moreover, the photo-responses of the arrays were investigated by measuring their spectral responses and $I - V$ characteristics under light illuminations showing maximum photocurrent to dark current ratio of 1,400 and responsivity of 10^6 A/W.

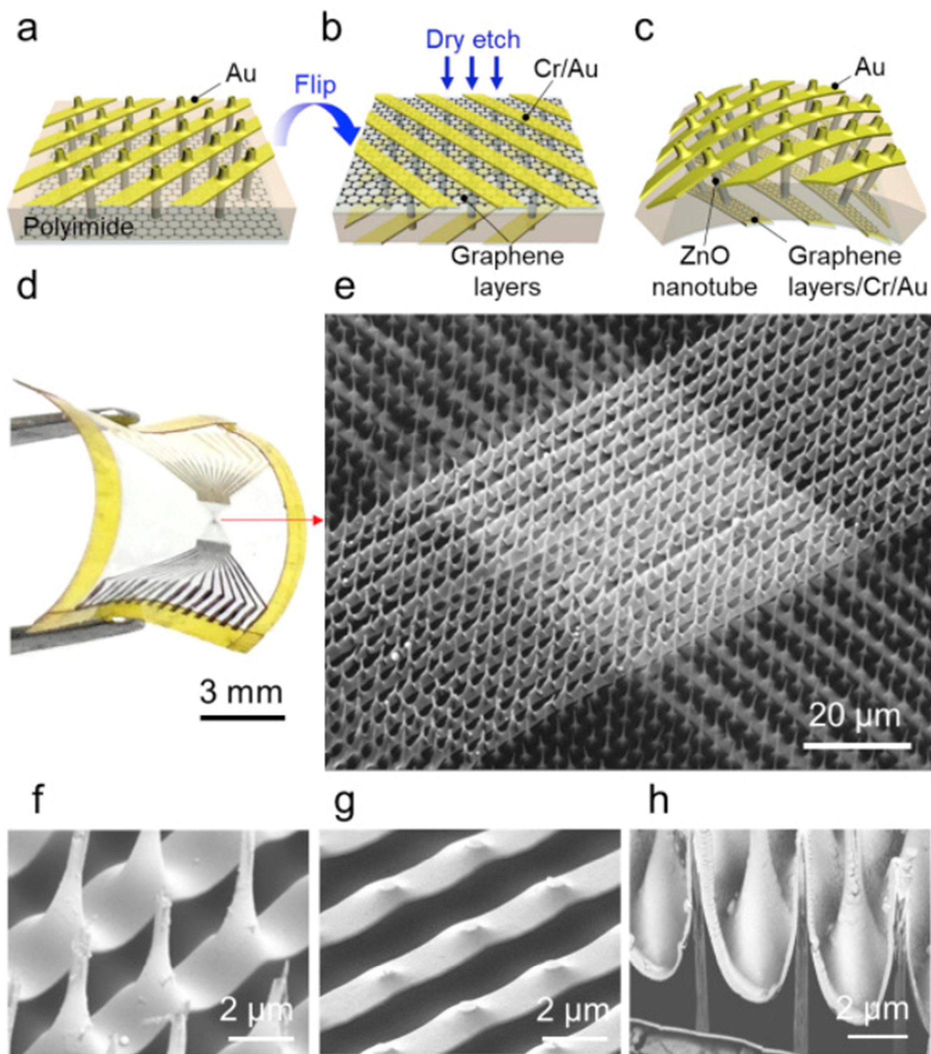

Figure 2.15. Fabrication of a nanotube crossbar array by (a) designing gold (Au) electrode lines as Schottky contacts on the top surface of the ZnO nanotubes and (b) deposition of chromium (Cr)/Au electrodes, followed by a reactive ion etching process, to create graphene layers/Cr/Au electrode lines as ohmic contacts on the bottom surface. (c) Overall structure of the nanotube device array with Au and

graphene layers/Cr/Au electrode lines contacting individual nanotubes. The top and bottom electrodes are cross-aligned. (d) Photograph of the ultrathin and flexible nanotube device array. (e) Tilted SEM images clearly demonstrating precise alignment of the (f) top and (g) bottom electrodes with the ZnO nanotube device array. (h) Cross-sectional SEM image of the nanotube device array.[78]

2.3.2.2. Optoelectronics

Chung et al. demonstrated transferrable LEDs by growing GaN thin films on ZnO nanowalls prepared on graphene films then transferring them onto arbitrary substrates.[76] The LEDs show strong light emissions on any kinds of substrates where LEDs were transferred onto. Lee et al. fabricated flexible LEDs by hetero-epitaxy growth of GaN layers on ZnO nanotubes grown on graphene films.[10] The nanostructured GaN LEDs on graphene films performed stable and strong light emissions in a flexible form even under many times of the bendings. Moreover, Chung et al. and Park et al. further optimized inorganic nano/microstructure growth on CVD-graphene films enabling their applications on large-scale flexible devices.[8, 11] Chung et al. demonstrated transferrable LEDs by growing GaN thin films on CVD-graphene films with pre-grown ZnO nanowalls.[7] However, CVD-graphene films have many grain boundaries because they are grown on polycrystalline metal foils. Those grain boundaries affected on in-plain direction of the inorganic semiconductors grown on them resulting in severe crack issues on GaN thin films. To address this issue, as shown in **Figure**

2.16, they grew GaN microstructures on micro-patterned CVD-graphene films. The CVD-graphene films are patterned to arrays of the microdot with a diameter of ~5 μm which is comparable with a size of the single grain of the CVD-graphene films. Then, ZnO nanowalls were grown selectively on those microdot arrays as an intermediate layer. Subsequently, using lateral growth technique, high quality GaN microdisks were able to be grown on ZnO nanowalls. Consequently, they performed strong light emissions and operated reliably under many times of the bendings because of the deformable characteristics of the array.

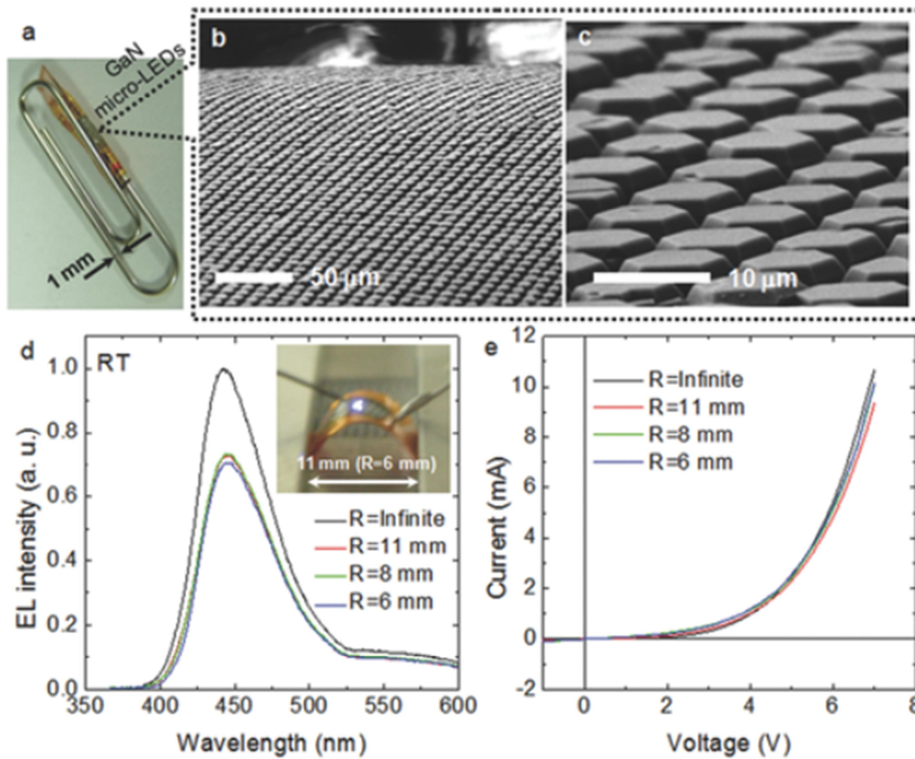

Figure 2.16. Bending test of the GaN micro□LED array. a) Optical image of GaN micro□LEDs wrapped around a 1 mm diameter paper clip. b) Low□magnification and c) high□magnification FE□SEM images of GaN micro□LEDs under bending radii of 0.6–0.8 mm. d) Room temperature EL spectra and e) *I–V* curves of the micro□LEDs under various bending radii. The inset in (d) shows a light emission image of the micro□LEDs at a bending radius of 6 mm.[7]

Experimental Techniques

3

3.1. Growth techniques

This section describes the equipment and techniques to grow materials used for experiment.

3.1.1. Metal-organic vapor-phase epitaxy system

Metal-organic vapor-phase epitaxy (MOVPE) is an advanced chemical vapor deposition method of epitaxial growth of materials with very pure high quality metal-organic precursors. To grow high quality inorganic semiconductors, metal-organic chemical vapor epitaxy (MOCVD) systems were built for the growth of GaN and ZnO nano/microstructures. MOCVD systems consist of gas delivery system, growth chamber, substrate heating system, and low pressure pumping-exhaust system as described in following.

3.1.1.1. Gas delivery system

Figure 3.1 shows gas delivery system of nitride semiconductor MOCVD. Air actuated pneumatic valves (Fujikin Inc. FPR-UDDFCL-7106.35) controlled the gas directions and flow rates with 12 channel pneumatic gas manifold control card (Clippard Instrument Laboratory Inc., No. EMC-08-24-30) and mass flow controls (MFCs) (Tylan Co. FC-280S, Celerity Co. TN280, Mykrolis Co. FC-280S) with 12-channel MFC controller (DFC4000), respectively. Bellows-shield metering valve (Swagelok Inc. SS4BMG) controls line pressures of reactants and dopants, and their pressures were monitored by baratron pressure gauge (MKS Co. 870B). Their gas lines were made by electro-polished 316-stainless steel (SS) tubing with sizes of 1/4" or 1/2". VCR fittings with SS gaskets (SS-4-VCR-2, Swagelok, Co.) were used for all tubes.

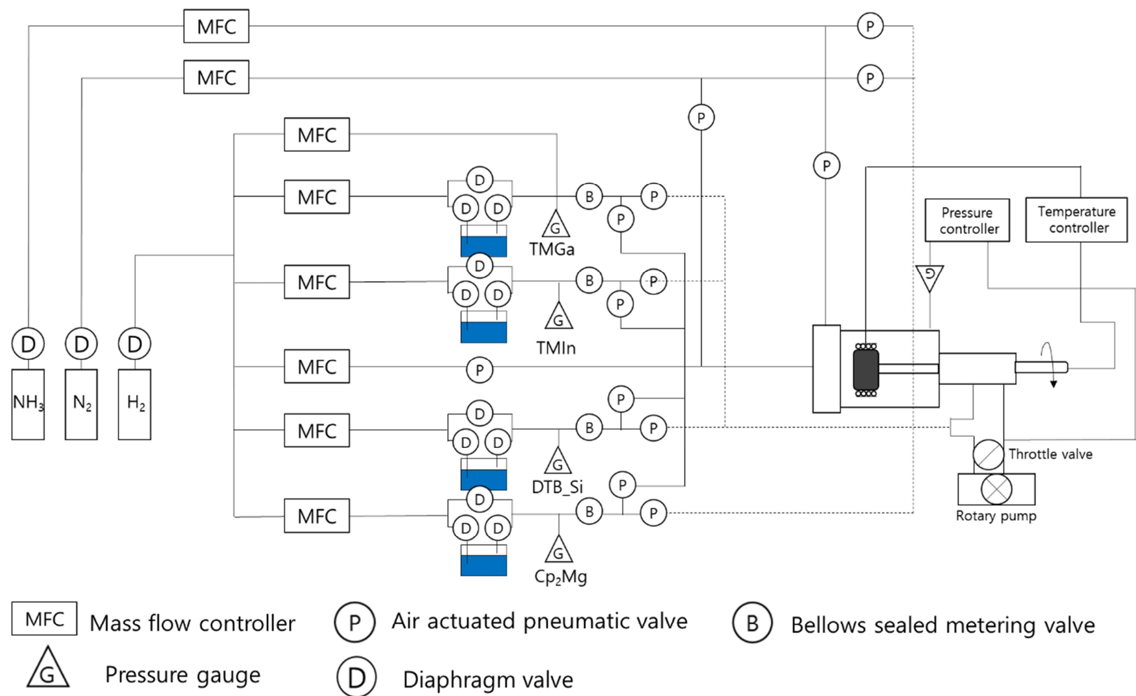

Figure 3.1. Schematics of gas delivery systems

3.1.1.2. Reactor and temperature controller

Two kinds of reactor were designed for III-nitride and ZnO MOVPE system. A vertical type rotating reactor with SS chamber (SYSNEX 1×2” reactor) is employed for III-nitride reactor. SiC coated graphite susceptor with a size of 2 inch is used for high purity GaN growth. A rotation feedthrough connected with a rotation motor and a belt allows rotations of the susceptor. A showerhead

connected with SUS lines of the precursors improves the uniformity of growth rate or composition over the entire substrate surface.

Meanwhile, the ZnO reactor made of a fire polished tube quartz (material grade: GE-214), with 90 mm-width and 300 mm-length, and two 316-SS ultratorr fitting flanges on both ends. The substrate is loaded on a graphite susceptor inside the reactor and heated by a ratio frequency (RF) induction heater (Eltek, Inc., 20 kW for SYSNEX chamber and 10 kW for ZnO reactor). The temperature of graphite susceptor is measured by the K-type (or R-type) thermocouples. The temperature was controlled by a proportional-integral-derivative (PID) type temperature controller (Chino Co. KP1000).

3.1.1.3. Exhaust disposal system and low pressure pumping system

The exhaust throttle valve (MKS Co. No. 253B) connected to a series of vacuum component for rotary pump (Edward Co. E2M28-chmical type, pumping capacity: 550L/min), reactor pressure control, and manual angle valve. A baratron pressure gauge (MKS Co. No. 628B-BTBE1B capacitance manometer type) was

placed near the reactor to read vacuum levels accurately. The reactor pressure is controlled by the batron gauge and the exhaust throttle valve in the range of 0.1 to 1000 Torr with a support from PID pressure controller (MKS Co. 651C). During the growth, the by-product gas phase chemicals were blown out through the exhaust tubing lines and disposed by a scrubber system (Tera Tech Co. NSHW400) where the toxic and explosive gases and particles are burnt then washed out in water.

3.2. Structural characterization

3.2.1. Morphology investigation

The materials grown for the experiments were analyzed using a JEOL scanning electron microscopy (SEM) and Carl zeiss field emission SEM. The images were obtained at working distances of 5–10 mm and high accelerating voltages in the range of 5–30 keV.

3.2.2. Crystallographic and microstructural investigations

3.2.2.1. Transmission electron microscopy

Microstructural analysis was performed using high-resolution transmission electron microscopy or scanning transmission electron microscopy (HR-TEM or STEM; a Philips Tecnai UT-30, FEI F20, JEOL-2100FS). The TEM sampling was performed by focused ion beam (FIB). For the cross-sectional inspections, samples were milled with 30kV-accelerated Ga ions using FIB machine (FEI Co. NOVA 200 NANOLAB) in the dual beam mode.

3.3. Optical Characterization

3.3.1. Photoluminescence and electroluminescence spectronscopy

For optical characteristic measurements, Photoluminescence (PL) measurement was performed by a continuous wave He–Cd laser (325 nm) and pulsed wave Nd:YAG laser (355 nm) as the excitation source. The luminescence of the samples was collected through the slit of a spectrometry (Dongwoo Optron Co. MonoRa 320i with charge coupled device), and dispersed though the spectrometry with grating. PL spectra was analyzed by charge coupled device

(CCD)-attached dual grating monochromator. The electroluminescence (EL) was measured using a microscope (Carl Zeiss Co. No. Axioskop 2 MAT) monocrometer (Dongwoo Optron Co. MonoRa 150i) with CCD was used for spectrum analysis.

3.4. Electrical characterization

3.4.1. Current–Voltage measurement

Current–Voltage measurements including LED and ReRAM operations were carried out under the dc operation (Keithely 2400) at room temperature.

Flexible ReRAM based on hybrid dimensional material systems

4

4.1. Introduction

Researches about flexible electronics have been widely performed to satisfy recent demands on the portable devices including mobile phones and bio-medical sensors.[79, 80] Among them, the memory devices are a crucial component due to its important roles in the device such as data storage and communication with other components. Especially, ReRAM have attracted attention due to its advantages appropriating with the flexible electronics such as low power consumption, fast operation speed, high scalability and simple device structure.[81-83] To demonstrate flexible ReRAM, researchers have investigated a variety of organic based flexible ReRAM fabricated at relatively low temperature using spin coating method.[84, 85] Although the organic based flexible ReRAM show stable resistive switching performances, there are significant challenges in non-

compatibility with industries which is one of the advantages in the ReRAM. To address the problems, inorganic based ReRAM has been fabricated on the flexible substrates by low temperature physical vapor deposition (PVD) technique.[39, 86] However, due to limitation in its material structure which is thin film based structure, the resistive switching characteristics were degraded when it is performed in a flexible form. To overcome the limitation, herein, we demonstrate inorganic based flexible ReRAM composed of ReRAM disk arrays on graphene films. The Pt/NiO layers were deposited on *n*-GaN disk arrays prepared on CVD graphene films using sputtering and metal-organic chemical vapor deposition (MOCVD). The resistive switching characteristics are conserved in a flexible form even after 1000 times of the bending due to the isolated material structures. Moreover, even at 450K, stable resistive switching characteristics were obtained which indicates good durability of the device in harsh conditions.

4.2. Growth of oxide/nitride hybrid structures on graphene layers

This section describes growth process of oxide and nitride hybrid structures on CVD-graphene films.

4.2.1. ZnO nanowall growth CVD-graphene films

Firstly, graphene thin films synthesized on Cu foil are transferred onto SiO_2/Si substrates. Then, SiO_2 growth mask is deposited on the graphene thin films with periodic hole array. Diameter of the hole is 25μm and patterned by photolithography technique. ZnO nanowalls were selectively grown on exposed graphene films using catalyst-free low-pressure MOVPE. High-purity diethylzinc (DEZn) and oxygen were used as reactants for the ZnO nanowalls, and high-purity argon was used as the carrier gas. The flow rates of DEZn and oxygen were 3 and 20 sccm, respectively. The reactor pressure and temperature during the growth were maintained at 0.3 Torr and 600° C, respectively.

4.2.2. Growth of GaN microdisk arrays

The ZnO is vulnerable to H_2 ambient gas and high temperatures where are ideal conditions high-quality GaN growth. To protect ZnO nanowalls during the GaN growth, an LT-GaN buffer layer was grown on the ZnO nanowalls with

sufficient thickness. For the LT-GaN growth, nitrogen atmosphere was formed with the reactor pressure and temperature of 200 Torr and 500 °C, respectively.

After the LT-GaN growth, high-quality GaN layers were grown at 1060 °C. During the growth, we restricted continuous flow of NH_3 to perform pulsed mode growth to introduce low Ⅴ/Ⅲ ratios for lateral growth while the Ga precursor continuously flowed into the reactor. As shown in **Figure 4.1**, 25μm-wide GaN microdisk arrays were grown on CVD-graphene films.

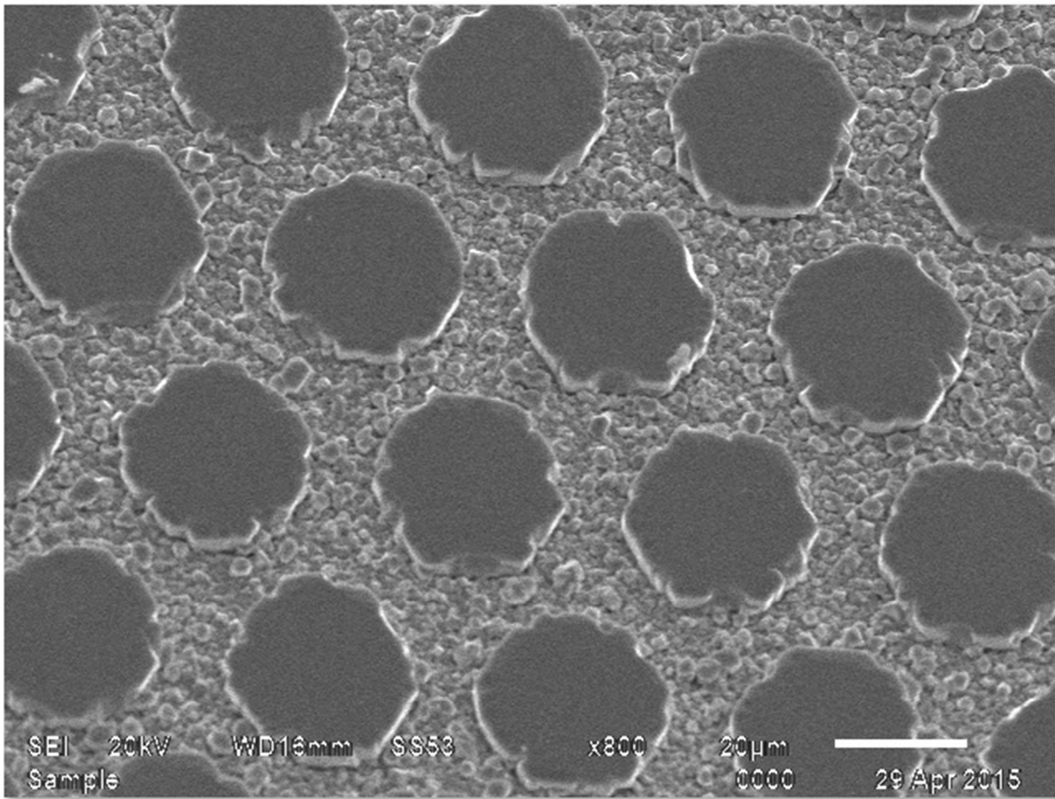

Figure 4.1. SEM image of GaN microdisk arrays

4.2.3. Growth of resistive switching layers

Subsequently, as a resistive switching layer, a 35-nm-thick polycrystalline NiO was deposited by DC reactive sputtering on the *n*-GaN disk array at 500°C and 1.5 mTorr pressure in an Ar + O_2 gas mixture (7% O_2).

4.4. Fabrication of flexible ReRAM

General schematics of flexible ReRAM fabrications are illustrated in **Figure 4.2**. Au top electrodes are selectively deposited on the NiO with diameters of 20μm using aligned photolithography technique, DC reactive sputtering, and a conventional lift-off process. Consequently, ReRAM disk arrays composed of Au/NiO/*n*-GaN are successfully fabricated on the CVD graphene films.

To transfer the ReRAM disk arrays/CVD graphene films onto the flexible substrate for instance plastic or metal foil, thermal release tape which loses its sticky properties up to ~100°C is applied on the devices then binds them during exfoliation from the SiO_2/Si substrate. Subsequently, thermal release tape/devices are flipped over (**Figure 4.3**) and PMMA is coated as a holding layer on the

bottom of the devices which is CVD graphene films. For both detachment of the thermal release tape and stiffening of the PMMA, these are baked at 180°C for 1 minute and transferred onto plastic substrate for easy handling.

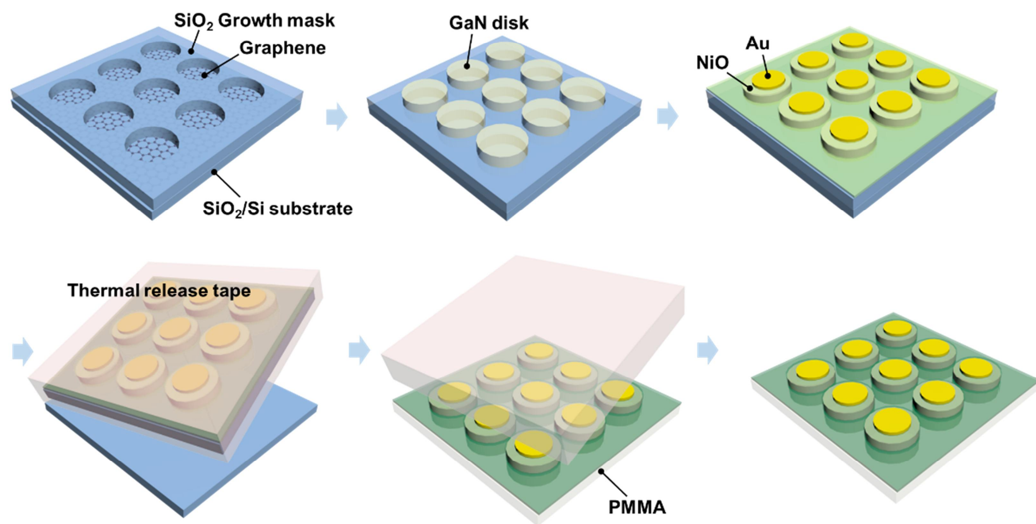

Figure 4.2. Schematics of the oxide/nitride/graphene hybrid material system growth and its device fabrication process.

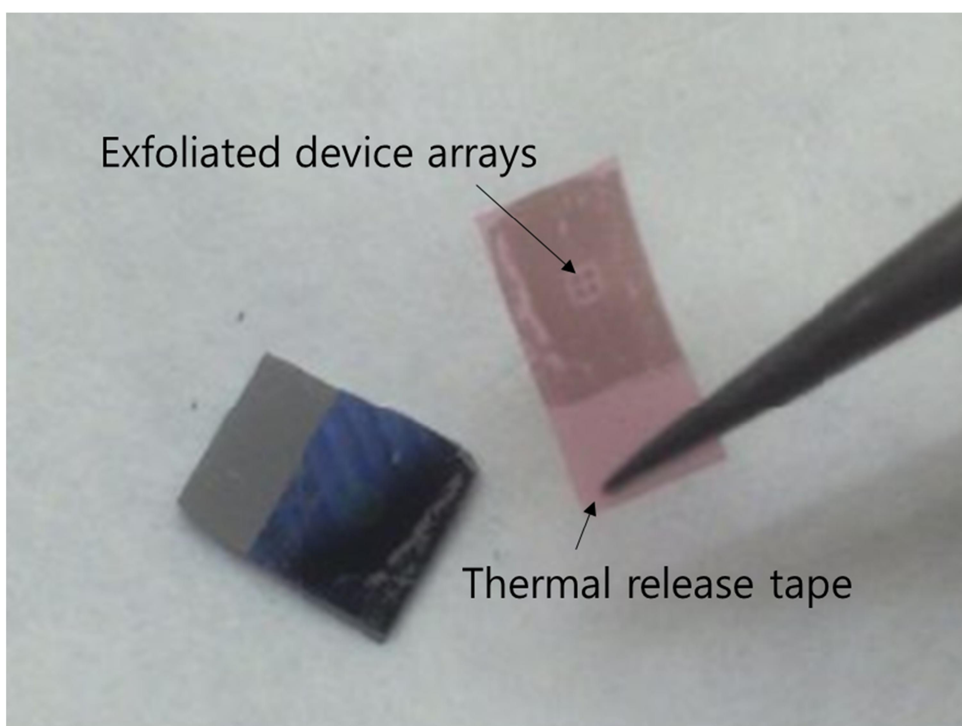

Figure 4.3. Releasing the device arrays using the thermal release tape.

4.5. Resistive switching characteristics

The resistive switching characteristics are measured by keithley 2400 sourcemeter with two tungsten tips which are placed on Au and graphene. As shown in **Figure 4.4**, *I–V* characteristic curves of the ReRAM disk clearly show unipolar resistive switching behavior during variously strained states including flat, bent and rolled states. Sweeping the voltage to positive values above a certain operation voltages of V_{set} or V_{reset} with an appropriate compliance current allows an abrupt increase or decrease in the current level. This voltage sweep modifies resistance states of the NiO film to non-volatile low resistance state (LRS) or high resistance state (HRS). Regardless with strains from the substrate, stable unipolar resistive switching behaviors were obtained without any degradation or fluctuation indicating that the ReRAM disk is rarely affected by strains from the substrate. Furthermore, the hybrid structures show semi-transparent behavior as displayed in inset of the Figure 2. We believe that the oxide/nitride/graphene material system is able to be applied on even transparent electronics through replacement of the top electrode/oxide layers from Au/NiO to transparent top

electrode(Indium-tin-oxide, ITO)/oxide(ZnO, TiO_2) layers because the nitride/graphene material system is already transparent itself.

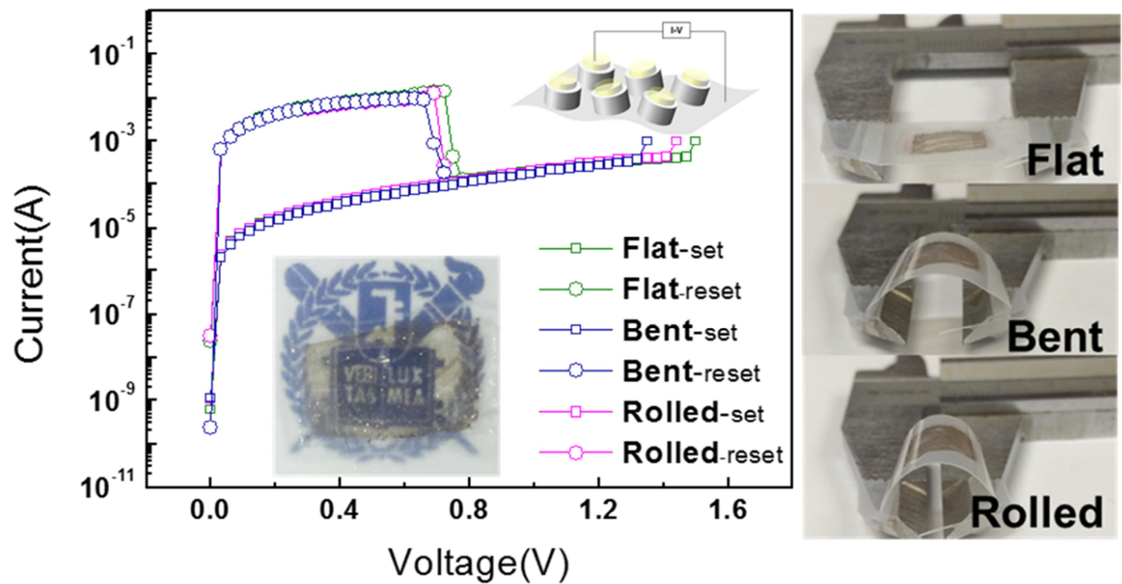

Figure 4.4. *I–V* characteristic curves of ReRAM disk at variously strain states including flat, bent, and rolled states. Inset shows a photograph of the device showing semi-transparency.

For more detail analysis about resistive switching characteristics, we perform 100 times of resistive switching and investigate its *I–V* characteristics. According to the cumulative probability introduced in **Figure 4.5(a)**, we can clearly find that no operation voltage overlap occurs between V_{set} and V_{reset}. Specific values of the distributions and standard deviations (SDs) for each strained states are introduced in **Table 4.1**. The ranges of the distributions of V_{set} and V_{reset} for each strained states are almost similar and its SDs are compatible with each other indicating that 100 times of the resistive switching performed stably even in variously strained state.

However, according to endurance analysis (Figure 4.5(b)), resistance of both HRS and LRS are fluctuated when strain is applied. The resistances of the HRS and LRS for the flat state fluctuate in the ranges of 4 KΩ ~ 25 KΩ (open green circle) and 27 Ω ~ 64 Ω (solid green square), respectively, at constant reading voltage of 0.02 V. The fluctuation ranges of HRS and LRS for the bent state become larger in the ranges of 8 KΩ ~ 56 KΩ (open blue circle) and 45 ~ 494 Ω (solid blue square) respectively. Moreover, in case of the rolled state, the

fluctuation ranges of 6 KΩ ~ 67 KΩ (open blue circle) and 26 ~ 674 Ω (solid blue square) were obtained. However, although the fluctuation ranges of both LRS and HRS are expanded, we can confirm that resistance overlap between HRS and LRS does not appear. Figure 4.5(c) shows the retention characteristics of the ReRAM disk which ensure that the ReRAM disk is able to retain its HRS and LRS states over 8 months under reading voltage of 0.1 V. Furthermore, in comparison with the previous studies which demonstrated inorganic based flexible ReRAM using oxide thin films deposited on the flexible substrates,[39, 86] the operation parameters including operation voltage and current of the ReRAM disks are conserved well even after 1000 times of bending as shown in Figure 4.5(d).

In addition, we investigate resistive switching characteristics even at 450K, when the device is bent, to verify durability of our devices in harsh conditions at a flexible form as shown in **Figure 4.6**. In case of cumulative probability (Figure 4.6(a)) after 100 times of resistive switching, its operation voltage ranges and SDs (0.45V and 0.16V for V_{set} and V_{reset} respectively) seems to be comparable with that of 300K. Meanwhile, according to endurance analysis

(Figure 4.6(b)), when our device is operated at 450K fluctuation ranges of both HRS and LRS are slightly expanded but still overlap between two resistance states are prevented.

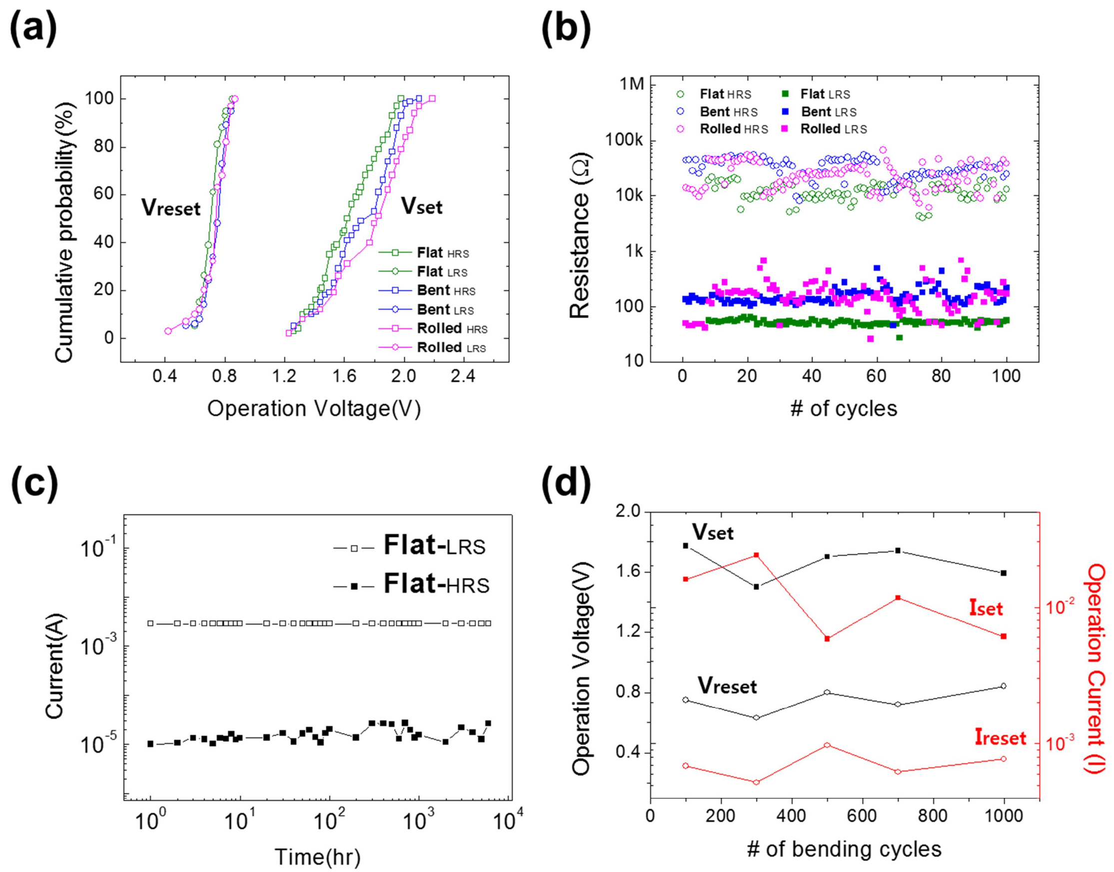

Figure 4.5. Resistive switching characteristics of ReRAM disk on plastic substrate. (a) cumulative probability, (b) endurance, (c) retention, and (d) reliability about number of bending cycles.

		Flat state	Bent state	Rolled state
Distributions of	V_{set}	1.26 ~ 1.98 V	1.26 ~ 2.04 V	1.23 ~ 2.10 V
	V_{reset}	0.60 ~ 0.85 V	0.54 ~ 0.84 V	0.42 ~ 0.84 V
SD of	V_{set}	0.34 V	0.42 V	0.35V
	V_{reset}	0.16 V	0.17V	0.15V

Table 4.1. Distributions and SDs of V_{set} and V_{reset} at variously strained state

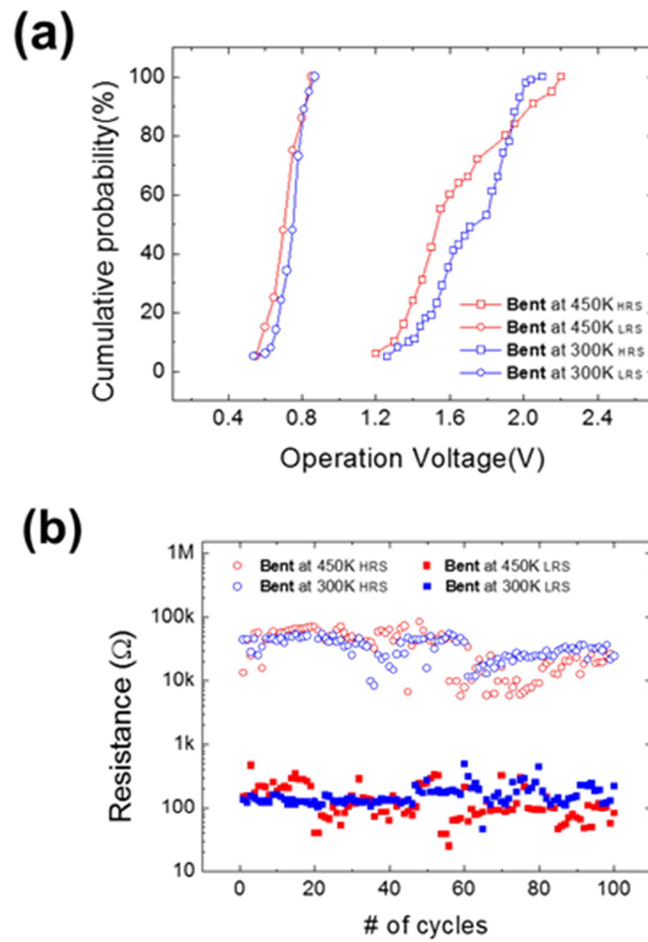

Figure 4.6. Comparison of resistive switching characteristics of ReRAM disk at 300K and 450K. (a) cumulative probability, (b) endurance.

4.6. Discussion for the mechanism of resistive switchings using oxide/nitride hybrid structures

Meanwhile, the hybrid material structures of NiO/GaN allow us to explore resistive switching dynamics by visualizing formation/rupture of the filaments during resistive switching. One of issues for LED performance enhancement is how to decrease contact resistance between top electrode and p-GaN layer. Au/Ni deposition and oxidation was used in our experiment as many researches suggested,[87, 88] and successfully decreased the contact resistance. On the other hand, many studies about NiO film as an insulator layer in ReRAM so far have demonstrated that CF formed in bulk during resistive switching is composed of percolation clusters based on Ni.[89, 90] Thus, if LRS is induced during resistive switching in the NiO thin film, light emission can be caused by the formation of Ni-based CF and its low contact resistance with the LED structure.

As commented above, ReRAM has been considered as one of promising next generation non-volatile memory to overcome limitations of Si-based flash

memory due to its advantages, such as high operation speed, low power consumption and high scalability. However, instability problem in its operation parameters is remaining unsolved and resistive switching mechanism is still controversial. Many researches have been performed to enhance stability of operation parameters through deposition parameter control,[36] fabricating heterojunction with other materials such as graphene[91] or introducing oxygen reservoir.[92] Transmission electron microscopy (TEM)[90, 93] or conductive atomic force microscopy (C-AFM)[94, 95] studies have revealed that resistive swithing is caused by formation of conducting filament (CF) in bulk or oxygen migration at interface. In addition, in-situ TEM is recently used to study time evolution of CF's and find switching mechanism.[96] However these methods have faced many weaknesses such as small observable area compared to device-scale, destructive sample fabrication such as ion milling and top electrode elimination, and poor performance of a damaged sample.[93, 95, 96] To approach more useful device-scale switching mechanism, we should develop an advanced non-destructive tool which enables real-time large-area imaging of micro-scale distribution of CF's in a

ReRAM device leading to exploring time evolution of CF’s related to fluctuation of resistive switching parameters.

In this section, a new concept for real-time large-area imaging of micro-scale distribution of CF’s during resistive switching by introducing a hybrid device of ReRAM and LED will be described. A CF formed in the ReRAM device is used as a p-type electrode from which holes are injected to a p-GaN top layer of the LED structure. When CF’s are formed in the ReRAM device, the synchronous light emission is induced by recombination of electrons and holes which are injected from an n-GaN of the LED and the CF’s, respectively, under applied electric field. Lignt emission images obtained using our ReRAM/LED hybrid device demonstrate device-scale real-time observation of rupture/formation of major CF’s which maninly cause the resistive switching, and growth of minor CF’s which distort connectivity of major CF’s leading to operation parameter fluctuation.

4.6.1. Fabrication of ReRAM/LED hybrid device

A GaN thin film was deposited on an Al_2O_3 (0001) substrate at three step temperatures of 540 °C for 2 mintues, 970 °C for 15 mintues, and 1080 °C for 1 hours with flow rates of 15 – 30 sccm for trimethyl-gallium (TMGa) followed by substrate heating at 1050 °C for 1 mintue with H_2 and NH_3. And then, a GaN-based p-n junction LED structure with $In_{1-x}Ga_xN$/GaN multi quantum well (MQW) was grown heteroepitaxially on the surface of the GaN thin film. First, a Si-doped n-GaN layer was deposited in the flow rates of 15 – 30 sccm for TMGa and 1-3 sccm for ditertiarybutyl-silane. Then, eight-period $In_{1-x}Ga_xN$/GaN MQW's were grown at 760 °C and 850 °C, respectively. Finally, a Mg-doped p-GaN layer was deposited on the top of the GaN quantum barrier layer at 1000 °C, using biscyclopentadienyl-magnesium as the doping source.

To fabricate a ReRAM/LED hybrid device, a 35-nm-thick polycrystalline NiO film was prepared by dc reactive sputtering method on a p-GaN/MQW/n-GaN/GaN/Al_2O_3 LED substrate at temperature of 500 ºC and pressure of 1.5 mTorr in Ar + O_2 mixture gas with O_2 ratio of 7 %.[17-21] Pt top electrodes with 100

μm × 100 μm were deposited and patterned using dc reactive sputtering and conventional lift-off process.

Schematic structures of a ReRAM/LED hybrid device are introduced in **Figure 4.7**(a). When the formation of CF, called set process, is induced by an applied electric field, initial resistance state is changed to low resistance state (LRS) in which carriers are injected to LED via CF and light emission is generated. In contrast, light emission in LED cannot be generated in high resistance state (HRS) when the CF is ruptured and carrier injection is limited. Figure 4.7(b) shows the typical unipolar resistive switching behaviors of a conventional Pt/NiO/Pt structure (red open symbols) and a Pt/NiO/LED hybrid device (black open symbols). Electrical properties were measured using a Keithly 2400 sourcemeter at room temperature and atmospheric pressure. The Pt/NiO/LED generally shows lower current levels and higher operation voltages in various resistive states including initial state, HRS, and LRS compared to those of the Pt/NiO/Pt, which may result from relatively higher resistance of the LED structure than that of the Pt bottom electrode. Simultaneously with these

conventional resistive switching behaviors, changes in device-scale blue light emission images are able to be detected as demonstrated in Figure 4.7(c). In case of the LRS, we can observe inhomogeneously distributed blue spots at which CF's formed in NiO are connected to the electrode of LED.

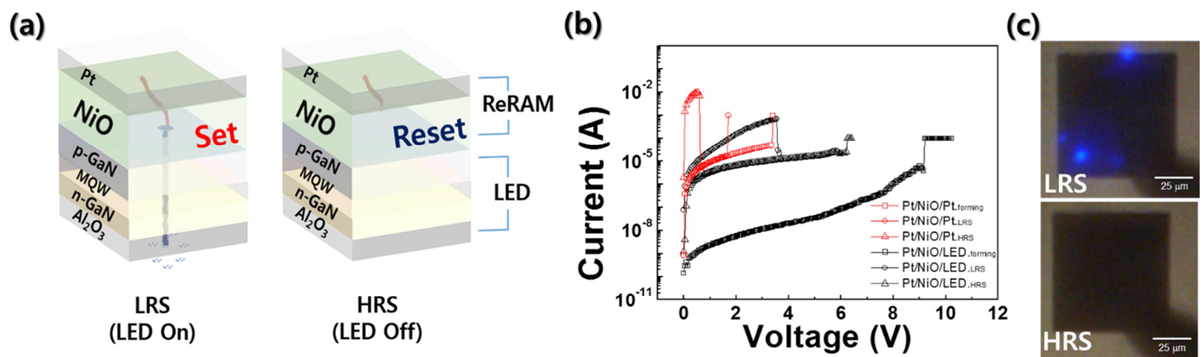

Figure 4.7. Transport and light emitting characteristics of a ReRAM/LED hybrid device. (a) Schematic device structures, (b) resistive switching behaviors, and (c) light emission images of a ReRAM/LED hybrid device in LRS and HRS. For comparison, resistive switching behaviors of a conventional ReRAM are also displayed in (b).

4.6.2. Real-time imaging of resistive switching dynamics

To figure out impact of NiO interlayer on operation of LED in our experimental system, electrode dependent LED performance is investigated. Ni electrode and Au protecting layers, each of which has ~ 10 nm thickness, are deposited on our LED device using thermal evaporator deposition, as shown in the upper inset of **Figure 4.8**(a). Semi-conducting NiO layer is fabricated between Ni and p-GaN by oxidation using rapid thermal annealing in oxygen flow. Bright light emission (lower inset of Figure 4.8(a)) by recombination of electrons and holes in junction between p-GaN and n-GaN supported by multi-quantum well is generated at applied voltage above 3 V where current level is rapidly increased in Figure 4.8(a). During applying voltage no resistive switching behavior occurs due to low resistance of semi-conducting NiO. However, the same LED structure with Pt top electrode (Figure 4.8(b)) shows neither light emission nor rapid increase of current level implying that the Pt electrode is not suitable for making ohmic contact with the p-GaN layer. According to these results, resistive switching NiO thin film inserted between Pt top electrode and LED structure is expected to make

an ohmic contact by formation of CF consisting of metallic Ni-based materials leading to light emission from LED structure.

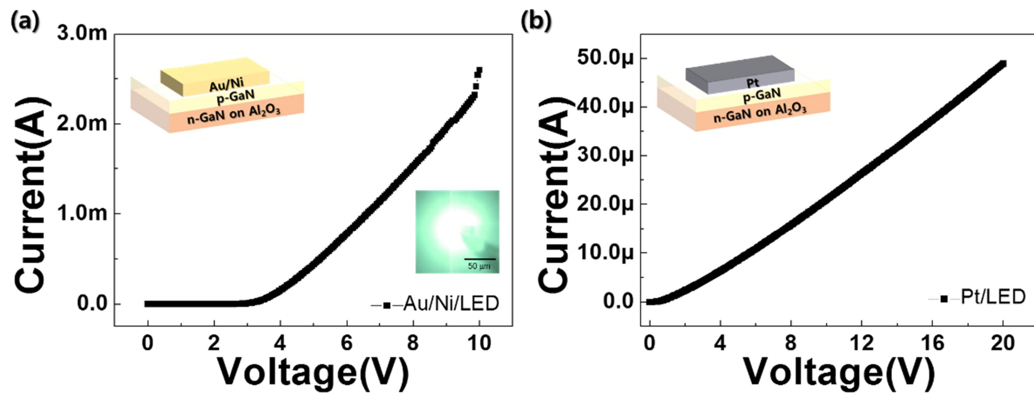

Figure 4.8. Electrode dependent LED performance. Current-voltage curves of LED devices with (a) Au/Ni and (b) Pt top electrode. The upper insets show schematic diagrams of LED devices and the lower inset of (a) reveals the light emission image obtained from the Au/Ni/LED device.

To obtain a stable forming, setting of appropriate compliance current is required as a tool for limiting damage on the device when CF's are suddenly connected to p-GaN by high applied voltage. Under compliance current of 10 μA, we can observe semi-forming with gradual increase of current level indicating formation of CF's which do not make a perfect connection between top and bottom electrodes, as shown in **Figure 4.9**(a). The optical microscope images of the Pt/NiO/LED in Figure 4.9(b) were obtained when its current-voltage (I-V) curves in Figure 4.9(a) reached the points marked by arrows and numbers. At the point 1 (8.85 V, 0.17 μA), light spot A and B (L-A and L-B) are detected. As the applied voltage is increased, light spot C (L-C), D (L-D), and E (L-E) gradually appear at the point 2 (9.05 V, 0.27 μA) and 3 (9.85 V, 1.42 μA). L-A and L-E disappear when the current level is about to reach compliance current of 10 μA, which may be caused by thermal damage to parts of CF's. The compliance current is increased to 100 μA, which is 10 times higher than that of semi-forming, to induce full forming process. The CF's are already partially formed during semi-forming process and thus current level is generally elevated. The L-B, L-C, and L-

D appear when I-V curve reaches the point 5 (6.50 V, 4.12 μA) whose voltage is relatively lower than those of points 1-3 during semi-forming process. Finally forming process is completed at the point 6 (8.20 V marked as $V_{forming}$, 18.94 μA) with appearance of additional light spot F (L-F), which is considered as a main CF for resistive switching. Because applying voltage is automatically limited when the device is switched at $V_{forming}$, light intensity of the L-F is not strong compared to other light spots. It is also assumed that forming process may induce the formation of incomplete CF's whose endpoints are not close enough to p-GaN to transfer charge carriers and generate light emission in the LED part.

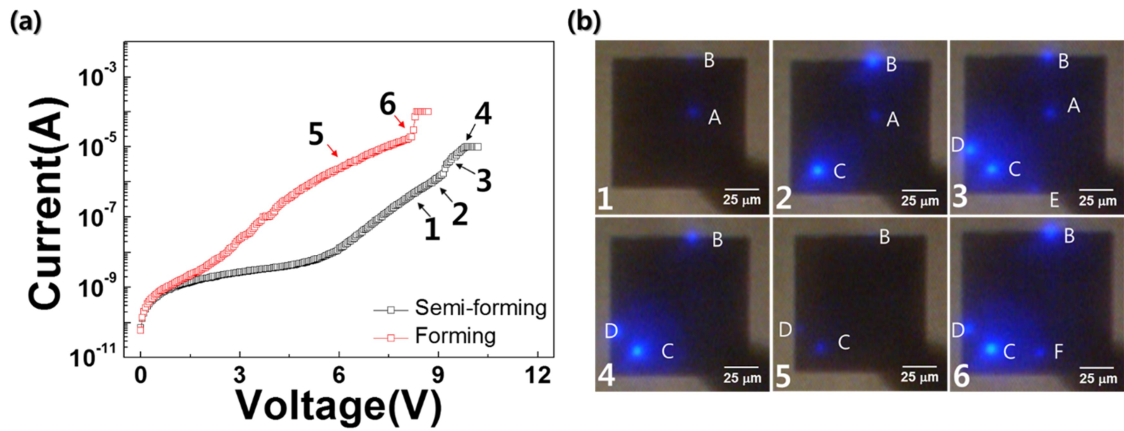

Figure 4.9. Resistive switching and real-time light emission during semi-forming and forming processes. (a) Resistive switching behaviors and (b) light emission images of a ReRAM/LED hybrid device during semi-forming and forming processes. Black and red open squares in (a) indicate semi-forming and forming processes, respectively. Light emission images in (b) are obtained when I-V curves in (a) reach the points marked with arrows and numbers during resistive switching.

During repetitive operation in our ReRAM/LED device, different resistive switching behaviors are observed as shown in **Figures 4.10**(a), 4.10(c), and 4.10(e). At LRS obtained after forming process, only L-F is observed in stable reset and stable set process (SrSs) as illustrated in Figure 4.10(b). In contrast with L-F, other CF's are not detected due to the low applied voltage of point 1-SrSs (2.15 V, 9.2 mA) although its current level is higher than forming process. At point 2-SrSs just after switched from LRS to HRS, we can observe turn-off of L-F simultaneously with step-like current drop implying rupture of the CF. This result can be explained by former studies about random circuit breaker (RCB) model which showed that only one metal cluster was completely connected from bottom electrode to top electrode but others were not connected although they were formed even near the top electrode.[94] Therefore, light emissions at L-A to L-E seem to be detected by tunneling current through very thin insulating gap between insufficiently formed CF's and p-GaN under high applied voltage. Subsequently, we can observe gradual current increase as applied voltage increases up to set volate (V_{set}) because ruptured CF is able to grow close to the top electrode. 3-SrSs

(3.75 V, 28.54 μA) and 4-SrSs (4.75 V, 65.39 μA) are referred to as gradual growth and complete connection (set switching) of CF, respectively. In this process, only L-F is observed in Figure 4.10(b) demonstrating that resistive switching is managed by L-F.

In stable reset and unstable set process (SrUs), I-V curve and light emission images of the stable reset process in Figures 4.10(c) and 4.10(d) are similar to those of SrSs. During successive unstable set process, gradually increased current is suddenly dropped at 5-SrUs (5.90 V, 47.52 μA) while it shows step-like increase at 6-SrUs (6.15 V marked as V_{set}, 34.58 μA) indicating that CF is reconnected to the top electrode. In contrast to SrSs, minor L-C and L-D are also observed after resistance fluctuation of SrUs but major L-F is still brightest.

In case of unstable reset and stable set process (UrSs), current fluctuation in LRS is observed with blinking of L-F as illustrated in Figure 4.10(f). 1-UrSs (3.05 V, 486.00 μA) and 2-UrSs (3.50 V, 298.89 μA) in Figure 4.10(e) are located at voltages lower than those of unstable HRS introduced in Figure 4.10(c). Therefore, we can assume that L-C and L-D from minor CF's are not observable

in Figure 4.10(f) due to insufficient applied voltage for considerable tunneling current. Stable set process occurs at V_{set} very close to V_{reset} of unstable reset although large gap between V_{set} and V_{reset} is required for preventing readout failure caused by switching voltage overlap.

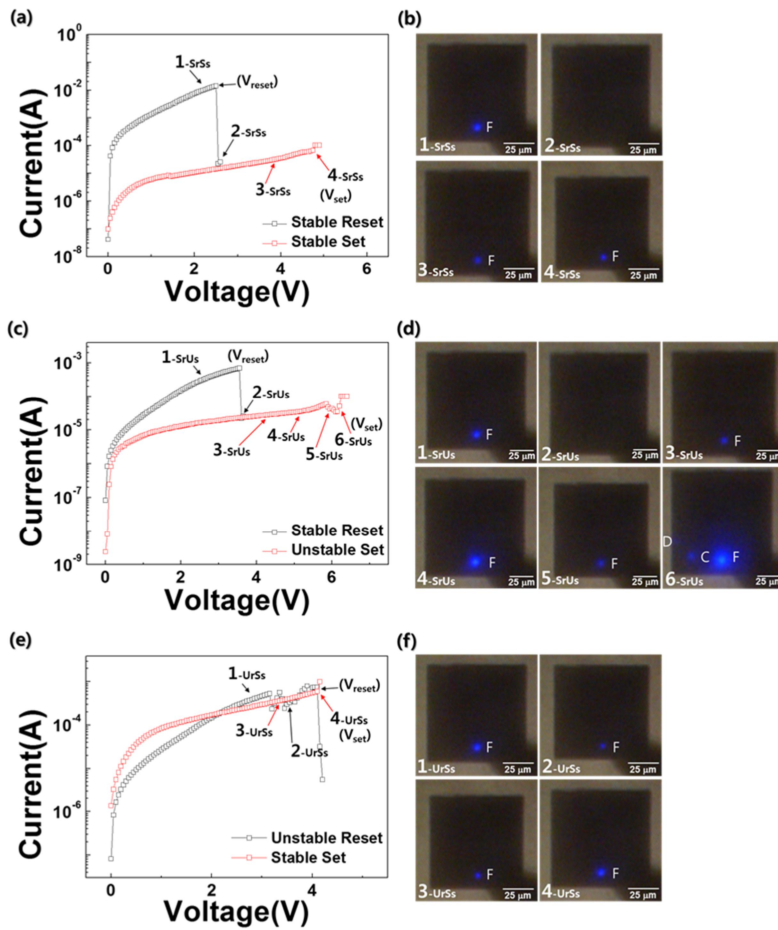

Figure 4.10. Repetitive resistive switching and real-time light emission. (a, c, e) I-V curves and (b, d, e) light emission images of a ReRAM/LED hybrid device during (a and b) stable reset and stable set (SrSs), (c and d) stable reset and unstable set (SrUs), and (e and f) unstable reset and stable set (UrSs) processes. Light emission images are obtained when I-V curves reach the points marked with arrows and numbers during resistive switching.

More unstable reset process (MUr) induces more frequent blinking of L-F indicating fluctuation in CF configuration, as shown in **Figures 4.11**(a) and 4.11(b). Especially after the disappearance of L-F which is caused by the lowest current level at 4-MUr (4.22 V, 512.42 μA), L-F is turned on again which means that major CF is not ruptured perfectly and soft reset process occurs probably due to lack of joule heating. When applied voltage is increased from 0 V after the more unstable reset process, L-B, L-C, and L-D from minor CF's appear in voltage region even lower than V_{set} as shown in Figure 4.11(d). It seems that current fluctuation during more unstable reset switching, detected also using change in the light emission image, is accompanied by growth of minor CF's. Such current fluctuation depresses the life time of a ReRAM device because it is able to cause damages on the device. Although many previous studies have reported decrease in current fluctuation using deposition process control, oxide barrier, and simply modified circuit design,[97] they didn't demonstrate the correlation between current fluctuation and change in CF configuration. In constrast, our results reveal that the current fluctuation is simultaneously observed

with blinking of L-F (unstable behavior of main CF) and appearance of L-B, L-C, and L-D (growth of minor CF's).

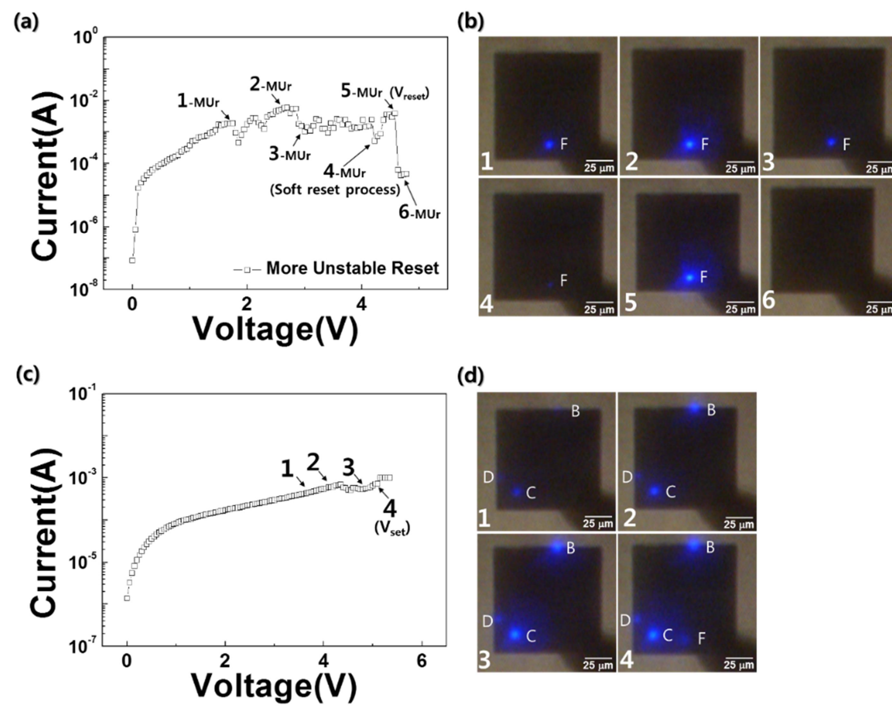

Figure 4.11. More unstable reset switching and real-time light emission. (a and c) I-V curves and (b and d) light emission images of a ReRAM/LED hybrid device during (a and b) more unstable reset and (c and d) subsequent set processes.

Figure 4.12(a) shows relation between set current (I_{set}) and V_{set} where resistive switching from HRS to LRS occurs at other ReRAM/LED hybrid device. At $V_{forming}$ of 10V, which is the highest switching voltage, many light spots including L-E at major CF appear as shown in Figure 4.12(b). After forming process, first set operation takes place at lower voltage and current level than those of forming. However, when 10th set switching is induced, current level is increased by about two orders showing degradation of resistive switching properties especially on/off ratio. When 31st set switching occurs after repetitive switching, variation of major CF from L-E to L-A is detected as illustrated in Figures 4.12(c) and 4.12(d) with decrease of the current level and increase of operation voltage to similar value of forming operation. Resistance increase of 31st set switching is attributed to deterioration of major CF under L-E and connection of alternative minor CF under L-A at higher voltage. After connection of the CF under L-A, the CF under L-E is connected again at 35th set switching where low switching voltage is recovered as shown in Figure 4.12(e). This observation implies that large voltage fluctuation after degradation of resistive

switching is managed by replacement of stressed major CF with fresh minor CF.

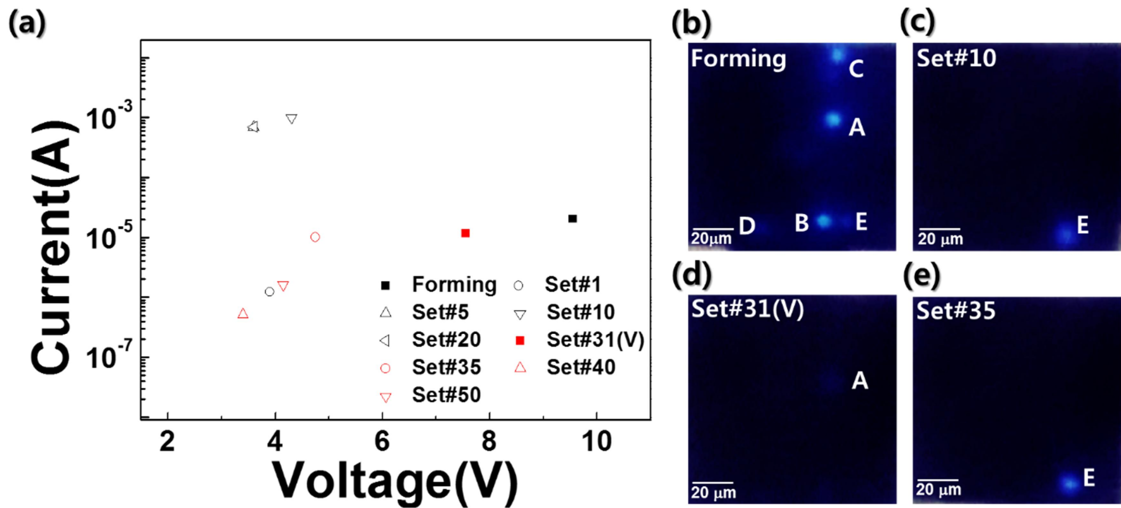

Figure 4.12. 50 times resistive switchings and real-time light emission. (a) I_{set} versus V_{set} relationship and (b-e) light emission images obtained at several set switchings during 50 times resistive switchings of other ReRAM/LED hybrid device.

4.7. Summary

In summary, we fabricate flexible inorganic non-volatile memory array composed of oxide/nitride/graphene hybrid structures. We demonstrate stable resistive switching characteristics including cumulative probability, endurance, and retention analysis even in bent and rolled states. After 1000 times of bending, we obtain that resistive switching characteristics are not degraded. Furthermore, even at 450K, our hybrid device shows stable resistive switching characteristics without overlap between HRS and LRS. We believe that our hybrid structures may foster inorganic based flexible memory applications with good durability on harsh conditions including many times of banding and device operation in high temperature.

Furthermore, using NiO/GaN hybrid material structures, we propose a new hybrid structure composed of ReRAM and LED which enables us to monitor the time evolution of CF configuration on the device scale during resistive switching. We directly observe unstable formation/rupture process of CF and anomalous conducting filament connection, which accompany switching parameter

fluctuation considered as critical weaknesses of the ReRAM. In contrast to former real-time measurement studies using in-situ TEM or C-AFM, we can investigate the change in CF configuration in whole area of the device during more than 50 times of resistive switching in atmospheric condition. Our ReRAM/LED hybrid structure demonstrates that unstable formation/rupture process of CF during resistive swiching gives rise to either change in major CF or growth of minor CF's which potentially cause variation on CF configuration and thus large fluctuation in switching parameters.

Monolithic integration of morphology controlled GaN microstructures on graphene films for flexible & multi-color LEDs

5

5.1. Introduction

Highly efficient and flexible multi-color micro light emitting diodes (micro LEDs) are required for mobile and wearable optoelectronic devices and displays with high resolution and low power consumption[1, 98]. For such applications, organic materials have long been studied, but higher performance of the device is expected by using inorganic materials due to their excellent electrical and optical characteristics as well as long-term stability and reliability[41, 99]. Recent studies on GaN based micro- and nanostructures on CVD-graphene films demonstrated feasibility for their application on flexible light emitting devices[11, 100]. However, their full color display application has still remained out of reach

because of difficulty in achieving multiple color generation from inorganic LEDs on the same substrate. Meanwhile, fabrications of multi-color LEDs have recently been realized on sapphire substrate by simultaneous growth of various GaN microstructures and subsequent formation of multiple quantum wells (MQWs) on the different facets[62, 101]. In such devices, the emission colors originate from various indium (In) composition and/or width variation of MQWs on the different facets of the microstructures[62]. Nevertheless, difficulty in monolithic integration of various GaN microstructures on CVD graphene films represent one of the major obstacles to using inorganic semiconductors in flexible full color light emitting devices. Accordingly, one critical step for the flexible and full light emitting devices is to prepare monolithic integrated various GaN microstructures on CVD graphene films. Here, we report on the fabrication of flexible and monolithically integrated multi-color micro LEDs using GaN microrods and micropyramids simultaneously grown on CVD graphene films.

5.2. Morphology control of GaN microstructures on graphene films

Morphology controlled growth of GaN microstructures describes in this section. The key parameter that originates growth of different microstructures under same growth conditions including temperatures and growth times is growth rate controllability. To simultaneously grow various microstructures on a single substrate, we varied the spacing of the ZnO nanotubes where the heteroepitaxy of GaN and ZnO performs.

5.2.1. Growth parameter: spacing & time

The simultaneous growth of different microstructures on graphene films were achieved by selective area metal-organic vapor-phase epitaxy (SA-MOVPE). For the substrate preparation, graphene thin films synthesized on Cu foil were transferred onto SiO_2/Si substrates, essential for growing high quality GaN microstructures, offering easy transfer of the microstructures to an arbitrary substrate, and fabricating flexible devices. For the SA-MOVPE of inorganic materials on the CVD graphene films, a 300-nm-thick SiO_2 layer was deposited

on the CVD-graphene films and patterned by conventional lithography technique. Next, hole patterns on the growth mask were defined by e-beam lithography. we prepared hole arrays for growth of ZnO nanostructures with different spacings of 2, 4, 6 and 8 μm and a diameter of 0.6 μm, respectively. After lithography, the SiO_2 film was etched by reactive-ion etching (RIE) using CF_4 plasma and buffered oxide etchant(BOE). Then, ZnO nanotube arrays were selectively grown on SiO_2-mask-patterned CVD-graphene films by catalyst-free MOVPE as shown in **Figure 5.1**.

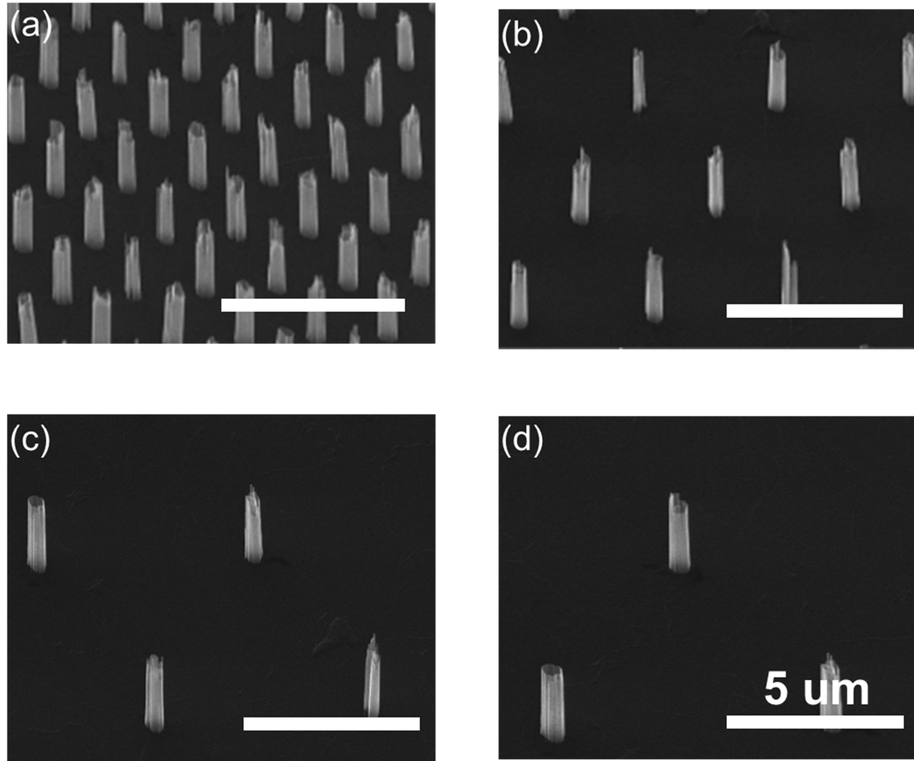

Figure 5.1. SEM images of ZnO nanostructures with different spacings. (a) 2, (b) 4, (c) 6, and (d) 8 μm.

Growth time and spacing dependent morphology changes of GaN microstructure were investigated by SEM as shown in **Figure5.2**. For 2 μm spacing, a rough surface morphology with a few hundred nanometer-thick irregular GaN layers was observed for microstructures when the growth time is 2 min. Meanwhile, as the growth time increases to 4 and 10 min, GaN microstructures exhibited a flat and smooth surface showing a microrod shape with its diameter and height of 1.1 and 4.2 μm. We further explored the morphology change by increasing the growth time from 10 to 20 min and obtained a micropyramid shape with significant increase of the diameter from 1.1 to 2.0 μm but their height did not change significantly. Similar morphology change behavior was observed for the larger spacings; a microrod changes to a micropyramid as the growth time increases.

Interestingly, for the fixed growth time, GaN microstructures become thicker similarly to the growth time dependent morphology change behavior as the spacing increases. The layers grown on 2 μm spacing exhibited a little rough and irregular surface morphology but the GaN layers grown on larger spacings did

show clear facets with a smooth surface. Furthermore, as the spacing increases from 2 to 6 and 8 μm, the microstructure exhibited larger diameters changed from 1.1 to 1.8 μm indicating that thicker GaN layer was grown as the spacing increases. Meanwhile, for the given spacings, the height of GaN microstructure did not change significantly. Similar behavior was observed for the microstructures at different growth times of 4, 10, 16, and 20 min.

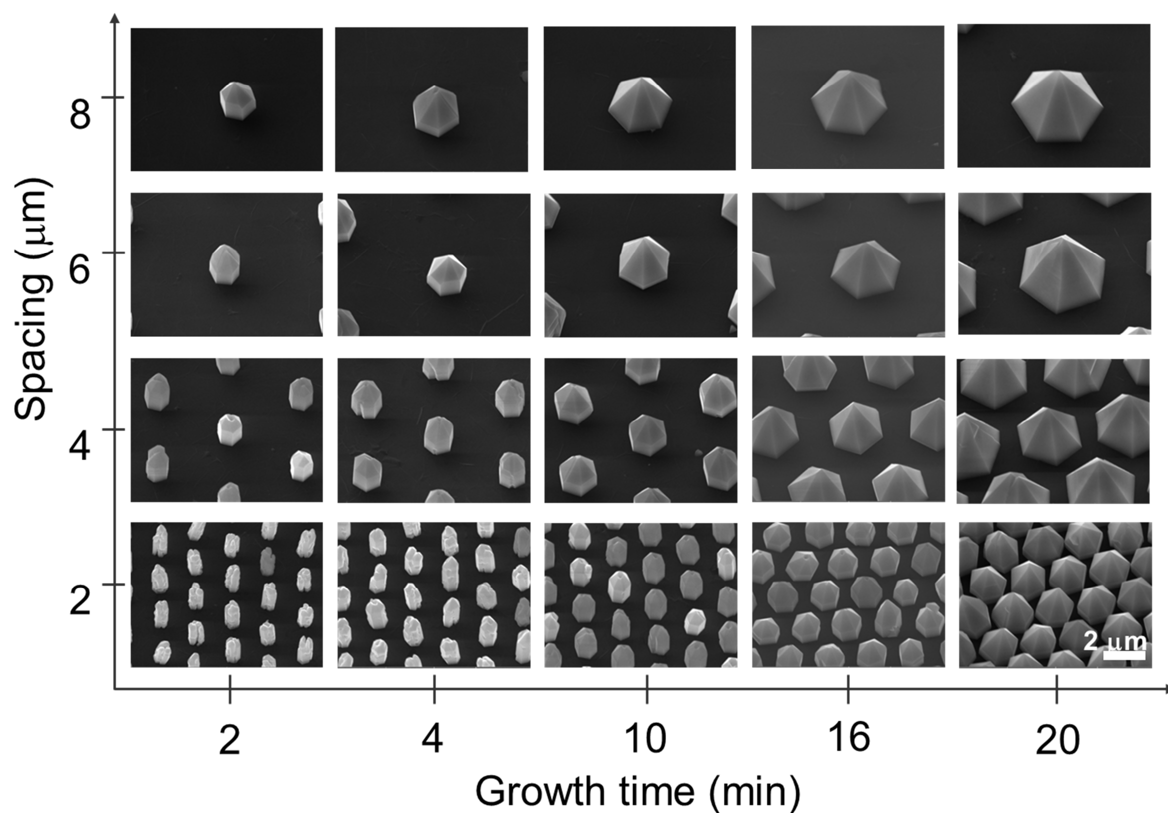

Figure 5.2. Morphology controlled growth of GaN/ZnO heterostructures. SEM images of the GaN/ZnO heterostructures with different spacings and growth times show gradual change of their morphology from microrod to micropyramid.

5.2.2. Growth behavior analysis

The SEM images show strong growth time and spacing dependence of the morphology change indicating clear morphology change from a microrod to a micropyramid as the growth time and spacing increase. Interestingly, lateral growth occurs on the semi-polar planes rather than non-polar planes, resulting presumably from the difficulties in achieving growth on the non-polar facet.[102] Since the density of dangling bond (DB) of the non-polar facet (12.1 nm^{-2}) is smaller than that of the semi-polar facet (16.0 nm^{-2}), the growth along the semi-polar facet would be energetically more favorable, thus resulting in forming micropyramids.

We further studied the growth temperature dependent morphology change of GaN microstructures to investigate Ga adatom migrations and adsorption/desorption. We examined various growth temperatures in the range of 900 – 1100 ˚C with a fixed ZnO nanostructures spacing of 4 μm and a length of 3.8 μm (**Figure 5.3**). As the growth temperature increases, it is clearly shown that the morphology changes from a microrod to a micropyramid with enhanced

growth selectivity. Meanwhile, when the growth temperature is 1100 ˚C, randomly grown GaN particles are observed which presumably resulted from destruction of the ZnO nanostructure due to high desorption rate of Ga atom resulting in exposure of the ZnO nanostructure to H_2 atmosphere at high temperature where ZnO can be dissolved[14]. This result indicates that migrations and adsorption/desorption of the Ga adatoms are critical factors of the morphology-controlled growth.

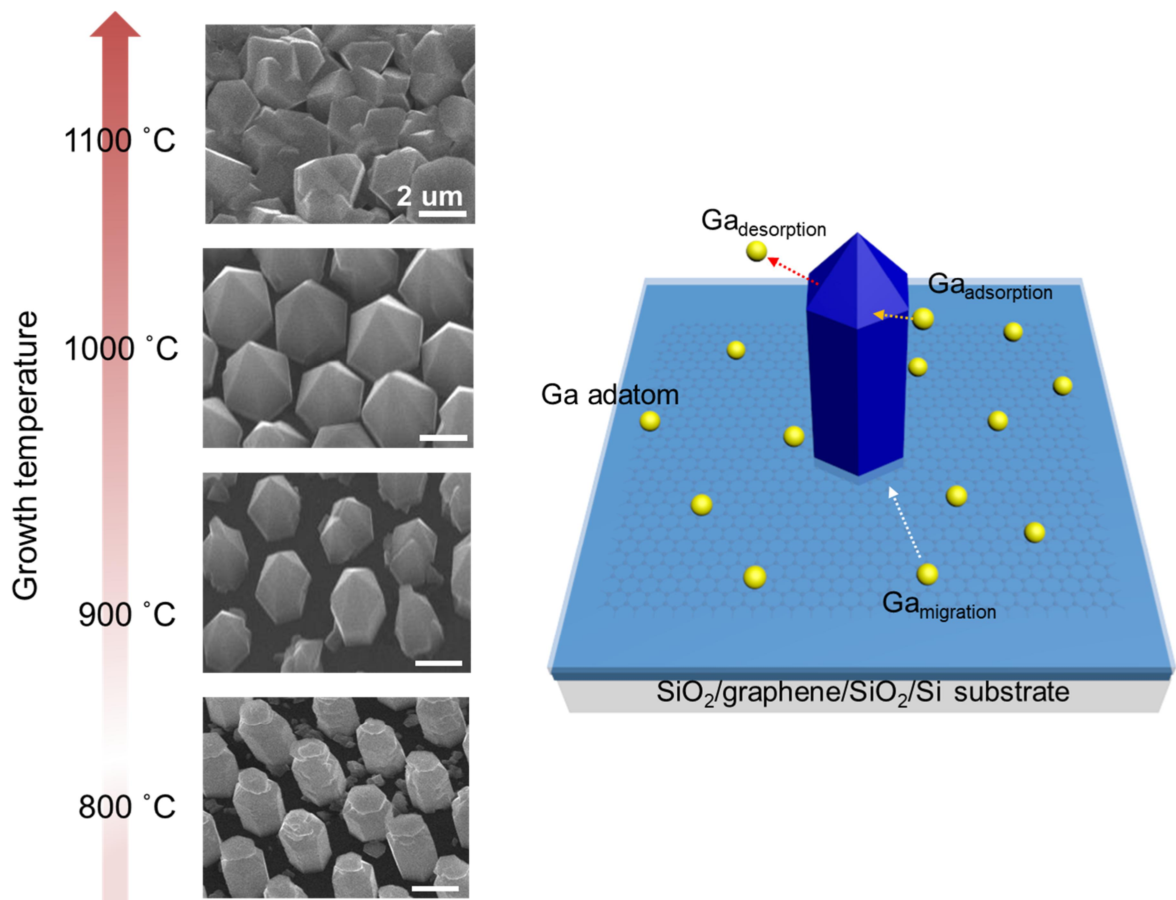

Figure 5.3. GaN/ZnO heterostructures grown at different temperatures and schematic illustration of their growth mechanism.

Based on the observations of the morphology change of GaN microstructure, we suggest that the morphology change of GaN microstructure can be qualitatively explained by the growth rate control model presented in **Figure 5.4**. When a surface diffusion length of the Ga atom is ℓ, the area that Ga atom can diffuse would be $\ell^2\pi$. In this area, if the ZnO nanostructure arrays are prepared with a certain number of nanostructures (n) and their spacing is smaller than ℓ, the amount of Ga atoms that can be grown on a single nanostructure would follow $\sim\ell^2\pi/n$. At the growth temperature of 1000 ˚C, ℓ is estimated to be 10 μm[103] so the growth rate could be affected by spacings of the ZnO nanostructures when the spacing is narrower than 10 μm.

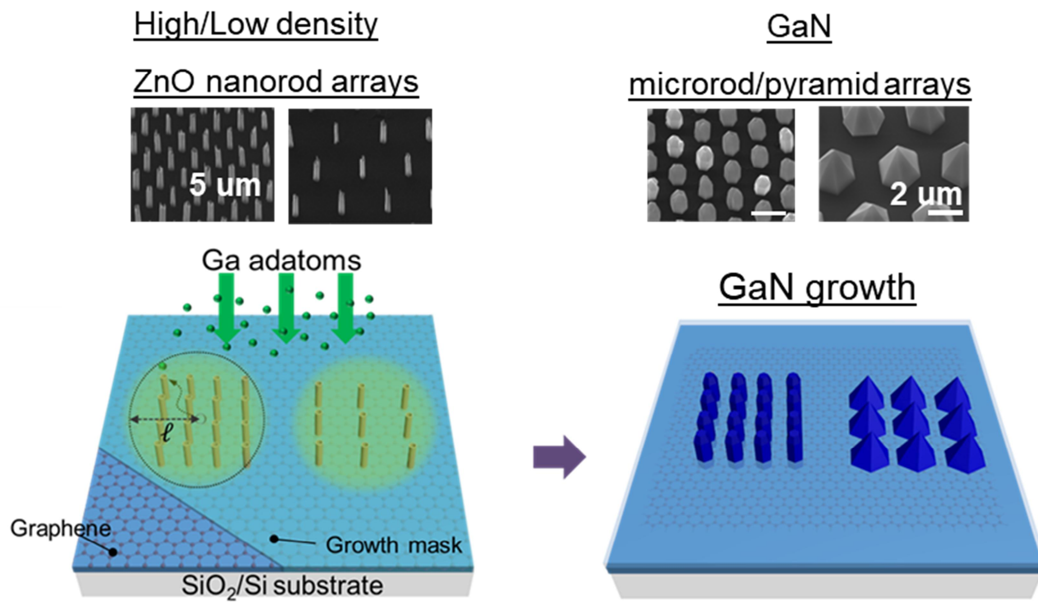

Figure 5.4. Strategy for the monolithic integration of GaN microrod and micropyramid on CVD graphene films.

Meanwhile, when the spacing is wider than 10 μm, micropyramid was grown with poor growth selectivity as shown in **Figure 5.5**. The poor selectivity resulted from formation of GaN islands between the ZnO nanostructures, presumably due to the shorter diffusion length than the spacing.

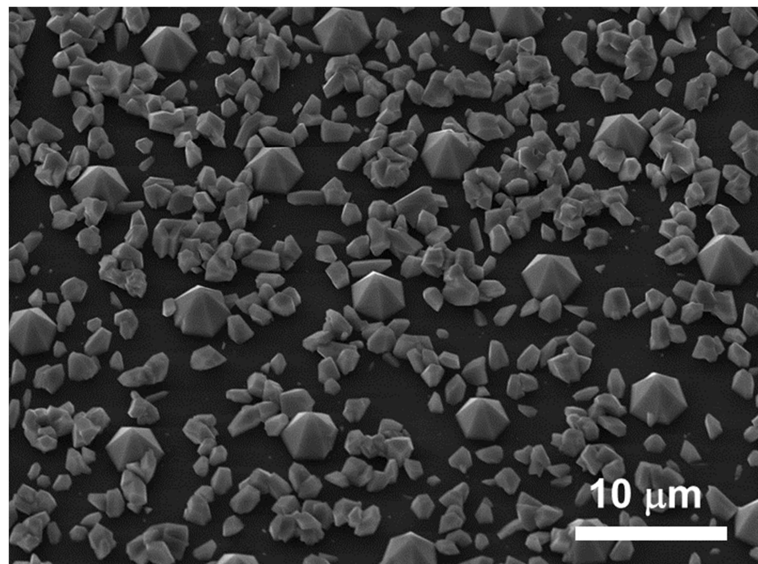

Figure 5.5. SEM image of GaN microstructures grown on ZnO nanostructures with spacing of 12 μm.

5.3. Fabrication of LEDs on graphene films

The morphology controlled growth of GaN microstructures, composed of GaN *p-n* homojunction with InGaN/GaN QW on large graphene films enabled the fabrication of monolithically integrated flexible LEDs. The basic approach for the fabrication is shown in **Figure 5.6**(a). To integrate GaN microrod and micropyramid on graphene films simultaneously, we grow GaN on ZnO nanostructures with different spacings of 2 and 6 μm for 10 min. After growing LED structures on graphene films, *p*-GaN metal contacts with an area of 50 × 50 μm^2 were formed on the top region of as-grown LEDs by sequential steps of *p*-GaN activation, polyimide (PI) layer filling, and Ni/Au layer depositions. To impart mechanical flexibility to the devices, the LEDs were removed from the SiO_2/Si substrate by chemical etching of the SiO_2 layer using buffered oxide etchant (BOE). Then, the LEDs were adhered to the Cu-coated PET substrate to make an electrical connection between the CVD graphene films of the device and an insulating plastic substrate.

Monolithically integrated multi-color LEDs can emit various colors by applying the voltages on different multi-color LEDs simultaneously. Figure 5.6(b) displays an optical microscope image showing the blue and green color emissions by applying 9.0 V on microrod- and micropyramid-based LEDs, respectively.

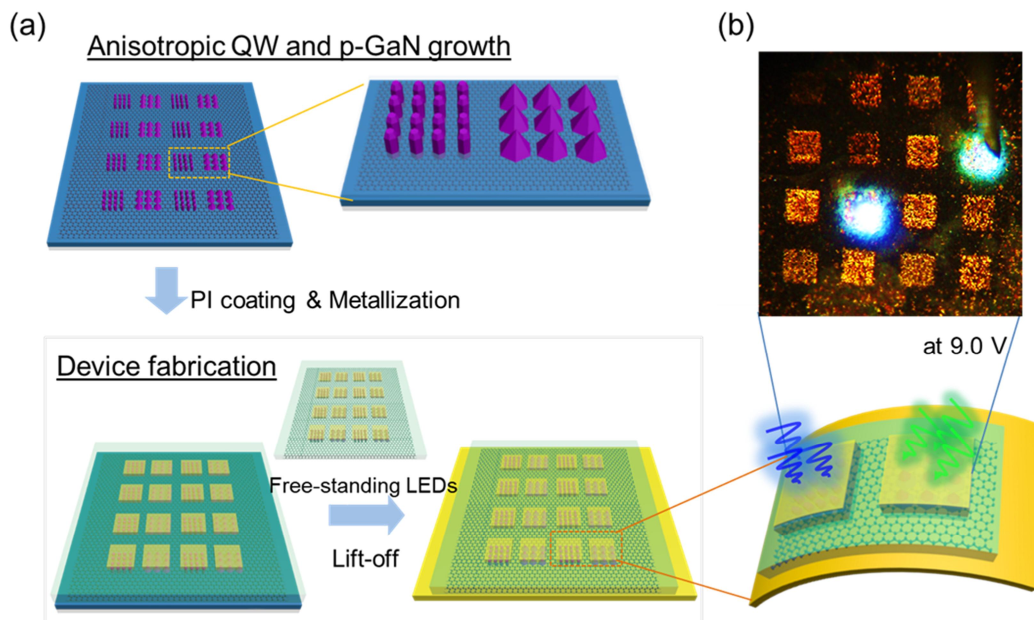

Figure 5.6. Schematic illustration of monolithic integrated flexible LED. (a) device fabrication and (b) its demonstration at 9.0 V.

5.4. EL and electrical characteristics

We further investigated the optical characteristics of microrod- and micropyramid-based LEDs as shown in **Figure 5.7**. Figure 5.7(a) displays the EL spectra of the microrod-based LED at various current levels in the visible range. Under a current of 0.11 mA, the dominant EL emission from the microrod-based LED was at 506.3 nm with another shoulder peak centered at 536.9 nm. As the current increased to 0.25 and 0.50 mA, the main EL peak changed to 505.3 and 504.8 nm. Meanwhile, the dominant EL peak of the micropyramid-based LED gradually shifted from 580.3 to 570.2 nm by changing the applied currents from 0.11 to 0.50 mA with another shoulder peak centered at 509.9 nm as shown in Figure 5.7(b).

The optical characteristics of the GaN microstructure LEDs can be analyzed by comparing them with previously reported result. Y. Robin *et al*. reported simultaneous growth of GaN microrod, micropyramid, and microdisk by controlling the diameter of the growth mask opening and fabricated different LEDs by subsequent deposition of InGaN/GaN QWs on those structures.[62] Their

observation of photoluminescence (PL) and cathodo-luminescence (CL) shows the similar tendency to our data demonstrating wavelength shift from blue to green and red as the structure changes from microrod to micropyramid and microdisk. In addition, Hong *et al*. reported the appearance of additional blue emission peak from microrod-based LED at high applied bias voltages with qualitative explanation using the field distribution model.[104] Based on their investigation, EL spectra in Figure 5.7(a) can be interpreted that the QW formed on non-polar plane which dominantly consists the microrod structure emits blue color at a high current (marked as a blue dot), while a shoulder peak at a longer wavelength is observed from the QW formed on semi-polar plane (marked as a green dot). In contrast, the micropyramid-based LED that the semi-polar plane is dominant emits main EL peak at a longer wavelength region whereas a small shoulder peak appeared at a shorter wavelength region. In addition, it is also reported that the spectral broadening and EL peak shift from micropyramid-based LEDs consisting of semi-polar plane can be related to the nonuniform QW

thickness[105]. This result strongly suggests that EL spectra in Figure 5.7.(b) seems to be originated by nonuniform QW thickness shown in **Figure 5.8**.

The LED structures were grown by deposition of $In_xGa_{1-x}N$/GaN quantum well (QW) and *p*-GaN layers on the microstructures. Figure 5.8 shows TEM images of microrod- and micropyramid-based LEDs fabricated on graphene films. The TEM images clearly show differences in the QW thickness and composition between the microrod- and micropyramid-based LEDs. The formation of QW with different thicknesses and compositions that depend on the GaN microstructure planes may have resulted from the anisotropic surface formation energies of GaN crystal planes that influence the diffusion of adatoms[104].

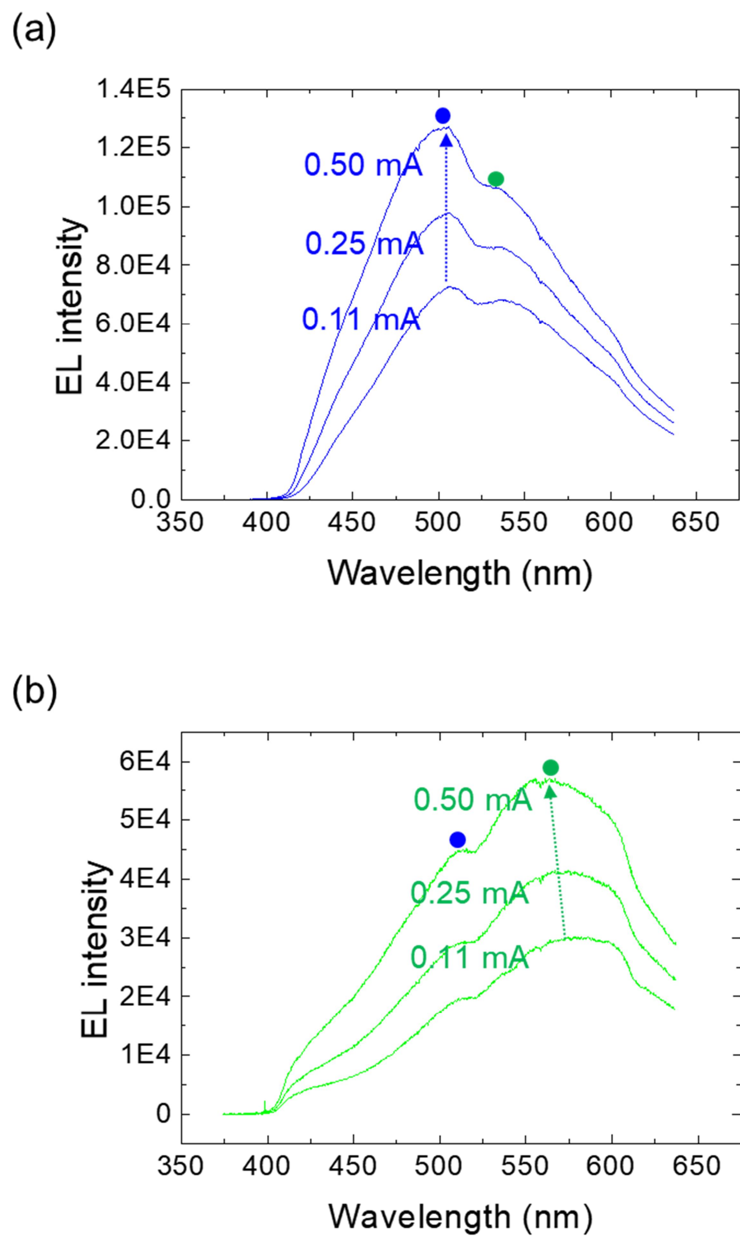

Figure 5.7. EL spectra of (a) microrod-based and (b) micropyramid-based LEDs as a function of current levels from 0.11 to 0.50 mA.

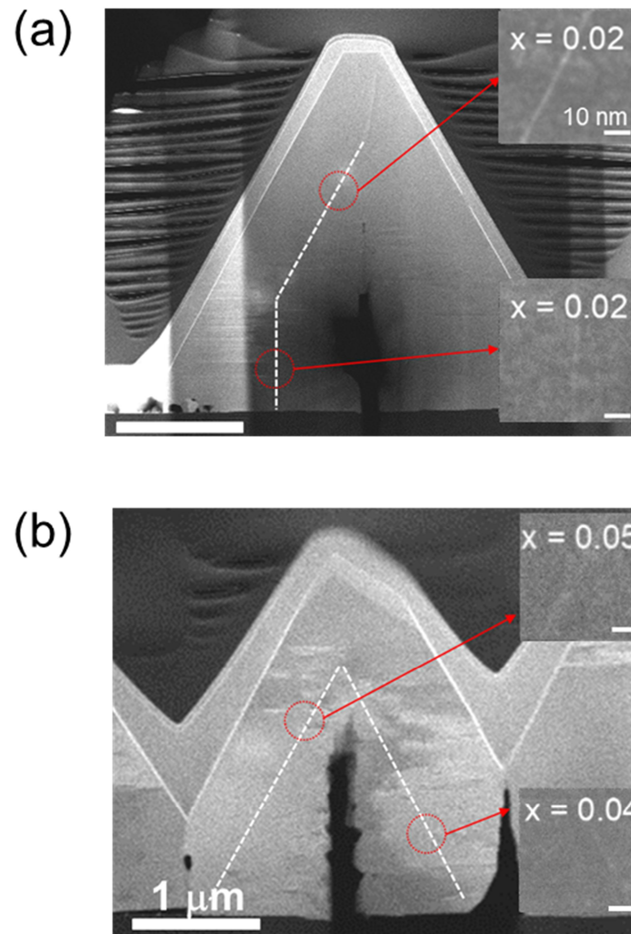

Figure 5.8. TEM images of monolithically integrated LEDs on CVD graphene films. (a) microrod-based LED. (b) micropyramid-based LED.

The device characteristics of the microrod- and micropyramid-based LEDs transferred onto Cu foil were evaluated under substrate bending. Figu re **5.9**(a) shows the light emission photographs of microrod-based LED at b ending radii of ∞, 7, 5, and 3.5 mm showing reliably produced blue light emission under a fixed applied bias voltages of 9.0 V. Figure 5.9(b) and 5. 9(c) show the current (*I*)−voltage (*V*) characteristic curves of microrod- and micropyramid-based LEDs under 1000 times of the bending showing typical rectifying behavior characteristic of GaN *p*−*n* junction diodes. However, the current level of the micropyramid-based LED slightly increases as bending cycles increase in contrast to the microrod-based LEDs showing negligible changes in the current level. Figure 5.9(d) shows plot of the normalized E L intensities of the microrod- (top) and micropyramid-based LEDs (bottom) as a function of bending cycles at a applied current of 0.25 mA, respective ly. It is obtained that normalized EL intensities slightly decreased when be nding cycles reached to 1000 times of repeated bending.

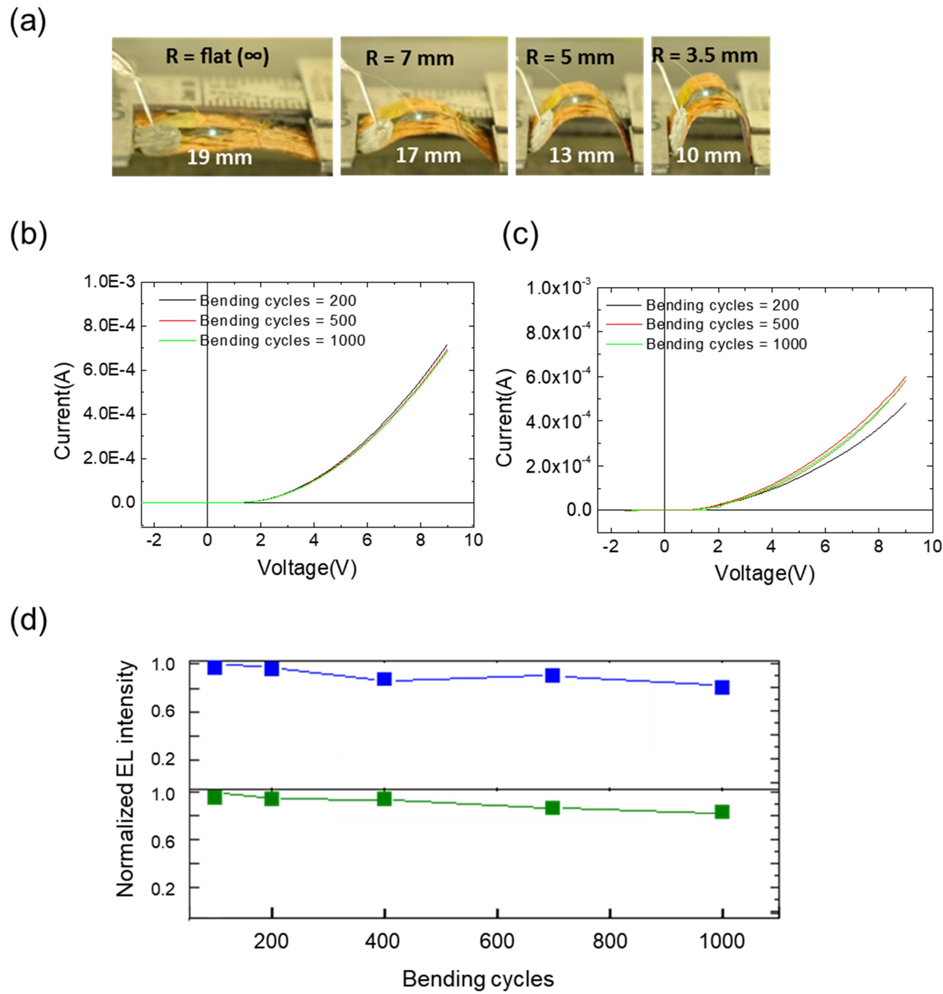

Figure 5.9. Flexibility demonstrations. (a) Light emission photographs at bending radii of ∞, 7, 5, 3.5 mm. I–V characteristic curves as a function of the bending cycle for (b) microrod-based and (c) micropyramid-based LEDs. (d) Normalized EL intensity of the microrod-based (top) and micropyramid-based LEDs during 1000 times of bending.

5.5. High temperature operations of flexible LEDs

Head-up displays (HUDs) are displays that present data without requiring users to look away from their usual viewpoints. The HUDs composed of a concave mirror with a display that producing images where the light is collimated are now applied in commercial aircraft or automobiles. However, low efficiency of the projection for producing images limits displaying the images under sun light. To address this, large-scale and flexible optoelectronic devices have attracted attention since they can directly be attached on windshield glass. Meanwhile, light source for the HUD is expected to retain its light emission characteristics under harsh condition because it may have wide operational environment such as high temperature and humidity. Recently, organic films have widely been employed due to their excellent scalability and flexibility for the large-scale and flexible optoelectronic devices.[106, 107] However, performance of the device composed of organic materials can be limited under such harsh condition because organic materials are sensitive to its operational environment. Compared with organic materials, an inorganic semiconductor can offer better

optical characteristics because it is mechanically, chemically, and thermally stable.[4] Regarding this issue, flexible LEDs based on GaN microstructures grown on CVD-graphene films are appropriate candidate to satisfy those requirements. We report the light-emitting characteristics of GaN microdisk light-emitting diodes (LEDs) grown on CVD-graphene dots at high temperatures ranging from 20 to 100°C. Most of these temperatures may exceed the operational temperature of flexible displays. The characteristics were compared with those of conventional GaN thin-film LEDs on sapphire.

We investigated current (I) – voltage (V) characteristic curves of the GaN disks on CVD graphene films as function of temperature ranging from 293 to 373 K (**Figure 5.10**). The sample was prepared on hot plate and the temperature increases by 10 K with dwelling time of 10 minutes. They exhibited typical rectifying behavior characteristics of GaN p-n junction diodes. The leakage current and the turn-on voltage of the LEDs at 293 K were 0.3 mA at -3 and 3 V with current of 1.0 mA, respectively. As the temperature increases to 373 K, both leakage current and current at turn-on voltage increase to 0.6 and 2.5 mA.

Specifically, the current at forward bias drastically increases as the temperature increases to 313 K but it seems to be shown that the current does not change significantly when the temperature is higher than 313 K.

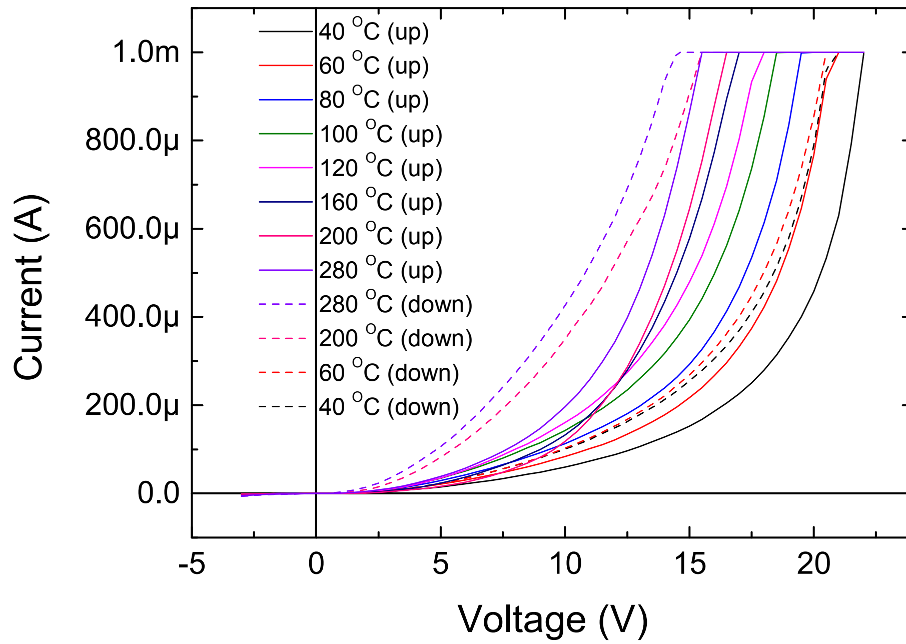

Figure 5.10. Temperature dependent $I - V$ characteristic curves of GaN microdisk LEDs. The temperature increased from 293 to 373 K by 10 K.

In order to evaluate temperature dependent light emission behavior of the GaN disk LEDs, we compare the electroluminescence (EL) spectra under temperature in the range of 293 to 373 K of the GaN disk LEDs on CVD graphene films with conventional GaN thin films on sapphire substrate at a fixed injection current of 10 mA as shown in **Figure 5.11**. At 293 K, the dominant EL emission was observed at 430 nm with another peak centered at 495 nm for the GaN disk LEDs. The EL characteristics of the GaN disk LEDs was quite distinct from that of the GaN thin films which exhibited only a dominant peak at 415 nm. The EL peak at 495 nm presumably originate from inhomogeneties in indium composition or thickness of the quantum wells along the GaN disk. As the temperature increases, the light intensity drops gradually in both LEDs with slight red shift behaviors which will be discussed in **Figure 5.12**.

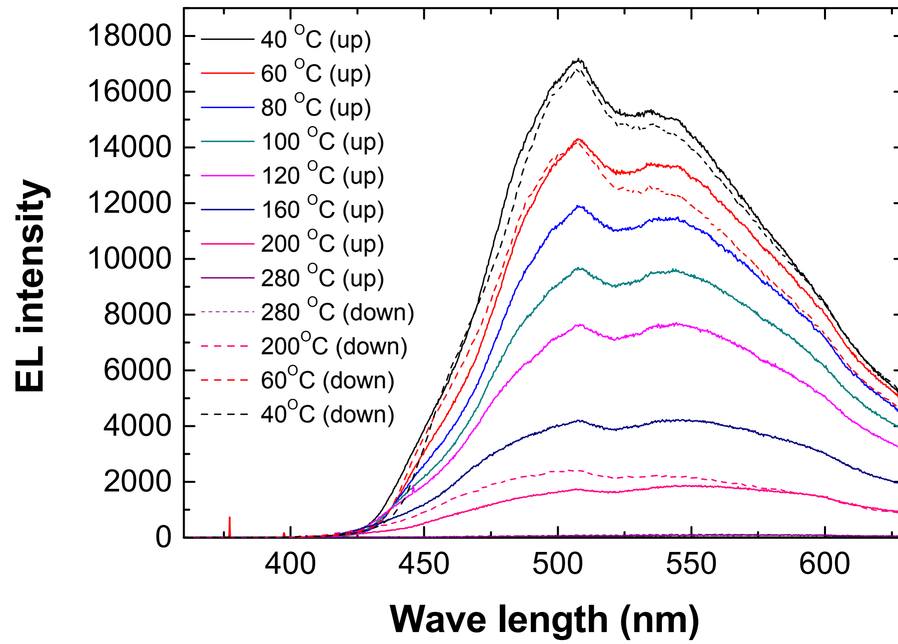

Figure 5.11. Temperature dependent EL spectra of GaN microdisk LEDs and GaN thin film LEDs.

The light-emitting behavior of the LEDs at temperatures ranging from 20 to 100°C was further evaluated by plotting the light intensity and peak energy as a function of temperature. Figure 5.12(a) plots the light intensity as a function of temperature. The light intensity of the GaN microdisk LEDs and thin-film LEDs decreased linearly as a function of 1/T to 50°C, while that of the GaN microdisks LEDs decreased exponentially at higher temperature. This indicated that more non-radiative recombination occurred in the GaN microdisk LEDs than in the GaN thin-film LEDs.[108] The plot of peak energy as a function of temperature showed energy shifting of the EL peaks for both samples (Figure 5.12(b)). Linear red-shifting with a slope of 0.39 was found for the GaN thin-film LEDs. Similar red shifting with a slope of 0.40 was observed for the GaN microdisk LEDs over the range of 20–70°C. Generally, such energy shifting for GaN microstructure LEDs under applied voltage-driven conditions is due to anisotropic deposition of InGaN/GaN QWs along the microstructures. However, this red-shifting could be due to a thermal effect on the GaN, whereby carriers relaxed into localized states of lower energy.[109] Therefore, the large red-shifting behavior observed for the

GaN microdisk LEDs at high temperatures presumably resulted from higher dislocation densities in the GaN microdisks than in the GaN thin-films.[77, 110]

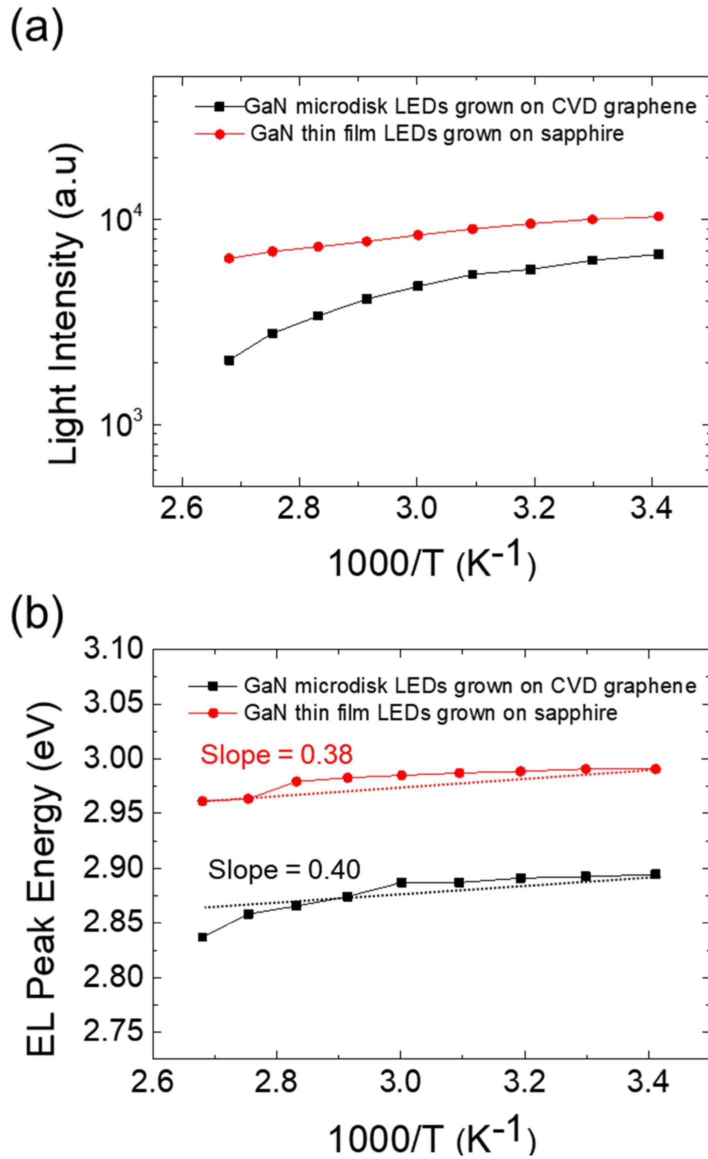

Figure 5.12. Analysis of the light-emitting characteristics as a function of temperature. (a) Plot of light intensity as a function of temperature. (b) Plot of peak energy of light emission as a function of temperature.

5.6. Summary

In conclusion, monolithically integrated multi-color LEDs were fabricated using *p*-GaN layer and QW deposition on morphology-controlled *n*-GaN microstructures on CVD graphene films. The morphology controlled growth of GaN microstructures was investigated by controlling spacings of the ZnO nanotube arrays; microrod and micropyramid were grown on the spacings of 2 and 6 μm, respectively. The microrod and micropyramid based LEDs show blue and green light emission under applied currents from 0.11 to 0.50 mA. They show larger EL peak shift from micropyramid-based LED than that from microrod-based LED. Furthermore, the LEDs fabricated on CVD graphene films were readily transferred onto flexible substrate, which operated in a flexible form. The microrod-based LED shows reliable LED performances without significant degradation of the LED performance. We believe that the monolithic integrated flexible multi-color LEDs will pave the way for development of next generation optoelectronic devices using flexible inorganic LEDs such as large-scale, high-

resolution and full color flexible display.

In addition, we evaluated the light-emitting characteristics of GaN microdisk LEDs on CVD-graphene dots at temperatures ranging from 20 to 100°C. The temperature-dependent EL characteristics of these devices were compared with those of conventional GaN thin-film LEDs on a sapphire substrate. The measurements revealed that the degradation of the light-emitting characteristics, i.e., light intensity and EL peak energy shifting, of the GaN disk LEDs on CVD-graphene films was similar to that of the GaN thin-film LEDs on sapphire in the temperature ranges between 20 to 80°C, respectively.

Conclusion and Outlook

6

6.1. Conclusion

Hybrid-dimensional nanostructures have been investigated and their applications on flexible devices including FET and blue LEDs have been demonstrated. Their excellent device performances after many times of bendings are promising to demonstrate wearable devices which require stable device performances under physically harsh conditions. Although previous works on hybrid materials have focused on flexible LEDs and FET, these graphene-based hybrid materials can provide further functionality beyond previously demonstrated devices. For example, electronics need to not only process the information, but also be capable for data storages to save the processed data. To communicate the processed data with user efficiently, high-resolution optoelectronics are required to display the information accurately. The main objective of the dissertation is to develop more functional devices to meet

demands for flexible devices based on hybrid dimensional nanomaterial systems. The approach of this dissertation is to develop new material system which gives novel functionality to the hybrid dimensional nanomaterial systems. To fabricate next generation non-volatile memory devices based on hybrid-dimensional nanostructures, we prepared oxide/nitride hybrid material system prepared on CVD-graphene films and fabricated flexible ReRAM devices. Owing to their discrete material structures and excellent flexibility of graphene films, stable resistive switching characteristics including cumulative probability, endurance, and retention analysis were measured even in bent and rolled states. After 1000 times of bending, we obtain that resistive switching characteristics are not degraded. Furthermore, even at 450K, our hybrid device shows stable resistive switching characteristics without overlap between HRS and LRS. We believe that our hybrid structures may foster inorganic based flexible memory applications with good durability on harsh conditions including many times of banding and device operation in high temperature. Furthermore, using NiO/GaN hybrid material structures, we proposed a new hybrid structure composed of ReRAM and

LED which enables us to monitor the time evolution of CF configuration on the device scale during resistive switching. We directly observe unstable formation/rupture process of CF and anomalous conducting filament connection, which accompany switching parameter fluctuation considered as critical weaknesses of the ReRAM. In contrast to former real-time measurement studies using in-situ TEM or C-AFM, we can investigate the change in CF configuration in whole area of the device during more than 50 times of resistive switching in atmospheric condition. Our ReRAM/LED hybrid structure demonstrates that unstable formation/rupture process of CF during resistive swiching gives rise to either change in major CF or growth of minor CF's which potentially cause variation on CF configuration and thus large fluctuation in switching parameters.

Recent studies on GaN based micro- and nanostructures on CVD-graphene films demonstrated feasibility for their application on flexible light emitting devices. However, their full color display application has still remained out of reach because of difficulty in achieving multiple color generation from inorganic LEDs on the same substrate. A difficulty in monolithic integration of

various GaN microstructures on CVD graphene films for multi-color emissions represent one of the major obstacles to using inorganic semiconductors in flexible full color light emitting devices. Accordingly, one critical step for the flexible and full light emitting devices is to prepare monolithic integrated various GaN microstructures on CVD graphene films. Here, we reported on the fabrication of flexible and monolithically integrated multi-color micro LEDs using GaN microrods and micropyramids simultaneously grown on CVD graphene films. Monolithically integrated multi-color LEDs were fabricated using *p*-GaN layer and QW deposition on morphology-controlled *n*-GaN microstructures on CVD graphene films. The morphology controlled growth of GaN microstructures was investigated by controlling spacings of the ZnO nanotube arrays; microrod and micropyramid were grown on the spacings of 2 and 6 μm, respectively. The microrod and micropyramid based LEDs show blue and green light emission under applied currents from 0.11 to 0.50 mA. They show larger EL peak shift from micropyramid-based LED than that from microrod-based LED. Furthermore, the LEDs fabricated on CVD graphene films were readily transferred onto flexible

substrate, which operated in a flexible form. The microrod-based LED shows reliable LED performances without significant degradation of the LED performance. We believe that the monolithic integrated flexible multi-color LEDs will pave the way for development of next generation optoelectronic devices using flexible inorganic LEDs such as large-scale, high-resolution and full color flexible display. In addition, we evaluated the light-emitting characteristics of GaN microdisk LEDs on CVD-graphene dots at temperatures ranging from 20 to 100°C. The temperature-dependent EL characteristics of these devices were compared with those of conventional GaN thin-film LEDs on a sapphire substrate. The measurements revealed that the degradation of the light-emitting characteristics, i.e., light intensity and EL peak energy shifting, of the GaN disk LEDs on CVD-graphene films was similar to that of the GaN thin-film LEDs on sapphire in the temperature ranges between 20 to 80°C, respectively.

6.2. Future works and outlook

This research demonstrated the hybrid material systems composed of oxide and nitride nano/microstructures on graphene films and their applications on flexible electronics and optoelectronics. NiO/GaN hybrid material systems motivated to fabricate a flexible ReRAM and successfully demonstrated its stable resistive switching characteristics under various bending status, indeed. Novel optoelectronic devices have been also demonstrated based on monolithic integration of morphology controlled GaN microstructures on graphene films. However, further improvement in device structures and material engineering should be accompanied to use them in more practical applications as following.

Flexible ReRAM based on hybrid dimensional material systems

NiO/GaN hybrid structures have novel advantages for their applications in resistive switching memories. Commercialized ReRAM cells consist of a diode and a resistor (1D1R) to selectively read/write information. The NiO/GaN hybrid structures can intrinsically satisfy the requirement to consist ReRAM cells since GaN has been applied on many electronics including Schottky diode and high

electron mobility transistor (HEMT). For their further practical applications, underlying GaN layer needs to be functionalized as diode layers by depositing metal layers between GaN and NiO layers.

Monolithic integration of morphology controlled GaN microstructures on graphene films for flexible & multi-color LEDs

In order to fabricate more practical devices, another shape of GaN microstructure needs to be grown simultaneously for red color emissions. According to the growth morphology studies depending on spacing of the ZnO nanotube arrays, further increasing of the spacings does not change the morphology of the microstructures, but selectivity of the growth significantly decreases. To grow another structure, we may need to increase a diameter of the ZnO nanotubes and optimize growth conditions to introduce more drastic growth rate differences.

In addition, to grow the microstructures more closely each other for applications on high-resolution display, further material engineering needs to be accompanied including studies on morphology change behavior depending on

length or shape of the ZnO nanotubes.

REFERENCES

1. J. A. Rogers, T. Someya and Y. Huang, science **327** (5973), 1603-1607 (2010).

2. T. Sekitani, H. Nakajima, H. Maeda, T. Fukushima, T. Aida, K. Hata and T. Someya, Nature materials **8** (6), 494-499 (2009).

3. T. Sekitani and T. Someya, Advanced Materials **22** (20), 2228-2246 (2010).

4. Y. Sun and J. A. Rogers, Advanced Materials **19** (15), 1897-1916 (2007).

5. A. Carlson, A. M. Bowen, Y. Huang, R. G. Nuzzo and J. A. Rogers, Advanced Materials **24** (39), 5284-5318 (2012).

6. W. Wong, T. Sands and N. Cheung, Applied Physics Letters **72** (5), 599-601 (1998).

7. K. Chung, S. I. Park, H. Baek, J.-S. Chung and G.-C. Yi, NPG Asia Materials **4** (9), e24-e24 (2012).

8. J. B. Park, H. Oh, J. Park, N.-J. Kim, H. Yoon and G.-C. Yi, Apl Materials **4** (10), 106104 (2016).

9. H. Oh, J. Park, W. Choi, H. Kim, Y. Tchoe, A. Agrawal and G. C. Yi, Small **14** (17), 1800240 (2018).

10. C. H. Lee, Y. J. Kim, Y. J. Hong, S. R. Jeon, S. Bae, B. H. Hong and G. C. Yi, Advanced materials **23** (40), 4614-4619 (2011).

11. K. Chung, H. Yoo, J. K. Hyun, H. Oh, Y. Tchoe, K. Lee, H. Baek, M. Kim and G. C. Yi, Advanced materials **28** (35), 7688-7694 (2016).

12. M. Coll, J. Fontcuberta, M. Althammer, M. Bibes, H. Boschker, A. Calleja, G. Cheng, M. Cuoco, R. Dittmann and B. Dkhil, Applied surface science **482**, 1-93 (2019).

13. H. Y. Hwang, Y. Iwasa, M. Kawasaki, B. Keimer, N. Nagaosa and Y. Tokura, Nature materials **11** (2), 103-113 (2012).

14. Y. Chen, IEEE Transactions on Electron Devices **67** (4), 1420-1433 (2020).

15. S. Kim, J. H. Son, S. H. Lee, B. K. You, K. I. Park, H. K. Lee, M. Byun and K. J. Lee, Advanced Materials **26** (44), 7480-7487 (2014).

16. S. Chopra and S. Subramaniam, Int. J. Innovative Science **2** (4) (2015).
17. S. Hormoz and S. Ramanathan, Solid-State Electronics **54** (6), 654-659 (2010).
18. S. Sugahara, IEE Proceedings-Circuits, Devices and Systems **152** (4), 355-365 (2005).
19. M. T. Greiner, L. Chai, M. G. Helander, W. M. Tang and Z. H. Lu, Advanced Functional Materials **22** (21), 4557-4568 (2012).
20. M. Lorenz, M. R. Rao, T. Venkatesan, E. Fortunato, P. Barquinha, R. Branquinho, D. Salgueiro, R. Martins, E. Carlos and A. Liu, Journal of Physics D: Applied Physics **49** (43), 433001 (2016).
21. D. Newns, J. Misewich, C. Tsuei, A. Gupta, B. Scott and A. Schrott, Applied Physics Letters **73** (6), 780-782 (1998).
22. A. Pergament, G. Stefanovich and A. Velichko, Journal on Selected Topics in Nano Electronics and Computing **1** (1), 24-43 (2013).
23. T. Tanaka, K. Tomioka, S. Hara, J. Motohisa, E. Sano and T. Fukui, Applied physics express **3** (2), 025003 (2010).
24. G. M. Cohen and P. M. Solomon, (Google Patents, 2007).
25. K. Tomioka, M. Yoshimura, E. Nakai, F. Ishizaka and T. Fukui, presented at the 2013 IEEE International Electron Devices Meeting, 2013 (unpublished).
26. H. T. Ng, J. Han, T. Yamada, P. Nguyen, Y. P. Chen and M. Meyyappan, Nano Lett. **4** (7), 1247-1252 (2004).
27. A. Chen, Solid-State Electronics **125**, 25-38 (2016).
28. M. Suzuki, Journal of the Ceramic Society of Japan **103** (1203), 1099-1111 (1995).
29. J. H. Park, H. Y. Kim, G. S. Jang, D. Ahn and S. K. Joo, Journal of Physics D: Applied Physics **49** (7), 075106 (2016).
30. S. Bhatti, R. Sbiaa, A. Hirohata, H. Ohno, S. Fukami and S. Piramanayagam, Materials Today **20** (9), 530-548 (2017).
31. A. Khvalkovskiy, D. Apalkov, S. Watts, R. Chepulskii, R. Beach, A. Ong, X. Tang, A. Driskill-Smith, W. Butler and P. Visscher, Journal of Physics D: Applied Physics **46** (7), 074001 (2013).

32. S. Raoux, R. M. Shelby, J. Jordan-Sweet, B. Munoz, M. Salinga, Y.-C. Chen, Y.-H. Shih, E.-K. Lai and M.-H. Lee, Microelectronic Engineering **85** (12), 2330-2333 (2008).
33. S. Raoux, Annual Review of Materials Research **39**, 25-48 (2009).
34. M.-J. Lee, C. B. Lee, D. Lee, S. R. Lee, M. Chang, J. H. Hur, Y.-B. Kim, C.-J. Kim, D. H. Seo and S. Seo, Nature materials **10** (8), 625-630 (2011).
35. A. Sawa, Materials today **11** (6), 28-36 (2008).
36. R. Jung, M.-J. Lee, S. Seo, D. C. Kim, G.-S. Park, K. Kim, S. Ahn, Y. Park, I.-K. Yoo and J.-S. Kim, Applied physics letters **91** (2), 022112 (2007).
37. S. Kim and Y.-K. Choi, Applied physics letters **92** (22), 223508 (2008).
38. C. Wu, K. Zhang, F. Wang, X. Wei and J. Zhao, ECS Transactions **44** (1), 87 (2012).
39. H. Y. Jeong, Y. I. Kim, J. Y. Lee and S.-Y. Choi, Nanotechnology **21** (11), 115203 (2010).
40. J. Yun, K. Cho, B. Park, B. H. Park and S. Kim, Journal of Materials Chemistry **19** (14), 2082-2085 (2009).
41. F. Ponce and D. Bour, Nature **386** (6623), 351-359 (1997).
42. N. Guan, X. Dai, A. V. Babichev, F. H. Julien and M. Tchernycheva, Chemical science **8** (12), 7904-7911 (2017).
43. J. Y. Tsao, M. H. Crawford, M. E. Coltrin, A. J. Fischer, D. D. Koleske, G. S. Subramania, G. T. Wang, J. J. Wierer and R. F. Karlicek Jr, Advanced Optical Materials **2** (9), 809-836 (2014).
44. S. Strite and H. Morkoç, Journal of Vacuum Science & Technology B: Microelectronics and Nanometer Structures Processing, Measurement, and Phenomena **10** (4), 1237-1266 (1992).
45. M. Razeghi, IEEE Photonics Journal **3** (2), 263-267 (2011).
46. M. Soltani, R. Soref, T. Palacios and D. Englund, Optics express **24** (22), 25415-25423 (2016).
47. S. Lester, F. Ponce, M. Craford and D. Steigerwald, Applied Physics Letters **66** (10), 1249-1251 (1995).
48. M. F. Schubert, S. Chhajed, J. K. Kim, E. F. Schubert, D. D. Koleske, M. H. Crawford, S. R. Lee, A. J. Fischer, G. Thaler and M. A. Banas, Applied

Physics Letters **91** (23), 231114 (2007).
49. W. A. Melton and J. I. Pankove, Journal of crystal growth **178** (1-2), 168-173 (1997).
50. N. Grandjean, J. Massies, Y. Martinez, P. Vennegues, M. Leroux and M. Laügt, Journal of crystal growth **178** (3), 220-228 (1997).
51. S. Pal and C. Jacob, Bulletin of Materials Science **27** (6), 501-504 (2004).
52. B. Zhang and Y. Liu, Chinese science bulletin **59** (12), 1251-1275 (2014).
53. F. Ponce, B. Krusor, J. Major Jr, W. Plano and D. Welch, Applied physics letters **67** (3), 410-412 (1995).
54. A. Tanaka, W. Choi, R. Chen and S. A. Dayeh, Advanced Materials **29** (38), 1702557 (2017).
55. M. K. Kelly, R. P. Vaudo, V. M. Phanse, L. Görgens, O. Ambacher and M. Stutzmann, Japanese journal of applied physics **38** (3A), L217 (1999).
56. J. H. Choi, E. H. Cho, Y. S. Lee, M. B. Shim, H. Y. Ahn, C. W. Baik, E. H. Lee, K. Kim, T. H. Kim and S. Kim, Advanced Optical Materials **2** (3), 267-274 (2014).
57. C.-M. Kang, J.-Y. Lee, M.-D. Park, S.-H. Mun, S.-Y. Choi, K. Kim, S. Kim, J.-P. Shim and D.-S. Lee, presented at the SID Symposium Digest of Technical Papers, 2018 (unpublished).
58. H. Ohmae, Y. Tomita, M. Kasahara, J. Schram, E. Smits, J. Van den Brand, F. Bossuyt, J. Vanfleteren and J. De Baets, presented at the SID Symposium Digest of Technical Papers, 2015 (unpublished).
59. V. W. Lee, N. Twu and I. Kymissis, Information Display **32** (6), 16-23 (2016).
60. F. Nguyen, Synthetic metals **122** (1), 215-219 (2001).
61. M. A. Meitl, Z.-T. Zhu, V. Kumar, K. J. Lee, X. Feng, Y. Y. Huang, I. Adesida, R. G. Nuzzo and J. A. Rogers, Nature materials **5** (1), 33-38 (2006).
62. Y. Robin, Y. Liao, M. Pristovsek and H. Amano, physica status solidi (a) **215** (21), 1800361 (2018).
63. K. Chung, J. Sui, B. Demory, C.-H. Teng and P.-C. Ku, Applied Physi

cs Letters **110** (11), 111103 (2017).
64. K. Kishino, A. Yanagihara, K. Ikeda and K. Yamano, Electronics Letters **51** (11), 852-854 (2015).
65. S. Bae, H. Kim, Y. Lee, X. Xu, J.-S. Park, Y. Zheng, J. Balakrishnan, T. Lei, H. R. Kim and Y. I. Song, Nature nanotechnology **5** (8), 574 (2010).
66. S. J. Kim, K. Choi, B. Lee, Y. Kim and B. H. Hong, Annual Review of Materials Research **45**, 63-84 (2015).
67. Y.-J. Kim, J.-H. Lee and G.-C. Yi, Applied Physics Letters **95** (21), 213101 (2009).
68. Y. J. Kim, H. Yoo, C. H. Lee, J. B. Park, H. Baek, M. Kim and G. C. Yi, Advanced materials **24** (41), 5565-5569 (2012).
69. J. Jo, H. Yoo, S. I. Park, J. B. Park, S. Yoon, M. Kim and G. C. Yi, Advanced Materials **26** (13), 2011-2015 (2014).
70. Y. J. Hong, J. W. Yang, W. H. Lee, R. S. Ruoff, K. S. Kim and T. Fukui, Advanced Materials **25** (47), 6847-6853 (2013).
71. Y. J. Hong, W. H. Lee, Y. Wu, R. S. Ruoff and T. Fukui, Nano letters **12** (3), 1431-1436 (2012).
72. J.-H. Kang, Y. Ronen, Y. Cohen, D. Convertino, A. Rossi, C. Coletti, S. Heun, L. Sorba, P. Kacman and H. Shtrikman, Semiconductor Science and Technology **31** (11), 115005 (2016).
73. Y. Tchoe, J. Jo, M. Kim and G.-C. Yi, NPG Asia Materials **7** (8), e206-e206 (2015).
74. A. Yoon, J. Y. Park, J. M. Jeon, Y. Cho, J. B. Park, G. C. Yi, K. H. Oh, H. N. Han and M. Kim, small **9** (13), 2255-2259 (2013).
75. S. I. Park, Y. Tchoe, H. Baek, J. Heo, J. K. Hyun, J. Jo, M. Kim, N.-J. Kim and G.-C. Yi, APL materials **3** (1), 016103 (2015).
76. K. Chung, C.-H. Lee and G.-C. Yi, Science **330** (6004), 655-657 (2010).
77. H. Yoo, K. Chung, Y. S. Choi, C. S. Kang, K. H. Oh, M. Kim and G. C. Yi, Advanced Materials **24** (4), 515-518 (2012).
78. Y. Tchoe, M. S. Song, H. Kim, H. Baek, J. Y. Park, H. Oh, K. Lee, K. Chung, J. K. Hyun and G.-C. Yi, Nano Energy, 104955 (2020).

79. H. Klauk, Nature Mater. **6** (6), 397-398 (2007).
80. M. Kaltenbrunner, T. Sekitani, J. Reeder, T. Yokota, K. Kuribara, T. Tokuhara, M. Drack, R. Schwödiauer, I. Graz and S. Bauer-Gogonea, Natur **499** (7459), 458-463 (2013).
81. S. E. Ahn, M. J. Lee, Y. Park, B. S. Kang, C. B. Lee, K. H. Kim, S. Seo, D. S. Suh, D. C. Kim and J. Hur, Adv. Mater. **20** (5), 924-928 (2008).
82. M.-J. Lee, C. B. Lee, D. Lee, S. R. Lee, M. Chang, J. H. Hur, Y.-B. Kim, C.-J. Kim, D. H. Seo and S. Seo, Nature Mater. **10** (8), 625-630 (2011).
83. C. Kügeler, M. Meier, R. Rosezin, S. Gilles and R. Waser, Solid-State Electron. **53** (12), 1287-1292 (2009).
84. R. H. Kim, H. J. Kim, I. Bae, S. K. Hwang, D. B. Velusamy, S. M. Cho, K. Takaishi, T. Muto, D. Hashizume and M. Uchiyama, Nature communications **5** (2014).
85. T. W. Kim, H. Choi, S. H. Oh, G. Wang, D. Y. Kim, H. Hwang and T. Lee, Adv. Mater. **21** (24), 2497-2500 (2009).
86. S. Lee, H. Kim, D.-J. Yun, S.-W. Rhee and K. Yong, Appl. Phys. Lett. **95** (26), 262113 (2009).
87. J. Moon, J. Kim, H. Lee, C. Ahn, H. Cho, J. Lee and H. Kim, Journal of the Korean Physical Society **53** (9), 3681-3684 (2008).
88. Y. Zhang, X. Li, L. Wang, X. Yi, D. Wu, H. Zhu and G. Wang, Nanoscale **4** (19), 5852-5855 (2012).
89. S. C. Chae, J. S. Lee, S. Kim, S. B. Lee, S. H. Chang, C. Liu, B. Kahng, H. Shin, D. W. Kim and C. U. Jung, Advanced Materials **20** (6), 1154-1159 (2008).
90. G.-S. Park, X.-S. Li, D.-C. Kim, R.-J. Jung, M.-J. Lee and S. Seo, Applied Physics Letters **91** (22), 222103 (2007).
91. M. Qian, Y. Pan, F. Liu, M. Wang, H. Shen, D. He, B. Wang, Y. Shi, F. Miao and X. Wang, Advanced materials **26** (20), 3275-3281 (2014).
92. W. Lee, J. Park, S. Kim, J. Woo, J. Shin, G. Choi, S. Park, D. Lee, E. Cha and B. H. Lee, ACS nano **6** (9), 8166-8172 (2012).
93. I. K. Yoo, B. S. Kang, S. E. Ahn, C. B. Lee, M. J. Lee, G.-S. Park and X.-S. Li, IEEE transactions on nanotechnology **9** (2), 131-133 (2010).

94. J. B. Yun, S. Kim, S. Seo, M. J. Lee, D. C. Kim, S. E. Ahn, Y. Park, J. Kim and H. Shin, physica status solidi (RRL)–Rapid Research Letters **1** (6), 280-282 (2007).
95. J. Son and Y.-H. Shin, Applied Physics Letters **92** (22), 222106 (2008).
96. Q. Liu, J. Sun, H. Lv, S. Long, K. Yin, N. Wan, Y. Li, L. Sun and M. Liu, Advanced Materials **24** (14), 1844-1849 (2012).
97. I. Hwang, M.-J. Lee, J. Bae, S. Hong, J.-S. Kim, J. Choi, X. L. Deng, S.-E. Ahn, S.-O. Kang and B. H. Park, IEEE electron device letters **33** (6), 881-883 (2012).
98. J. Herrnsdorf, J. J. McKendry, S. Zhang, E. Xie, R. Ferreira, D. Massoubre, A. M. Zuhdi, R. K. Henderson, I. Underwood and S. Watson, IEEE Transactions on Electron Devices **62** (6), 1918-1925 (2015).
99. I. Akasaki and H. Amano, Japanese journal of applied physics **45** (12R), 9001 (2006).
100. Y. Tchoe, K. Chung, K. Lee, J. Jo, K. Chung, J. K. Hyun, M. Kim and G.-C. Yi, NPG Asia Materials **11** (1), 1-7 (2019).
101. M. Funato, K. Hayashi, M. Ueda, Y. Kawakami, Y. Narukawa and T. Mukai, Applied Physics Letters **93** (2), 021126 (2008).
102. K. Hiramatsu, K. Nishiyama, A. Motogaito, H. Miyake, Y. Iyechika and T. Maeda, physica status solidi (a) **176** (1), 535-543 (1999).
103. M. Rozhavskaya, W. Lundin, S. Troshkov, A. Tsatsulnikov and V. Dubrovskii, physica status solidi (a) **212** (4), 851-854 (2015).
104. Y. J. Hong, C. H. Lee, A. Yoon, M. Kim, H. K. Seong, H. J. Chung, C. Sone, Y. J. Park and G. C. Yi, Advanced Materials **23** (29), 3284-3288 (2011).
105. A. K. Rishinaramangalam, M. Nami, M. N. Fairchild, D. M. Shima, G. Balakrishnan, S. Brueck and D. F. Feezell, Applied Physics Express **9** (3), 032101 (2016).
106. G. Gustafsson, Y. Cao, G. Treacy, F. Klavetter, N. Colaneri and A. Heeger, Nature **357** (6378), 477 (1992).
107. S. R. Forrest, Nature **428** (6986), 911 (2004).
108. J. Liu, W.-S. Tam, H. Wong and V. Filip, Microelectronics Reliability **49** (1), 38-41 (2009).

109. X. Cao, S. Leboeuf, L. Rowland and H. Liu, Journal of electronic materials **32** (5), 316-321 (2003).
110. L. Polenta, M. Rossi, A. Cavallini, R. Calarco, M. Marso, R. Meijers, T. Richter, T. Stoica and H. Lüth, ACS nano **2** (2), 287-292 (2008).

Abstract (Korean)

국문요약문

물리적으로 강하고 유연한 그래핀과 같은 2 차원 소재위에 성장된 무기물 나노소재로 구성된 복합차원 나노소재는 유연한 대면적 전자 및 광전소자로의 응용에 적합한 형태의 소재 구조이며, 실제로 이를 기반으로 한 유연한 수직형 전계효과 트랜지스터 및 발광다이오드 등을 포함한 많은 소자들이 개발되고 있다. 하지만, 처리된 정보를 저장하고 이를 사용자에게 전달하는 기능을 수행하기 위해선 보다 다양한 소자들이 개발되어야 할 필요가 있다. 본 학위논문은 이러한 수요를 충족시키기 위해, 복합차원 나노소재 기반 유연한 대면적 차세대 비휘발성 메모리 및 유연한 대면적 다파장 발광 다이오드의 개발에 대하여 다루고 있다.

복합차원 나노소재를 기반으로 차세대 비휘발성 메모리를 구현하기 위해 니켈 산화물 및 질화갈륨 이종구조로 구성된

마이크로디스크 형태의 소재를 그래핀 위에 성장하고, 본 소재의 상부 및 하부에 전극을 증착하여 전극/산화물/전극으로 구성된 형태의 산화물 기반 저항변화 메모리를 제조할 수 있었다. 마이크로디스크 형태의 소재의 사이가 떨어져있기 때문에 본 소자를 유연한 형태에서 구현하거나 1,000 회 이상의 구부림 뒤 소자의 특성을 파악할 때 소자 특성의 큰 변화 없이 정보가 안정적으로 저장되는 특성을 확인할 수 있었다. 뿐만 아니라, 니켈 산화물 기반 저항변화메모리를 동작할 때, 산화물 내부에 전도성이 높은 니켈 산화물이 필라멘트 형태로 구성되는데, 이를 발광다이오드의 나노전극으로 사용하여 저항변화메모리 내부의 필라멘트 역학에 대해서도 연구할 수 있었다.

한편, 저장된 정보를 사용자에게 정확하게 전달하기 위해선 발광다이오드의 한 픽셀 (pixel) 의 크기가 수 마이크로미터 이하로 작아야하고, 빨강, 초록, 파랑색의 빛을 발광할 수 있어야 하는데 이는 현재 이용되고 있는 픽 앤 플레이스 (pick and place) 기술을 이용하여 제조할 때 소자 제조의 효율성 및 재현성에 한계를 보이고 있다. 본 학위논문에서는 이를 극복하기 위한 방법의 하나로, 다양한 색을

발광할 수 있는 발광다이오드를 하나의 그래핀 기판위에 동시에 성장하는 방법을 제시하고 이를 유연한 다파장 발광다이오드로 구현하는 방법에 대해 기술하고 있다. 본 소자를 구현하기 위해 다양한 모양의 질화갈륨 및 산화아연 이종구조를 그래핀 위에 성장하는 방법을 개발하였는데, 산화아연 나노튜브의 간격을 다르게 설정하여 성장하고 이 위에 질화갈륨을 성장하면 질화갈륨의 성장률이 나노튜브의 간격에 따라 다르게 형성되어 다른 모양의 마이크로 발광다이오드가 성장되는 것을 이용하였다. 각기 다른 발광다이오드에 같은 전압을 가해줬을 때 성장률의 차이로 인한 다중 양자 우물 조성의 변화 및 소재 내부의 결함으로 인해 각기 다른 파장의 색이 발광되는 특성을 확인하였고, 유연한 형태에서도 안정적으로 발광특성이 유지되는 것을 확인할 수 있었다.

지도해주신 교수님, 함께 동고동락한 선후배 및 동료,

소중한 친구들, 그리고 사랑하는 가족에게 바칩니다.

Curriculum Vitae

Keundong Lee

22 – 410, Seoul National University, 1 Gwanakro, Gwanak-gu, Seoul, 08826, Korea| +82-2-880-2652 | keundonglee@snu.ac.kr

EDUCATION AND EXPERIENCE

University of California, San Diego
Visiting research scholar **Mar. 2016 - Present**
Advisor: Prof. Shadi Dayeh

Seoul National University, Seoul, Korea
Ph.D. candidate in Physics **Mar. 2014 - Present**
Advisor: Prof. Gyu-Chul Yi

Konkuk University, Seoul,Korea
M.A. in Physics **Mar. 2012 - Feb. 2014**
Advisor: Prof. Bae Ho Park

Konkuk University, Seoul,Korea
B.A. in Physics **Mar. 2008 - Feb 2012**

RESEARCH

Flexible optoelectronic/electronic device fabrication using GaN microstructure grown on graphene films

2014 – present

GaN has been studied as one of the promising material to be used in electronic and optic devices represented as power device and light emitting diode (LED). However, due to lattice mismatch, only few of single crystal substrates have been used leading high cost in growth of high quality GaN thin film and micro-structure. In addition, problems associated with high-quality inorganic film growth on large or flexible substrates represent one of the major obstacles to the use of inorganic semiconductors in foldable-display and solar cell applications. To decrease the cost in substrates for GaN growth and suggest solution about large and flexible device issues, GaN growth on graphene thin films transferred on arbitrary substrates was introduced by *Science* at 2010. Due to outstanding electrical transport properties and mechanically strong characteristics of the graphene, flexible optic and electronic devices based on GaN were able to be demonstrated. In my research, morphology control of the microstructure GaN from micro-rod to pyramid grown on graphene thin films was performed. Current research interests extend to fabricate flexible next-generation non-volatile memory and flexible & color tunable LED using oxide/nitride hybrid material systems prepared on chemical vapor deposited (CVD) graphene films.

Enhancement of ReRAM performance by control of growth parameter, modification of device structure, and study of resistive switching phenomena.

2011 – 2017

Resistive random access memory (ReRAM) has been considered one of the promising non-volatile memory devices to overcome the limitations of Si-based flash memory, as it has a high operating speed, low power consumption and high scalability. However, fluctuation in operation parameters of ReRAM remains a

critical weakness that leads to device failures. To enhance the stability of the operation parameters, many studies have been undertaken through optimization of the ReRAM material characteristics. In my research, through deposition parameter control including growth time, temperature and pressure, significant resistive switching characteristic improvement was achieved. Moreover, by simple insertion of defective graphene in the ReRAM which is metal-insulator-metal capacitor structure, operation voltage overlap between turn on and off was successfully limited. Current research interests are concentrated on study of resistive switching phenomena using hybrid device consisting by LED and ReRAM.

A hybrid multimodal surface-depth electrode for electrophysiological and multi-photon brain activity mapping

2016 – present

One of the grand challenges in neuroscience is to understand how neuronal activity is orchestrated to produce function. Single modality technologies offer either high spatial or high temporal resolution and with varied degrees of coverage. Multimodal approaches that can probe the brain's activity from the surface, at depth, and with high spatiotemporal resolution are believed to yield results that may complete our understanding of behavior and function. We leveraged microelectromechanical systems (MEMS) surface micromachining techniques to developed the hybrid surface-depth electrode. The depth electrode is to be maintained inside the cortex chronically and should not block optical access. Therefore, both the depth and surface electrodes need to be flush with the cortical surface: The integrated depth in our device utilizes an inserter with a small neck-region (narrow-constriction) of SU8 that is sheared (thermally or mechanically) to separate the handle from the implanted portion of the depth electrode.

JOURNAL PUBLICATIONS

"Monolithically integrated flexible and multi-color LEDs using morphology controlled GaN microstructures on graphene films"
K. Lee, Y. Tchoe, J. Park, G.-C. Yi (in preparation) **2020**

"Flexible resistive random access memory devices by using NiO_x/GaN microdisk arrays fabricated on graphene films"
K. Lee, J. Park, Y. Tchoe, J. Yoon, K. Chung, H. Yoon, S. Lee, C. Yoon, B. H. Park, G.-C. Yi, Nanotechnology, 205202 (2017) **2017**

"Real-time device-scale imaging of conducting filaments in resistive switching materials"
K. Lee, Y. Tchoe, H. Baek, K. Chung, S. Lee, C. Yoon, B. H. Park, G.-C. Yi, Scientific Reports, 27451 (2016) **2016**

"Enhancement of resistive switching under confined current path distribution enabled by insertion of atomically thin defective monolayer graphene"
K. Lee*, I. Hwang*, S. Lee, S. Oh, D. Lee, C. K. Kim, Y. Nam, S. Hong, C. Yoon, R. B. Morgan, H. Kim, S. Seo, D. H. Seo, S. Lee, B. H. Park,
Scientific Reports, 11279 (2015) **2015**

"Individually addressable, high-density vertical nanotube Schottky diode crossbar array"
Y. Tchoe, M. S Song, H. Kim, H. Baek, J. Y. Park, H. Oh, **K. Lee**, K. Chung, J. K Hyun, G.-C. Yi
Nano Energy, 104955 (2020) **2020**

"Large Wavelength Response to Pressure Enabled in InGaN/GaN Microcrystal LEDs with 3D Architectures"
D. W. Yang, **K. Lee**, S. Jang, W. J. Chang, S. H. Kim, J. H. Lee, G.-C. Yi, W. I. Park,

ACS Photonics 7, 1122 (2020) **2020**

"Free-standing and ultrathin inorganic light-emitting diode array"
Y. Tchoe, K. Chung, **K. Lee**, J. Jo, K. Chung, J. K. Hyun, M. Kim, G.-C. Yi,
NPG Asia Materials 11:37 (2019) **2019**

"Self-contained InGaN/GaN micro-crystal arrays as individually addressable multi-color emitting pixels on a deformable substrate"
D. W. Yang, **K. Lee**, S. Jang, W. J. Chang, S. H. Kim, J. H. Lee, G.-C. Yi, W. I. Park,
Journal of Alloys and Compounds 803, 826 (2019) **2019**

"GaN microstructure light-emitting diodes directly fabricated on tungsten-metal electrodes using a micro-patterned graphene interlayer"
K. Chung, **K. Lee**, Y. Tchoe, H. Oh, JB Park, J. K. Hyun, G.-C. Yi,
Nano energy 60, 82 (2019) **2019**

"Transferable single-crystal GaN thin films grown on chemical vapor-deposited hexagonal BN sheets"
K. Chung, H. Oh, J. Jo, **K. Lee**, M. Kim, G.-C. Yi,
NPG Asia Materials, 9, e410 (2017) **2017**

"Large linear magnetoresistance in heavily-doped Nb:$SrTiO_3$ epitaxial thin films"
H. Jin, **K. Lee**, S.-H. Baek, J.-S. Kim, B. Cheong, B. H. Park, S. Yoon, B. J. Suh, C. Kim, S. S. A. Seo, S. Lee,
Scientific Reports, 34295 (2016) **2016**

"Flexible GaN light-emitting diodes using GaN microdisks epitaxial laterally overgrown on graphene dots"
K. Chung, H. Yoo, J. K. Hyun, H. Oh, Y. Tchoe, **K. Lee**, H. Baek, M. Kim, G.-C. Yi,
Advanced Materials, 28, 7688 (2016) **2016**

“Reduced distributions of the set current and the voltage of unipolar resistance switching in a current-biased set process”
S.-C. Na, M. C. Chun, G. Jang, H. Shin, Y.-S. Kwon, **K. Lee**, C. Yoon, B. H. Park, B. S. Kang,
Journal of the Korean Physical Society, 68, 1467 (2016) **2016**

“A new simple method for point contact Andreev reflection (PCAR) using a self-aligned atomic filament in transition-metal oxides”
I. Hwang, **K. Lee**, H. Jin, S. Choi, E. Jung, B. H. Park, S. Lee,
Nanoscale, 7, 8531 (2015) **2015**

“Effects of the fluctuation in a singly-connected conducting filament structure on the distribution of the reset parameters in unipolar resistance switching”
S.-C. Na, **K. Lee**, M. C. Chun, Y.-S. Kwon, H.-J. Shin, S. Lee, B. H. Park, B. S. Kang,
Applied Physics Letters, 106, 133503 (2015) **2015**

“Ultra-thin resistive switching oxide layers self-assembled by field-induced oxygen migration (FIOM) technique”
S. Lee*, I. Hwang*, S. Oh, S. Hong, Y. Kim, Y. Nam, **K. Lee**, C. Yoon, W. Kim, B. H. Park,
Scientific Reports, 06871 (2014) **2014**

“Switchable Schottky diode characteristics induced by electroforming process in Mn-doped ZnO thin films”
Y. Nam, I. Hwang, S. Oh, S. Lee, **K. Lee**, S. Hong, J. Kim, T. Choi, B. H. Park,
Applied Physics Letters, 102, 162105 (2013) **2013**

CONFERENCE PRESENTATIONS

[Talk] "*Enhancement of Resistive switching characteristic using defective monolayer graphene*", Keundong Lee, Sungtek Oh, Dukhyun Lee, Sangik Lee, Sahwan Hong, Robert Morgan, Sunae Seo, David H.seo, Haksung Kim, Sangwook Lee, Tomoji Kawai, Inrok Hwang, Baeho Park, KPS Spring Meeting, Daejeon, Korea **2012**

[Poster] "*Enhancement of Resistive switching system with controlled electric field distribution using defective monolayer graphene*", Keundong Lee, Sungtek Oh, Dukhyun Lee, Sangik Lee, Sahwan Hong, Robert Morgan, Sunae Seo, David H.seo, Haksung Kim, Sangwook Lee, Tomoji Kawai, Inrok Hwang, Baeho Park, MRS Fall Meeting, Boston, MA **2013**

[Poster] "*Real Time Observation of Conducting Filaments in Resistive Switching Materials with Large Area Imaging Evolution Through Hybrid Device of ReRAM and LED*", Keundong Lee, Youngbin Tchoe, Hyeonjun Baek, Kunook Cheong, Sangik Lee, Chansoo Yoon, Bae Ho Park and Gyu-Chul Yi, CSW 2015, Santa Barbara, CA **2015**

[Talk] "Real-time device-scale imaging of conducting filament dynamics in resistive switching materials" Keundong Lee, Youngbin Tchoe, Hyeonjun Baek, Kunook Cheong, Sangik Lee, Chansoo Yoon, Bae Ho Park and Gyu-Chul Yi, EMC 2016, Delaware, DE **2016**

[Talk] "Selective area, metal-organic vapor phase epitaxial grown of GaN microstructures on graphene film for transferable and color tunable inorganic LEDs" Keundong Lee, Jong-woo Park, Youngbin Tchoe, Hongseok Oh, Dongha Yoo, Jiyoung Yoon and Gyu-Chul Yi, 18th ICMOVPE, San Diego, CA **2016**

[Poster] "Selective area, metal-organic vapor phase epitaxial grown of GaN microstructures on graphene film for transferable and color tunable inorganic LEDs" Keundong Lee, Jong-woo Park, Youngbin Tchoe, Hongseok Oh, Dongha Yoo, Jiyoung Yoon and Gyu-Chul Yi, IWN 2016, Orlando, FL **2016**

[Talk] "Flexible inorganic Light emitting diode integrated PEDOT:PSS/parylene C for high resolution optogenetic studies with electrocorticography (ECoG)" Keundong Lee, Mehran Ganji, Yun Goo Ro, Lorraine Hossain, Sang Heon Lee,

Jong-woo Park, Dongha Yoo, Jiyoung Yoon, Shadi. A. Dayeh and Gyu-Chul Yi, SPIE Photonics West, San Fransisco, CA **2017**

[Talk] "A Hybrid Multimodal Surface-Depth Electrode for Electrophysiological and Multi-Photon Brain Activity Mapping Keundong Lee, Martin Thunemann, Lorraine Hossain, Youngbin Tchoe, Jihwan Lee, Sang Heon Lee, Yun Goo Ro, Gyu-Chul Yi, Anna Devor and Shadi A. Dayeh, 62nd EMC, Online meeting, **2020**

TEACHING EXPERIENCE

Teaching Assistant

Modern Physics Experiment

2012 - 2013

Basic Physics

2012 - 2013

EXPERIMENTAL EXPERIENCE AD TECHNICAL SKILLS

• Material Growth

- Metal-organic chemical vapor deposition (MOCVD) : GaN (Thin film, Rod, Pyramid, Disk) on graphene and Sapphire substrates
- Pulsed Laser Deposition (PLD) : Oxide thin film (Perov-skite structure)

• Material Characterizations

- Morphological and structural characterizations : SEM, AFM, XRD, Raman spectroscopy
- Optical characterization : PL, Photo voltaic measurement

• Semiconductor processing

- Photolithography, wet etching, reactive ion etching, rapid thermal

annealing, metallization, atomic layer deposition, sputtering

PROFESSIONAL ACTIVITIES

- Member of Korean Physical Society (KPS)

  2012 - present
- Visiting scholar in Korea Institute of Science and Technology (KIST)

  2012 - 2013

REFERENCES

Prof. Gyu-Chul Yi
Department of Physics and Astronomy
Seoul National University, Seoul, Korea
Phone: +82 2 880 2651
gcyi@snu.ac.kr

Prof. Bae Ho Park
Department of Physics
Konkuk University, Seoul, Korea
Phone: +82 2 450 3405
baehpark@konkuk.ac.kr

Dr. Suyoun Lee
Electronic Materials Research Center
Korea Institute of Science and Technology, Seoul, Korea
Phone: +82 2 958 5114
slee_eels@kist.re.kr

Prof. Shadi Dayeh
Department of Electrical and Computer Engineering
University of California at San Diego, CA, USA
Phone: +1 858 534 5171
sdayeh@eng.ucsd.edu